

NORTHWESTERN UNIVERSITY

E710,
 $p\bar{p}$ ELASTIC SCATTERING AT TEVATRON ENERGIES

A DISSERTATION

SUBMITTED TO THE GRADUATE SCHOOL
IN PARTIAL FULFILMENT OF THE REQUIREMENTS

for the degree

DOCTOR OF PHILOSOPHY

Field of Physics and Astronomy

By

Sasan Sadr

EVANSTON, ILLINOIS

November 1993

AAC763

List of Figures

1	(a) The effective differential cross section vs $ t $ for no event loss due to pattern width, (b) the expected loss of events at low $ t $	16
2	The Tevatron Main Ring, Energy Doubler, and \bar{p} source	18
3	The E710 detector at the Fermilab Tevatron. Inset: Blow-up of the beam pipe at the positions of the tracking telescopes	19
4	Two roman pots inside their housing, forming a castle. The dashed line indicates the beam axis. (Taken from Ref. [36])	22
5	Geometry of the drift chambers for (a) front and (b) side views	24
6	(a) Map of computed drift potentials, (b) Map of computed drift times	25
7	(a) Front and (b) side views of the trigger counters (TC) and the calibration counter (CC)	26
8	Geometries of the ring scintillation counters around the beam pipe: (a) Ring sets L0-L4, R1-R4, (b) L5, R5, and (c) center counters around E0	27
9	(a) Cross section of the tracking drift chambers, and (b) beam's eye view of the drift chamber telescopes	29
10	A typical TDC distribution	32
11	Stability of statistics with track tolerance	34
12	The y projection of the events penetrating through the indentations of the calibration counter	35
13	The y projection of all events regardless of which counter is hit	36
14	The corrected y projection of events penetrating the calibration counter	37
15	The y calibration fit	39
16	The calibration function superimposed on the normalized x distribution	40
17	Gaussian fit to the x elastic pattern	44
18	Gaussian fit to the y elastic pattern	45

19	Contours of constant $ t $ at c.m. energy of 1.8 TeV	46
20	Contours of constant $ t $ at c.m. energy of 1.0 TeV	47
21	The separation between the background and the signal peaks	49
22	Comparison of background shapes from elastic and background samples	50
23	Fit to the 1.8 TeV data	58
24	Fits to the 600 and 650 series of the 1.8 TeV data	61
25	Fits to run 750 and the 700 series of the 1.8 TeV data	62
26	A $d\sigma/dt$ vs $ t $ fit for σ_t and B from the E710 1989 analysis of the 1.8 TeV data . . .	63
27	The dN/dy vs y^2 fit for elastic scattering distribution, for almost all of the E710 1991 analysis	64
28	Fit to $d\sigma/dt$ vs $ t $ in the high $ t $ region at 1.8 TeV	65
29	The world σ_{el}/σ_t data	66
30	The world pp and $\bar{p}p$ total single-diffractive cross section data	67
31	Fit to the 1.02 TeV data at low $ t $ range	68
32	Fit to the 1.02 TeV data at high $ t $ range	70
33	$\sigma_t(\bar{p}p)$ vs. s . The dashed line shows the behavior of $\sigma_t(pp)$, and the dotted line is given by the Regge pole formula of Landshoff and Donnachie (Eq. 55).	73
34	$B(\bar{p}p)$ vs. s . The dotted line is given by the Pomeron Regge trajectory formula of Landshoff and Donnachie (Eq. 57).	74
35	Cross section vs. energy for pp (\circ) and $\bar{p}p$ (\times) scattering, with a $\log^2 s$ variation, and no Odderon.	75
36	ρ vs. energy for pp (\circ) and $\bar{p}p$ (\times) scattering, with a $\log^2 s$ variation, and no Odderon. 76	
37	Cross section vs. energy for pp (\circ) and $\bar{p}p$ (\times) scattering, with a $\log^2 s$ variation, and Odderon 2.	77
38	ρ vs. energy for pp (\circ) and $\bar{p}p$ (\times) scattering, with a $\log^2 s$ variation, and Odderon 2. 78	
39	Cross section vs. energy for pp (\circ) and $\bar{p}p$ (\times) scattering, with a $\log^2 s$ variation,	

4.2	The Readout System	33
4.2.1	Calibration of the y Readout System	34
4.2.2	Calibration of the x Readout System	39
4.3	Determination of the Scattering Angles	41
4.4	Widths of the Elastic Pattern	43
4.5	Binning of the Data	45
4.6	Background Subtraction	48
4.7	Normalization of the Data	53
4.7.1	The Inelastics	53
4.7.2	The Accelerator Luminosity	53
4.8	Subdivisions within the Data	54
4.9	Fitting the Data	55
5	Results	58
5.1	The 1.8 TeV Data	58
5.1.1	Results from Individual 1.8 TeV Superruns	60
5.1.2	Earlier E710 Elastic Scattering Results at 1.8 TeV	60
5.1.3	Diffraction Dissociation at 1.8 TeV	65
5.2	The 1.02 TeV Data	68
6	Models of Elastic Scattering	72
6.1	The Regge Pole Picture	72
6.2	Analytic Asymptotic Amplitude Analysis of Elastic Scattering	76
6.3	QCD-Inspired Model of Elastic Scattering	85
6.4	Conclusion	90

Appendix A	92
Appendix B	98
Appendix C	100
Appendix D	103
D.1 The Trigger System	103
D.1.1 The Elastic Trigger	104
D.1.2 The Inelastic Trigger	105
D.1.3 The Master Trigger	106
D.2 On-line Data Analysis	107
Appendix E	110
E.1 The Calibration Counter Edge	110
E.2 The Calibration Counter Hole	111
Appendix F	113
F.1 Numerical Integration Techniques	113
F.2 The Effective Differential Elastic Cross Section	115
Appendix G	118
References	122

Of central importance to the determination of the t scales were the relative positions of the detectors with respect to the beam. Stefano Zucchelli provided us with a detailed knowledge of the positions of the pots as well as their internal dimensions.

I am grateful to Monica Bertani and Stan Pruss for assisting me in the determination of the accelerator luminosities. I also thank Carlos Avila and Luis Montes for answering my many questions pertaining to the various aspects of their data analysis.

I would also like to acknowledge Kam Seth of Northwestern University for his constructive suggestions regarding the presentation of the final results. Bob Tilden was responsible for the computer system used for the analysis of data at Northwestern. Jeff Bantly, Dan Claes, Rik Yoshida, and Sue Blessing provided me with helpful suggestions pertaining to programming as well as the format of my dissertation.

I am grateful to David Buchholz, Darwin Chang, and Heidi Schellman for serving at my candidacy and defense committees.

This work was made possible with the financial support of the US Department of Energy, the US National Science Foundation, the Italian Ministero Pubblica Istruzione, and the North Atlantic Treaty Organization.

My thanks go to all of the people in the business office of the Department of Physics and Astronomy at Northwestern whose help has been invaluable.

I would like to close this section on a personal note by expressing my appreciation to all of the friends that I have made during my years at Northwestern. There are simply too many of them to name. Particularly, I wish to mention Tom and Nellie Bohanon, Gerry Garino, Steve Trokenheim, Tony Escobales, Scott Kalbfeld, Ivan Phillips, John Mikrut, Miguel Sarmiento, and Susanne Lomatch. Their comradery and support made my years as a graduate student tolerable.

Evanston, November 1993

Contents

1	Introduction	1
1.1	The Experiment	1
1.2	History of the Field	1
1.3	Interpretation of the Results and Motivation for E710	3
1.4	Results of E710 and its Contemporaries, and their Significance	6
2	Procedure	9
2.1	Experimental Strategy	9
2.2	Formulation of Experimental Procedure	11
3	Experimental Setup	18
3.1	The Tevatron Collider	18
3.2	The E710 Apparatus	19
3.3	The Elastic Scattering Detectors	23
3.3.1	Geometry of the Drift Chambers	23
3.3.2	Scintillation Counters Inside the Roman Pots	25
3.4	The Inelastic Scattering Detectors	26
3.4.1	The Ring Scintillation Counters	26
3.4.2	The Tracking Telescopes	28
4	Data Analysis	31
4.1	Event Selection	31
4.1.1	TDC Windows	31
4.1.2	Trigger Selection	31
4.1.3	Wire and Track Selection	33

ABSTRACT

E710, p \bar{p} ELASTIC SCATTERING AT TEVATRON ENERGIES

Sasan Sadr

Experiment E710, located at site E0 of the Tevatron collider at Fermilab, was conceived in order to measure p \bar{p} elastic scattering. The measured parameters were: the total cross section σ_t , the ratio of the real to the imaginary part of the forward scattering amplitude ρ , the nuclear slope parameter B , the nuclear curvature parameter C , the total elastic cross section σ_{el} , and the single diffractive cross section σ_{sd} . These measurements were taken at center-of-mass energies of $\sqrt{s} = 1.02$ and 1.8 TeV.

Acknowledgements

I would like to take this opportunity to acknowledge my advisor Martin Block, without whose support this work could not have been done in its current format. His emphasis on the education of students and their development as mature scientists is not an abundant commodity in today's world.

I would also like to thank Roy Rubinstein and Jay Orear who were the spokesmen for this experiment.

Shekhar Shukla and Cedric Guss were very helpful to me in the initial months of my involvement with E710. The contributions made by Shekhar Shukla are too numerous to mention. He was responsible for the design and construction of the drift chambers used for the recording of the inelastic events, primarily as they pertained to beam gas. His help was also extremely valuable during the early phase of the analysis of the data at 1.8 TeV. He later initiated the formation of the analysis branch at Fermilab, which culminated with the release of the intermediate results of the 1.8 TeV data in the spring of 1991, thus allowing E710 to obtain and publish a preliminary ρ value for the first time.

Cedric Guss was responsible for the data acquisition system. His subsequent contribution was the preliminary analysis of the 1.8 TeV data at high t regions, resulting in the release of the cross section and nuclear slope values during the summer of 1989.

Acknowledgement must go to Norman Amos and Rosy Mondardini for their construction of the drift chambers used in the collection of data at low t regions.

The effective lengths in the vertical direction were measured as part a detailed study conducted by Ivano Veronesi.

	and Odderon 1.	79
40	ρ vs. energy for pp (o) and $\bar{p}p$ (x) scattering, with a $\log^2 s$ variation, and Odderon 1.	80
41	Cross section vs. energy for pp (o) and $\bar{p}p$ (x) scattering, with a $\log s$ variation, and no Odderon.	81
42	ρ vs. energy for pp (o) and $\bar{p}p$ (x) scattering, with a $\log s$ variation, and no Odderon.	82
43	Cross section vs. energy for pp (o) and $\bar{p}p$ (x) scattering, with a $\log s$ variation, and Odderon 1.	83
44	ρ vs. energy for pp (o) and $\bar{p}p$ (x) scattering, with a $\log s$ variation, and Odderon 1.	84
45	Cross section vs. energy for pp (o) and $\bar{p}p$ (x) scattering, along with eikonalized QCD fit	86
46	ρ vs. energy for pp (o) and $\bar{p}p$ (x) scattering, along with eikonalized QCD fit	87
47	B vs. energy for pp (o) and $\bar{p}p$ (x) scattering, along with eikonalized QCD fit	88
48	Two-Body Elastic Scattering	92
49	Schematic of the pot movement system	100
50	Front and side views of drift chambers inside their castle	101
51	The master trigger logic	106
52	Block digram of on-line data acquisition system	109

List of Tables

1	Recent experimental results at high energies	8
2	Positions of the quadrupole magnets between the inner and outer drift chambers on each side of E0	21
3	Angular acceptance ranges of the ring counter sections and their distances from E0 .	28
4	Systematic error contributions for 1.8 TeV data	59
5	Normalization parameters of the 1.8 TeV superruns	60
6	Systematic error contributions for 1.02 TeV data	69
7	Supercollider cross section predictions	90
8	Values of $ t _{int}$ and θ_{int} for $\bar{p}p$ elastic scattering	97
9	Calibration constants for pot position measurements	102

1 Introduction

1.1 The Experiment

The objective of Fermilab Tevatron experiment E710¹ was the measurement of the differential $\bar{p}p$ elastic and diffractive cross sections (p and \bar{p} refer to proton and antiproton, respectively). These measurements were taken at center of mass (c.m.) energies $\sqrt{s} = 1.02$ and 1.8 TeV, and the parameters extracted were the total cross section σ_t , the nuclear slope parameter B , the nuclear curvature parameter C , the ratio of the real to the imaginary part of the forward nuclear scattering amplitude ρ , the total elastic cross section σ_{el} , and the single diffractive cross section σ_{sd} . This thesis presents results from the analysis of E710 data with concentration on the measurements of σ_t , B , and ρ , and discusses the implication of these results on the field of elastic scattering.

This section describes the background of the field and the development of the motivation for E710. Appendix A explains the notation and kinematics of elastic scattering.

1.2 History of the Field

Since the mid 1960s, a large number of pp and $\bar{p}p$ elastic scattering and total cross section measurements have been carried out at facilities in Europe and the United States. The earliest of these were pp fixed target measurements, made at Brookhaven AGS[3] and Serpukhov[4] at c.m. energies

¹The E710 Collaboration:

Universita di Bologna and Istituto Nazionale di Fisica Nucleare, Bologna, Italy: M. Bertani, G. Giacomelli, I. Veronesi, M. Mondardini, S. Zucchelli

Cornell University, Ithaca, New York 14853: N. Amos, J. Orear

Fermi National Accelerator Laboratory, Batavia, Illinois 60510: C. Avila, W. Baker, B. Gomez, J. Negret, S. Pruss, R. Rubinstein

George Mason University, Fairfax, Virginia 22030: R. Ellsworth

University of Maryland, College Park, Maryland 20742: D. Dimitroyannis, J. Goodman, G. Yodh

Northwestern University, Evanston, Illinois 60208: M. Block, C. Guss, S. Sadr, S. Shukla

up to 10 GeV. They measured the pp cross section $\sigma_t(\text{pp})$, and ρ_{pp} . The cross sections were found to be approximately constant at about 40 mb. It was thought at that time that the cross section would remain constant with increasing energy.

In the early 1970s, pp data taken at the CERN ISR[6] in the energy range $10 < \sqrt{s} \leq 62$ GeV showed that the pp cross section was not constant and was instead *rising* with energy, from about 40 mb at $\sqrt{s} = 5$ GeV to 43.5 mb at $\sqrt{s} = 62$ GeV.

A decade later, with the introduction of the \bar{p} beam into the ISR, $\bar{p}p$ colliding beam experiments were conducted both by the Northwestern-Louvain group[11] which measured σ_t , B , and ρ , and the Pisa-Stony Brook group[12] which measured σ_t , only. The $\bar{p}p$ cross section showed a dramatic decline from 50 mb at $\sqrt{s} = 5$ GeV, to a minimum of 41.5 mb at $\sqrt{s} = 20$ GeV, before rising to the $\sigma_t(\text{pp})$ value of 43.5 mb at $\sqrt{s} = 62$ GeV.

The ISR experiments also indicated that ρ_{pp} and $\rho_{\bar{p}p}$ approach each other with increasing energy. $\rho_{\bar{p}p}$ is constant at around 0 in the interval $10 < \sqrt{s} < 20$ GeV before rising to 0.10 at $\sqrt{s}=53$ GeV. ρ_{pp} , on the other hand, rises from -0.27 at $\sqrt{s}=5$ GeV to 0 at $\sqrt{s}=23$ GeV, before rising to 0.08 at $\sqrt{s}=62$ GeV, which is within errors of the 0.10 value of $\rho_{\bar{p}p}$.

The nuclear slope parameter B is defined as the rate of change, with respect to t (the square of momentum transfer), of the logarithm of the differential nuclear cross section, evaluated at $t = 0$, or $B \equiv \left(\frac{d}{dt} \log \frac{d\sigma_n}{dt} \right)_{t=0}$. The ISR experiments demonstrated that B_{pp} and $B_{\bar{p}p}$ also approach each other with increasing energy. B_{pp} rises from 9.5 (GeV/c)^{-2} to $12.5 \text{ (GeV/c)}^{-2}$ in the interval $5 < \sqrt{s} < 62$ GeV, while $B_{\bar{p}p}$ stays at about 12 (GeV/c)^{-2} over this energy range. For pp and $\bar{p}p$, therefore, σ_t , B , and ρ appeared to converge with increasing energy. This also indicates that, at high energies, there is no difference between pp and $\bar{p}p$ scattering. The nuclear curvature parameter C is defined as $C \equiv \frac{1}{2} \left(\frac{d^2}{dt^2} \log \frac{d\sigma_n}{dt} \right)_{t=0}$. At the ISR, C was measured to be about 5 (GeV/c)^{-4} [1,44]. Also, the ratio of the elastic to total cross section σ_{el}/σ_t was measured to be

about 0.17. The significance of the latter two quantities will be discussed in Section 1.3.

The next high energy measurements were taken in 1983-4 when $\bar{p}p$ experiments at $\sqrt{s}=540$ and 546 GeV were conducted at the S $\bar{p}p$ S collider by the UA1 and UA4 collaborations. The former group reported a total cross section[8] of $67.6 \pm 0.5 \pm 2.7$ mb at $\sqrt{s}=540$ GeV, and the latter[9] 61.9 ± 1.5 mb at $\sqrt{s}=546$ GeV. Additionally, the UA5 collaboration reported a total cross section of $65.3 \pm 0.7 \pm 1.5$ mb at $\sqrt{s}=900$ GeV[29]. All of these values indicate a rise of cross section with energy. A rise is seen also for measured B values of 15.2 ± 0.2 (GeV/c) $^{-2}$ from UA4 and 17.1 ± 1.0 (GeV/c) $^{-2}$ from UA1. They also measured the ratio σ_{el}/σ_t to be about 0.22.

The UA4 ρ value of 0.24 ± 0.04 was surprisingly large. Models which had successfully predicted σ_t and B at the UA4 energy were not able to justify this high ρ value. It created a great deal of controversy which would not be resolved for almost a decade.

1.3 Interpretation of the Results and Motivation for E710

The original Pomeranchuk theorem states that if pp and $\bar{p}p$ cross sections become constant asymptotically and if ρ increases less rapidly than $\log s$, then the σ_t , B , and ρ values of the pp and $\bar{p}p$ systems become equal asymptotically[17]. The early pp results from the Brookhaven AGS[3] and Serpukhov[4] at c.m. energies up to 10 GeV indicated constant cross section values, and thereby seemed to confirm the first premise of the Pomeranchuk theorem. Later on, the data taken at the CERN ISR in the energy range $16 \leq \sqrt{s} \leq 62$ GeV showed that the cross section does *not* become constant asymptotically, and that the original Pomeranchuk theorem was not applicable. To account for this rise of the cross sections, the Pomeranchuk theorem was generalized[18] to state that as $s \rightarrow \infty$, $\sigma_t(pp)/\sigma_t(\bar{p}p) \rightarrow 1$. It is *not* required, however, that the difference in the cross sections go to zero, or even a non-zero constant as $s \rightarrow \infty$ [44]. Eden and Kinoshita showed that if both cross sections grow as $\log^\gamma s$ asymptotically, then their difference cannot grow faster than

$\log^{\gamma/2} s$ [18].

According to a derivation by Froissart[13] and later by Martin[14], the upper bound of the rise of pp and $\bar{p}p$ cross sections with s is $(\pi/m_\pi^2) \log^2(s/s_0)$, where m_π is the rest mass of the pion, and s_0 is a scale factor. This principle, known as the Froissart bound, dictates that σ_t cannot asymptotically rise faster than $\log^2 s$. Cornille and Martin[19] proved that inside the forward diffraction peak, at a given s and t , the ratio of the pp and $\bar{p}p$ *differential* cross sections asymptotically approaches unity, although their difference may not. A consequence of this theorem is that the ratio of the slope parameters goes to unity, i.e., $B_{pp}/B_{\bar{p}p} \rightarrow 1$, as $s \rightarrow \infty$. Furthermore, Block and Cahn[44] have derived the corollary that the ratio of the *squares* of the ρ values asymptotically goes to unity, i.e., $(\rho_{pp}/\rho_{\bar{p}p})^2 \rightarrow 1$, as $s \rightarrow \infty$.

The curvature parameter C was defined in Section 1.2. If the nucleon behaves as a sharp-edged disk of radius R , this curvature parameter would be negative and have a value of $-R^4/192$. As mentioned in Section 1.2, C was measured to have positive values at the ISR energy of $\sqrt{s} = 62$ GeV, and at the S $\bar{p}p$ S energy of $\sqrt{s} = 540$ GeV. These positive values of C indicate that at ISR and S $\bar{p}p$ S energies, the nucleon does *not* behave as a sharp disk.

In the mid 1980s, Block and Cahn[1] found the energy dependence of the forward scattering amplitude by making an asymptotic amplitude analysis fit of σ_t and ρ , for pp and $\bar{p}p$, in the energy interval $5 \leq \sqrt{s} \leq 62$ GeV. From this they extracted the energy dependence of the cross section at *higher* energies. They then put this energy dependence into the Chou–Yang model[20,21]. This model postulates that elastic scattering is the shadow of the absorption resulting from the passage of one hadronic matter distribution through another[44]. The scattering amplitude (see Section 6) is expressed in terms of an eikonal factorizable into functions of the impact parameter b and the c.m. energy s . Using the Durand and Lipen[21] assertion that the transverse matter distribution has the same shape as that of the charge distribution, the eikonal was fixed by Block and Cahn to

have the energy dependence obtained from the asymptotic analysis fit to the world data. The point here is that since the Chou–Yang model depends on b , it allows the calculation of the *differential* cross section $d\sigma/dt$ as a function of t . For the ISR energy of $\sqrt{s} = 62$ GeV and the SppS energy of $\sqrt{s} = 540$ GeV, the curvature parameter C was calculated to be positive, in agreement with the experimental results[1,44,51]. The Chou–Yang model evolves into a black disk as energy increases. Since a sharp disk exhibits negative curvature, C must equal zero at some energy, and eventually become negative. Block and Cahn proceeded to define ‘asymptopia’ as the energy domain where the elastic differential cross section is basically indistinguishable from that of sharp disk[44]. The quantitative indicator of the *onset* of asymptopia is the energy at which $C = 0$, which Block and Cahn predicted, using the above model, to be near the Tevatron energy of 1.8 TeV[53].

For a black disk model, the ratio $\sigma_{el}/\sigma_t = 1/2$. This ratio was measured to be 0.17 at the ISR[15], and 0.22 at the SppS[16].

Experiment E710, the highest energy ($\sqrt{s} = 1.8$ TeV) elastic scattering experiment to date, was conceived in order to achieve the following objectives²:

- To observe the trend in the rise of σ_t , B , and σ_{el}/σ_t with increasing energy, and to determine whether the Froissart bound holds at high energies.
- To test the validity of the prediction of Block and Cahn regarding the onset of asymptopia, by measuring the curvature parameter C at $\sqrt{s} = 1.8$ TeV to see if it is zero.
- To check the validity of the UA4 ρ value of 0.24 ± 0.04 .
- To measure diffractive dissociation and the single-diffractive cross section.

²It should be noted that although the main objective of E710 was the measurement of elastic scattering at $\sqrt{s} = 1.8$ TeV, data were also taken at lower energies of 1020, 546, and 300 GeV. Due to enormous amounts of background noise, only the 1020 GeV data have been analyzed, the results of which is discussed in this thesis. Data taken at lower energies have thus far been unusable.

1.4 Results of E710 and its Contemporaries, and their Significance

In 1989, E710 announced their initial $\bar{p}p$ measurements of $\sigma_t = 78.3 \pm 5.9$ mb and $B = 16.3 \pm 0.5$ (GeV/c) $^{-2}$ at $\sqrt{s} = 1.8$ TeV[24]. They also measured the elastic cross section of $\sigma_{el} = 19.6 \pm 3.0$ mb, and the ratio σ_{el}/σ_t of 0.25 ± 0.02 . They normalized their data according to their knowledge of the accelerator luminosity, which was known with an uncertainty of about 15%. E710 eventually superseded this cross section value by adopting a luminosity-free approach to normalizing their data[41].

In 1990, Kang and White[25] attempted to explain the large UA4 ρ value by postulating that it signals the presence of a genuine physical threshold just below 540 GeV. They suggested identifying this threshold with diffractive production of a new η particle composed of color sextet quarks, and with mass of ~ 30 GeV. The asymptotic model based on this hypothesis and fitted to the world data at the time would generate a cross section of 78.5 mb at $\sqrt{s} = 1.8$ TeV which was in excellent agreement with the E710 value, and a ρ of 0.22 at $\sqrt{s} = 540$ GeV which agreed well with the UA4 result. As we shall discuss in detail in Section 6, the Regge pole model of Landshoff and Donnachie[52], and later the analytic asymptotic amplitude analysis of Block and White[51] and the QCD-inspired eikonal model of Block, Halzen, and Margolis[49] all agreed with each other and gave a value of $\rho_{\bar{p}p} \approx 0.12$ – 0.14 !

At the time, E710 and CDF had completed acquisition of their respective data at $\sqrt{s} = 1.8$ TeV. For E710, the data were basically the same as those which led to their 1989 results. This time, however, they successfully removed the effects of the large background noise due to beam halo and therefore probed deeply into the low $|t|$ regions, in order to measure ρ as well as σ_t and B . In 1990, they published the results of a luminosity-independent measurement of the total ($\sigma_t = 72.1 \pm 3.3$ mb), elastic ($\sigma_{el} = 16.6 \pm 1.6$ mb), and total single-diffractive ($2\sigma_{sd} = 11.7 \pm 2.3$ mb) cross sections[41]. A year later, they announced simultaneously fitted values of $\sigma_t = 72.8 \pm 3.1$

mb, $B = 16.99 \pm 0.47 \text{ (GeV/c)}^{-2}$, and $\rho = 0.140 \pm 0.069$ [26]. These results were in excellent agreement with existing models, and they were the first pieces of evidence that suggested that the UA4 result may be incorrect. The E710 ρ value was a major factor that motivated the formation of the UA4/2 collaboration, whose mission was a precise re-measurement of ρ at $\sqrt{s} = 546 \text{ GeV}$. E710 also independently used data collected by higher $|t|$ detectors[53] to obtain the nuclear slope parameter $B = 16.26 \pm 0.23 \text{ (GeV/c)}^{-2}$ and the curvature parameter $C = 0.14 \pm 0.70 \text{ (GeV/c)}^{-4}$. This curvature parameter value is compatible with zero, and along with the positive curvature values reported by the lower energy data, signals the onset of ‘asymptopia’ at $\sqrt{s} = 1.8 \text{ TeV}$. This shows that 1.8 TeV is the transition energy signaling the onset of asymptopia, as predicted by Block and Cahn[1]. Also, the measured cross sections were well fitted by the QCD prediction of Block, Halzen, and Margolis[49]. Future high energy experiments (16 TeV at the LHC and 40 TeV at the SSC) are expected to measure negative nuclear curvature values.

Also in 1991, the CDF collaboration at Fermilab announced that at $\sqrt{s} = 1.8 \text{ TeV}$, $\sigma_t = 72.0 \pm 3.6 \text{ mb}$, $\sigma_{el} = 16.5 \pm 1.5 \text{ mb}$, and $B = 16.5 \pm 0.76 \text{ (GeV/c)}^{-2}$ [27]. These results were in excellent agreement with those of E710.

In 1993, the UA4/2 group, announced the highly anticipated $\rho_{\bar{p}p}$ value at $\sqrt{s} = 546 \text{ GeV}$ to be 0.135 ± 0.02 [22], thus refuting the large UA4 ρ value, along with the theoretical models constructed to explain it. This was a victory for the Regge pole, the analytic asymptotic amplitude, and the eikonalized QCD models. As a final confirmation, E710, in a re-analysis of the $\sqrt{s} = 1.8 \text{ TeV}$ data which allowed them to penetrate even deeper into the low $|t|$ region, measured $\rho_{\bar{p}p}$ to be 0.134 ± 0.069 at $\sqrt{s} = 1.8 \text{ TeV}$. The analysis leading to this result is discussed in this work.

Later that year, E710 measured the single-diffractive dissociation cross section[32] at $\sqrt{s} = 1.8 \text{ TeV}$ using a different set of detectors from those used for the 1990 single-diffractive results[41]. They announced a value of $2\sigma_{sd} = 8.1 \pm 1.7 \text{ mb}$ which was in reasonable agreement with the 1990

\sqrt{s} (GeV)	Experiment	σ_t (mb)	B ((GeV/c) ⁻²)	ρ	σ_{el}/σ_t
1800	E710	72.2±2.7	16.72±0.44	0.134±0.069	0.230±0.024
1020	E710	61.6±5.7	16.20±0.70		
546	UA4/2			0.135±0.02	

Table 1: Recent experimental results at high energies

results.

The E710 and UA4/2 results for σ_t , B , ρ , and σ_{el}/σ_t are shown in Table 1.³ This table summarizes the latest experimental information on elastic scattering. These results indicate a continuation of the rise of the cross section with energy.

E710 has achieved its objectives by showing that:

- σ_t and B increase with s .
- σ_{el}/σ_t increases with s , indicating the nucleon is getting blacker.
- $C \approx 0$ at $\sqrt{s} = 1.8$ TeV, in contrast to positive values at lower energies. This signals the onset of asymptopia, and the transformation of the nucleon to a black disk.

³In a recent set of preprints, CDF announced a new cross section of 80.0 ± 2.2 mb, which is in marked disagreement with their earlier result of 72.0 ± 3.6 mb obtained from the same data sample. There is no discussion in these preprints of the earlier results, and no explanation has yet been offered for the difference between the two values. In this work, the original results are used in the theoretical analysis.

2 Procedure

2.1 Experimental Strategy

In this experiment, the quantity of interest is the differential elastic cross section $d\sigma_{el}/dt$, which is obtained from the differential count dN/dt . For a given bin, $dN(t)/dt$ is the number of counts within a small interval dt around the t at the center of the bin. This quantity must be normalized to yield $d\sigma_{el}/dt$:

$$\frac{dN}{dt} = \mathcal{L} \frac{d\sigma_{el}}{dt}, \quad (1)$$

where \mathcal{L} is the luminosity and has the dimension of (area) $^{-1}$; the unit for its measurement is the inverse of the unit for cross section, i.e., mb $^{-1}$, pb $^{-1}$, etc. The expression for the differential elastic cross section $d\sigma_{el}/dt$ is given in Eq. 113 of Appendix A. There are several methods of fitting Eq. 1 to the data in order to extract σ_t , B , and ρ :

One method is referred to as Coulomb normalization. The t value at which the nuclear and Coulomb amplitudes are equal is referred to as the interference region t_{int} . If the experiment can cover $|t|$ values lower than $|t|_{int}$, namely, into the Coulomb region, then the Coulomb term dominates the differential elastic cross section, i.e., $d\sigma_e/dt \approx 4\pi(\alpha/t)^2$. Note that this expression does not depend on σ_t , B , and ρ . It therefore allows the direct determination of the luminosity, i.e., an *absolute* normalization of the experiment. Using Eqs. 113 and 1, the number of events in the interval dt can be written as

$$\frac{dN}{dt}(t) = \mathcal{L}\pi \left[\left(\frac{2\alpha}{|t|} \right)^2 G^4(t) + (\rho + \alpha\phi) \frac{\alpha\sigma_t}{\pi} \frac{G^2(t)}{|t|} e^{\frac{Bt}{2}} + \left(\frac{\sigma_t}{4\pi} \right)^2 (1 + \rho^2) e^{Bt} \right]. \quad (2)$$

Using Eq. 2, one can fit \mathcal{L} , σ_t , B , and ρ simultaneously. The slope parameter is determined primarily by the nuclear (third) term, and ρ primarily by the interference (second) term.

A second way to measure elastic scattering is the luminosity-free method. Experiments have

shown that the nuclear elastic cross section in small $|t|$ can be adequately parametrized as

$$\frac{d\sigma_n}{dt} = \frac{d\sigma_n}{dt} \Big|_{t=0} e^{Bt}, \quad (3)$$

i.e., B is the slope of the straight line obtained from plotting $\log(d\sigma_n/dt)$ vs $|t|$ in the small $|t|$ region. The differential nuclear cross section at $t = 0$ can be expressed in the following manner:

$$\begin{aligned} \frac{d\sigma_n}{dt} \Big|_{t=0} &= \frac{\pi}{p^2} \frac{d\sigma_n}{d\Omega} \Big|_{t=0} \\ &= \frac{\pi}{p^2} |\text{Re}f(0) + i \text{Im}f(0)|^2. \end{aligned} \quad (4)$$

where $f(0)$ is the nuclear scattering amplitude evaluated at the center of mass frame at $t = 0$.

Introducing $\rho \equiv \text{Re}f(0)/\text{Im}f(0)$, Eq. 4 can be rewritten as

$$\begin{aligned} \frac{d\sigma_n}{dt} \Big|_{t=0} &= \pi \left| \frac{(\rho + i)\text{Im}f(0)}{k} \right|^2 \\ &= \pi \left| \frac{(\rho + i)\sigma_t}{4\pi} \right|^2, \end{aligned} \quad (5)$$

where the last step used the optical theorem, Eq. 98. The total elastic cross section σ_{el} can be expressed as $\int_{-\infty}^0 (d\sigma_n/dt) dt$. Substituting for $d\sigma_n/dt$ from Eqs. 3 and 5, and performing the integration, we obtain

$$\begin{aligned} \sigma_{el} &= \frac{1}{B} \frac{d\sigma_n}{dt} \Big|_{t=0} \\ &= \frac{\sigma_t^2 (1 + \rho^2)}{16\pi B}. \end{aligned} \quad (6)$$

The difference of the total and the elastic cross sections is the inelastic cross section σ_{inel} . The luminosity \mathcal{L} normalizes the number of counts to give a cross section, or

$$\sigma_{inel} = \frac{N_{inel}}{\mathcal{L}}, \quad (7)$$

or

$$\mathcal{L} = \frac{N_{inel}}{\sigma_{inel}}$$

$$\begin{aligned}
&= \frac{N_{inel}}{(\sigma_t - \sigma_{el})} \\
&= \frac{N_{inel}}{\sigma_t \left[1 - \frac{\sigma_t(1+\rho^2)}{16\pi B} \right]}, \tag{8}
\end{aligned}$$

where the last expression uses the expression for σ_{el} in Eq. 6. The expression for \mathcal{L} (Eq. 8) can alternatively be used in Eq. 2 to normalize the number of counts, provided that the number of inelastic events N_{inel} is known.

If neither the measurement of the inelastic rate N_{inel} nor Coulomb normalization is possible, a third method is to use an independent measurement of the time-integrated luminosity \mathcal{L} . In this case, Eq. 2 is fitted to the data, where \mathcal{L} is fixed. Again the nuclear and interference terms would determine B and ρ , respectively. If data in the interference region is unavailable, i.e., if the minimum $|t|$ covered is large such that $|t|_{min} > |t|_{int}$, then there is not enough information about ρ to allow its determination, and it should be fixed.

Finally, it is obvious that an independent measurement of the integrated luminosity \mathcal{L} allows the determination of the total cross section σ_t from the total interaction rate N_t , or

$$\sigma_t = \frac{N_t}{\mathcal{L}}. \tag{9}$$

This is a fourth method for measuring the total cross section.

In this experiment the minimum $|t|$ covered by the detectors was low enough for the data to contain some Coulomb information, i.e., $|t|_{min} < |t|_{int}$. Furthermore, the number of inelastics N_{inel} and the time-integrated accelerator luminosity \mathcal{L} were known. Therefore, the second and third methods described above were *simultaneously* used to normalize the data.

2.2 Formulation of Experimental Procedure

To detect the scattered particles and to measure their scattering angles, detectors were placed about the interaction point at predetermined distances. These detectors measured the positions of

the scattered particles with respect to the beam line, and hence obtained the particles' scattering angles. Throughout this formulation, a right-handed coordinate system is used to identify the positions of the scattered particles. In this coordinate system, z is the beam direction, and x and y are the horizontal and vertical directions normal to the beam line, respectively.

One objective of experiment E710 was the measurement of elastic scattering at $|t|$ values low enough to yield information about the Coulomb region, i.e., to measure ρ by using the interference of the nuclear and Coulomb amplitudes. To do this, measurements had to be taken at very low scattering angles, which in turn required the placement of the detectors at large distances from the interaction point. The site assigned to E710 along the Tevatron Collider contained an asymmetric arrangement of bending magnets about the interaction point at large distances. This asymmetry was taken into account in the calculation of the angles of the scattered particles. The quantity "effective length" is the distance between a low $|t|$ detector and the interaction point which would result in the *same* measured scattering angle if there were *no* bending magnets in the way. Due to the asymmetry of the arrangements of the bending magnets about the interaction region, the effective lengths were different for the left and right sides of the interaction region. Furthermore, the bending magnets deflected the particle trajectories differently along the x and y directions. Therefore, for the same side, the effective lengths had different values in x and y .

Let us isolate from the data sample a subset corresponding to elastically scattered particles, detected by a detector on the right side of the interaction region, that were in coincidence with particles detected at a *point* on the left side detector. Conservation of momentum requires all of these right side particles to be concentrated also at a point subtending the same angle with respect to the beam line as the corresponding left side point (see Fig. 48). In fact, what one sees is a symmetric two-dimensional *distribution* of particles centered about this point on the right side. This also holds true with the two sides reversed. The size and shape of this distribution are

independent of its location. The width of this distribution is due to the size of the interaction region, the betatron oscillations, and the detector resolution. We will refer to this distribution as the elastic pattern.

Due to the asymmetry of the setup about the interaction region, it was convenient to re-scale all dimensions to correspond to a spatial frame in which the distances between the interaction region and the detectors were equal. In this new frame, the right side detectors were significantly larger than the left side, by a factor of 1.52 in x and 1.05 in y . As a result, the right side detectors covered more of the elastic pattern of the particles incident on the left side detectors than vice versa. Consequently, the event distributions of the left side detectors required less correction for acceptance, and were the only distributions used in the analysis. Each bin on the left side contained events coincident with the *entire* right side, so no differential right side information was used.

Let us assign to the left and right sides of the interaction region their own reference frames, with the coordinate system of the left frame identified by (x, y, z) , and that of the right frame by (x', y', z') such that under a transformation from the left side to the right, $x \rightarrow -x'$, $y \rightarrow y'$, and $z \rightarrow -z'$. Let us further identify the x and y effective lengths of the two sides as L_x , L_y , $L_{x'}$, and $L_{y'}$. Using the transport equation (Eq. 122) from the appendix section on the beam lattice (Appendix B), the positions, detected by the drift chambers, of an elastically scattered $p\bar{p}$ pair on each side of the interaction region can be expressed as

$$x = m_x[x_{int} + x_0] + L_x[\alpha_x + \Delta\alpha_x] + \delta_x, \quad (10)$$

$$x' = -m_{x'}[x_{int} + x_0] + L_{x'}[\alpha_x + \Delta\alpha_{x'}] + \delta_{x'}, \quad (11)$$

$$y = m_y[y_{int} + y_0] + L_y[\alpha_y + \Delta\alpha_y] + \delta_y, \text{ and} \quad (12)$$

$$y' = m_{y'}[y_{int} + y_0] - L_{y'}[\alpha_y + \Delta\alpha_{y'}] + \delta_{y'}, \quad (13)$$

where

m_x is the left side horizontal focusing factor, $m_{x'}$ is the right side horizontal focusing factor, etc.,

(x_{int}, y_{int}) are the coordinates of the interaction with respect to the mean interaction location,

(x_0, y_0) are the coordinates of the beam center with respect to the center of the detector system (the designated origin),

α_x and α_y are the x and y components of the scattering angle α ,

$\Delta\alpha_x$ is the betatron oscillation angle along x (same for $\Delta\alpha_{x'}$ along x' , etc.),

δ_x is the detector resolution for the measurement of the location of scattered particles at x , etc.

Both sides have a common origin at the geometrical center of the apparatus.

The interaction region, the betatron oscillations $\Delta\alpha$, and the detector resolution δ all contribute to broaden the elastic pattern.⁴ Each of these contributions is assumed to broaden the elastic pattern in a gaussian manner. The differential cross section must be corrected for this broadening by convoluting it with ten gaussians: two for the x and y components of the coordinate of the event with respect to the interaction point, four for the x and y components of the betatron oscillation angles on the left and right sides, and four for the x and y components of the detector resolutions on the two sides. All of these must be integrated with the x and y components of the scattering angle, resulting in a twelve-dimensional integration to be performed. It can be mathematically

⁴The interaction region also has a width in the z direction. This width was found to be exceedingly small (≈ 0.6 m) in comparison to the distances between the detectors and the interaction region (25–121 m), and was therefore ignored in this formulation.

shown that this large convolution collapses to one with only two gaussians, for x and y , the widths of which contain the effects of *all* of the factors which broaden the pattern (see Ref. [33]). This was experimentally verified when the projections of the elastic pattern on the xz and yz planes were observed to be gaussians. The widths of these gaussians are referred to as the pattern widths, and are identified by the symbols σ_x and σ_y (refer to the section on widths, Section 4.4).

The width of the elastic pattern results in large event losses in the vicinity of the physical boundaries of the detectors. The amount lost can be as much as 75% at an infinitesimal bin closest to the beam, i.e., the bin with the lowest $|t|$. In Figs. 19 and 20, the half-dashed gaussian represents the elastic pattern composed of particles coincident with the low $|t|$ stacks of the left side detector. The dashed part is the portion of the pattern that lies outside of the detector boundaries. Denoting the coordinates of an event on a left side detector as (x, y) , and (x', y') for a right side detector, the actual form of the differential elastic cross section $d\sigma_{el}/dt$ requires its convolution with a two-dimensional gaussian representing the elastic pattern. Thus, the *pattern corrected* elastic differential cross section is

$$\left. \frac{d\sigma_{el}}{dt} \right|_{corr} = \int_{x'_{min}}^{x'_{max}} \int_{y'_{min}}^{y'_{max}} \frac{d\sigma_{el}}{dt} \frac{e^{-\frac{1}{2}\left(\frac{x-x'}{\sigma_x}\right)^2}}{\sqrt{2\pi}\sigma_x} \frac{e^{-\frac{1}{2}\left(\frac{y-y'}{\sigma_y}\right)^2}}{\sqrt{2\pi}\sigma_y} dy' dx', \quad (14)$$

where

$x'_{min(max)}$ and $y'_{min(max)}$ are the boundaries of the right side detector, and

σ_x and σ_y are the x and y pattern widths.

The bin size should preferably be chosen small enough to allow its approximation as a point. In practice, this is not possible due to the requirement that each bin contain a minimum number of events (typically, about 10) for it to have any statistical significance. If the dimensions of a bin on the left side detector is denoted as $x_{min(max)}$ and $y_{min(max)}$ such that $\Delta x \equiv x_{max} - x_{min}$ and

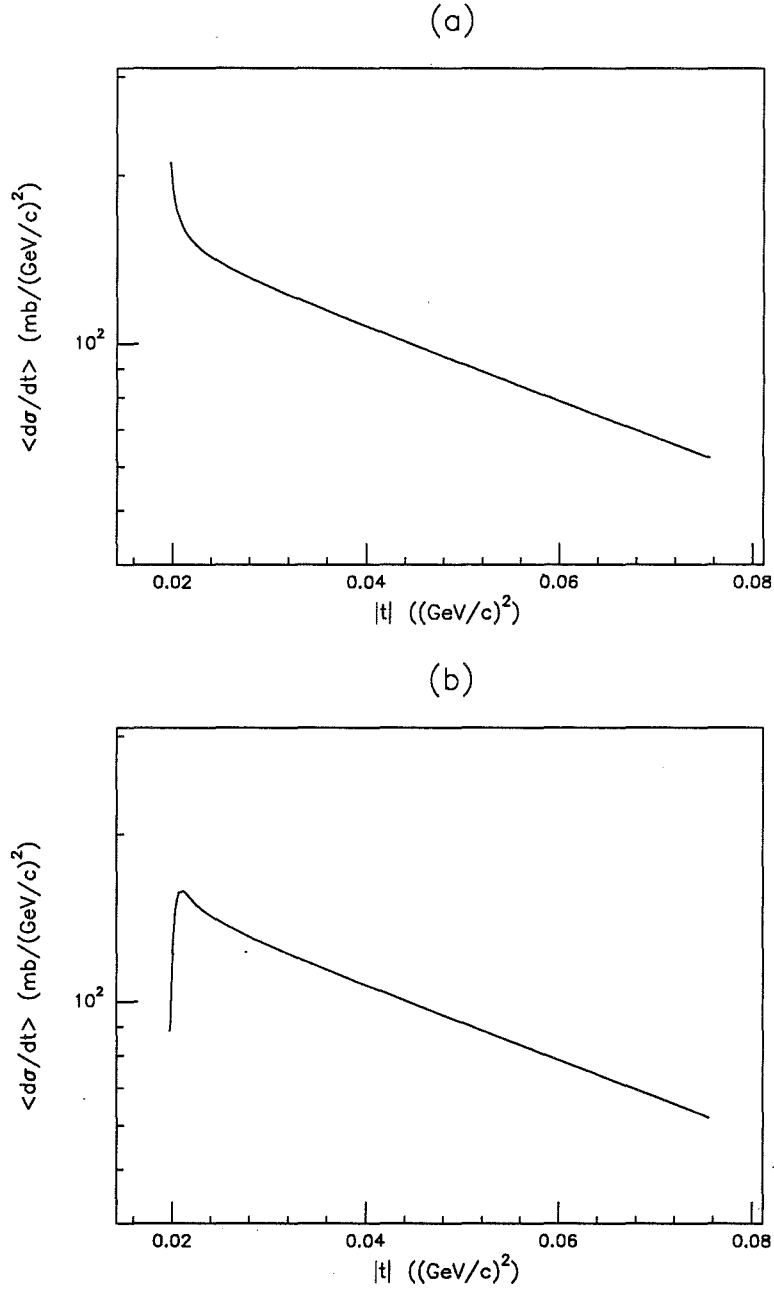


Figure 1: (a) The effective differential cross section vs $|t|$ for no event loss due to pattern width, (b) the expected loss of events at low $|t|$

$\Delta y \equiv y_{max} - y_{min}$, the pattern corrected differential cross section (Eq. 14) is thus averaged over

this bin. This average is the *effective* elastic differential cross section $\langle d\sigma_{el}/dt \rangle_i$ for bin i , or

$$\left\langle \frac{d\sigma_{el}}{dt} \right\rangle_i = \frac{1}{\Delta x \Delta y} \int_{x_{min_i}}^{x_{max_i}} \int_{y_{min_i}}^{y_{max_i}} \left. \frac{d\sigma_{el}}{dt} \right|_{corr} dy dx \quad (15)$$

The expression given in Eq. 15 is fitted to the number of counts $\Delta N_i/\Delta t$, where ΔN_i is the number of events in bin i , corrected for background and any inefficiencies, such as azimuthal coverage, dead time, etc. The quantity Δt is the interval in t covered by the bin. In this experiment, all bins are the same size, and therefore Δt is the same for all bins. Again, the data are normalized according to the second and third methods outlined in Section 2.1.

Fig. 1a is the plot of $\langle d\sigma_{el}/dt \rangle$ vs the $|t|$ value at the bin center, at $\sqrt{s} = 1.8$ TeV, if there were *no* loss of events near the detector boundaries due to the width of the elastic pattern. This figure shows a continual rise of the effective differential cross section with decreasing $|t|$. Due to the width of the elastic pattern, however, a significant loss of events is expected in the low $|t|$ bins, resulting in a drop of the effective cross section for these bins as shown in Fig. 1b. This effect is built into Eq. 15 which is fitted to the data.

3 Experimental Setup

3.1 The Tevatron Collider

Fig. 2[34] is a sketch of the aerial view of the accelerator ring of the Tevatron $\bar{p}p$ collider at the Fermi National Accelerator Laboratory (Fermilab) in Batavia, IL, USA. Protons are first accelerated to

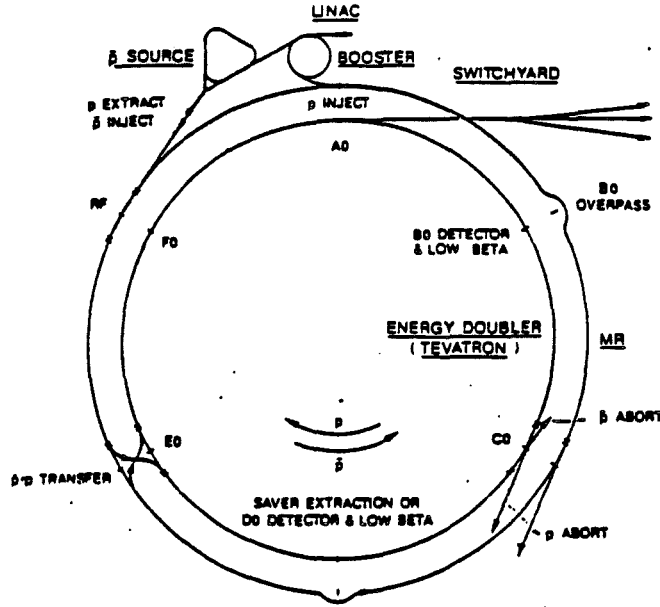


Figure 2: The Tevatron Main Ring, Energy Doubler, and \bar{p} source

200 MeV at the Linac, then sent to the booster where they are accelerated to 8 GeV, and from there to the Main Ring. At 150 GeV peak excitation, the Main Ring injects the protons into the Energy Doubler, a ring right beneath the Main Ring in the same tunnel. The Main Ring also extracts protons at 120 GeV and sends them back to the \bar{p} production target. An antiproton is produced for every 20,000 protons and then sent to the \bar{p} source which has two storage rings. The antiprotons are first sent to the “debuncher” ring where their narrow time spread is converted to a narrow momentum bunch spread. This allows them to enter the second “accumulator” ring. A flux of 6×10^{10} antiprotons per bunch are then injected back into the Main Ring, as are an order of magnitude higher number of protons per bunch. Both the p and the \bar{p} beams are accelerated in

the opposite directions up to energies of 0.9 TeV in the Energy Doubler ring. Each beam is divided into 6 bunches, and has a period of $21 \mu\text{sec}$ per revolution. Consequently, there are collisions every $3.5 \mu\text{sec}$ along six intersection regions A0, B0, C0, D0, E0, and F0.

3.2 The E710 Apparatus

Fig. 3 is a schematic of all of the detector systems used in the experiment. The Tevatron was

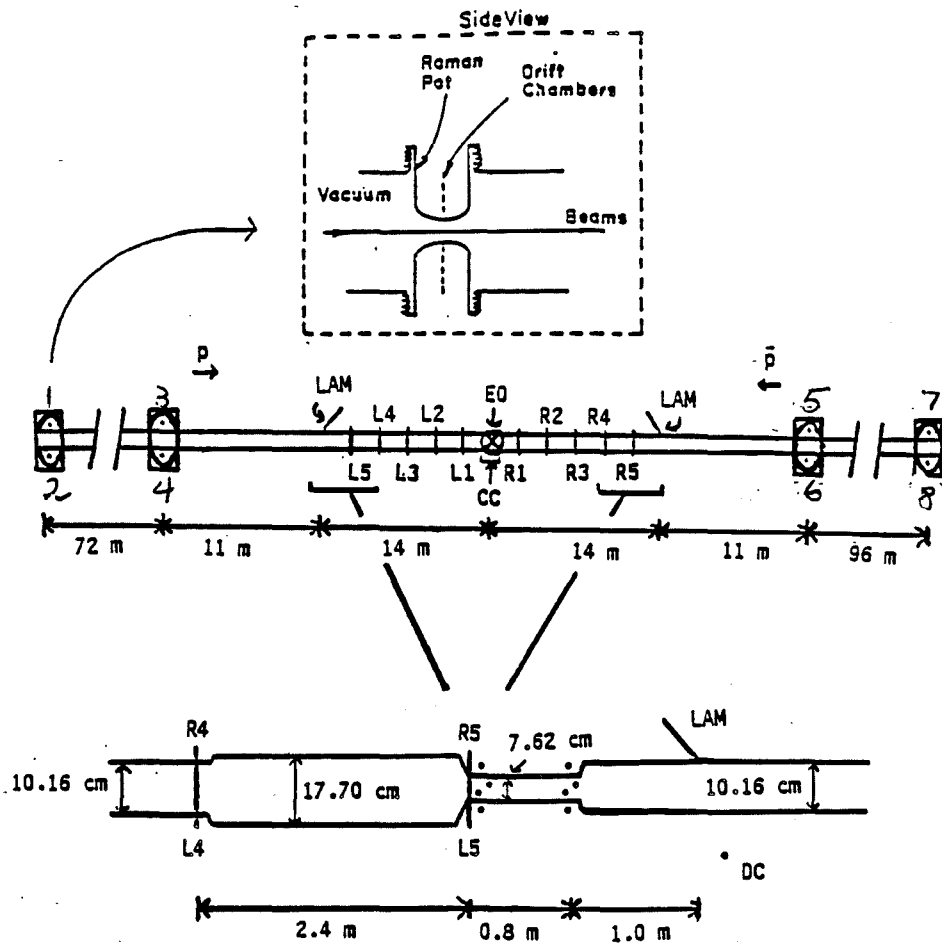


Figure 3: The E710 detector at the Fermilab Tevatron. Inset: Blow-up of the beam pipe at the positions of the tracking telescopes

designed prior to consideration of this experiment. Upon approval, E710 was assigned the E0

intersection region where, within 25 m of the interaction region, there were no correction magnets in the way to alter the trajectories of the beams. It was therefore possible to place four drift chambers symmetrically above and below the beam line inside the beam pipe on each side, 25 m from the interaction region. In Fig. 3, these chambers are labeled as 3, 4, 5, and 6, where 3 is the left arm, inner upper drift chamber above the beam, 4 is the left arm, inner down drift chamber below the beam, and so on. E0 marks the interaction region. These chambers allowed elastic scattering measurements down to $|t| = 0.006 \text{ (GeV/c)}^2$ at $\sqrt{s} = 1.8 \text{ TeV}$.

This minimum covered $|t|$ value was not low enough to allow penetration into the interference region (see Table 8 in Appendix A), so outer drift chambers were designed to be placed farther downstream from E0 on each side. This required finding available locations along the beam pipe considerably farther than 25 m from E0.

As Fig. 3 demonstrates, the arrangement of quadrupole magnets that stood between these outer drift chambers was not symmetric about E0 (also see Table 2). On the left side, the outer pots were placed 91 m from E0, and on the right, 124 m. The quadrupole magnets caused a deflection in the trajectories of the scattered charged particles on each side. Thus, the y (the vertical direction transverse to the beam line) positions of the elastic events in the outer chambers were measured as if the distance between the outer pots and E0 were 80 m on the left side and 76 m on the right, with *no* quadrupole magnets in between. In x (the horizontal direction transverse to the beam line), these distances were 45 m on the left and 30 m on the right. These distances are referred to as the y and x “effective” lengths L_y and L_x , respectively. If the coordinates of a point located to the left of E0 is specified as (x, y) , and that of a point to the right of E0 as (x', y') , then L_x and L_y are the left side effective lengths and $L_{x'}$ and $L_{y'}$ the right side. With these outer chambers, it was possible to obtain t coverage to as low as $|t| = 0.00075 \text{ (GeV/c)}^2$ at $\sqrt{s} = 1.8 \text{ TeV}$, i.e., into the Coulomb side of the interference region. The drift chambers located 25 m from E0 are hereby

	Distance from E0 (m)	Side
inner pots	25	\bar{p}
quadrupole magnet	27	\bar{p}
quadrupole magnet	33	\bar{p}
outer pots	91	\bar{p}
inner pots	25	p
quadrupole magnet	29	p
quadrupole magnet	35	p
quadrupole magnet	93	p
quadrupole magnet	94	p
quadrupole magnet	123	p
outer pots	124	p

Table 2: Positions of the quadrupole magnets between the inner and outer drift chambers on each side of E0

referred to as the inner or high $|t|$ chambers, and the ones located farther downstream as the outer, or low $|t|$. As Fig. 3 indicates, the outer chambers were identified according to the numbers 1, 2, 7, and 8, such that 1 is the left upper outer, 2 the left lower outer, and so on.

Due to the asymmetry of the setup about the interaction region, it was convenient to re-scale all dimensions to correspond to a spatial frame in which the distances between the interaction region and the detectors were equal. In this new frame, the right side detectors were significantly larger than the left side, by a factor of 1.52 in x and 1.05 in y . As a result, the right side detectors covered more of the elastic pattern of the particles incident on the left side detectors than vice versa. Consequently, the event distributions of the left side detectors required less correction for acceptance, and were the only distributions used in the analysis. Each bin on the left side contained events coincident with the *entire* right side, so no differential right side information was used.

To study elastic scattering at low $|t|$ values, the chambers had to be placed close to the circulat-

ing beams. Given the relatively large diameter (5 cm) of the Tevatron beam pipe, it was imperative to devise a scheme that would allow the detectors to penetrate into the pipe without affecting the near vacuum ($\approx 10^{-9}$ torr) condition inside it. To accomplish this objective, the chambers were encased inside mobile container units, called roman pots, that could move inside the beam pipe. A set of two roman pots, one above and the other below the plane of the accelerator, formed a castle, as shown in Fig. 4[35]. Each pot could be moved by remote control toward or away from

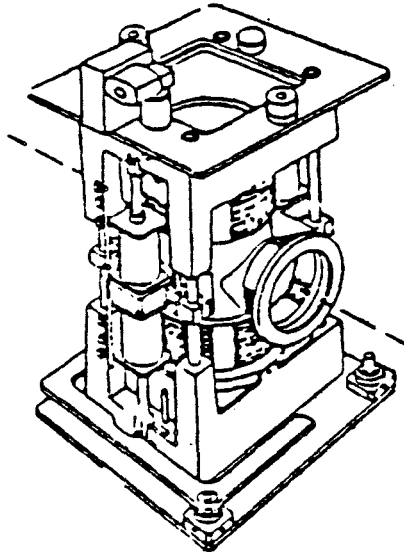


Figure 4: Two roman pots inside their housing, forming a castle. The dashed line indicates the beam axis. (Taken from Ref. [36])

the beam. To detect an elastic collision, a pair of inner or outer drift chambers were placed inside pots located diagonally with respect to the interaction region. As shown in Fig. 3, four such pairs, or combinations, existed. As mentioned earlier, the low $|t|$ data were gathered by the four outer drift chambers (1, 2, 7, and 8).

Behind each drift chamber, there were three scintillation counters. Two of these counters were identical and were used for triggering. They had 2 ns rise time photomultiplier tubes in order to have a fast trigger for tracks coming into the drift chambers. The third counter was smaller than

the other two. It had small holes drilled into it and was placed behind the trigger counters to provide a known spatial reference frame for calibrating the event coordinate readout system.

In order to approximate 4π angular coverage, ten ring scintillation counters were used on each side of E0 around the beam pipe for measurement of inelastic scattering, and eight central counters covering E0. In Fig. 3, the five left ring counters are identified as L1-L5, and the five right ring counters as R1-R5. The central counters are identified as CC.

The Lambertsons (identified as LAM in Fig. 3) are the bending magnets that direct the p and \bar{p} beams from the Main Ring to the Energy Doubler. Their placement close to the detectors was cause for concern about beam halo background being deflected toward the detectors. To deal with this problem, 16 tracking drift chambers were placed on each side of E0 around the beam pipe next to the L5 and R5 ring counters. These chambers were used for tracking events to determine whether they originated at the vertex. They were also used to measure beam gas background.

3.3 The Elastic Scattering Detectors

3.3.1 Geometry of the Drift Chambers

As mentioned earlier, the drift chambers were used to measure the spatial coordinates of the scattered particles. Each chamber consisted of 4 horizontal 30 mm long sense wires spaced 6 mm apart. The chambers were filled with 50-50% argon-ethane mixture. They had 1 kV/cm drift field and 23 mm drift distance (see Fig. 5)[35]. For mechanical stability, the chamber body was milled from a block of stesalite 4411-W. Voltages were distributed to the field wires through a printed circuit glued on the side faces of the chamber body. The wires were held with crimp pins which contacted directly the printed circuit without soldering.

The signal from each wire was preamplified with a $20\ \Omega$ input impedance through high voltage decoupling capacitors and an impedance matched line built in the printed circuit. The geometry

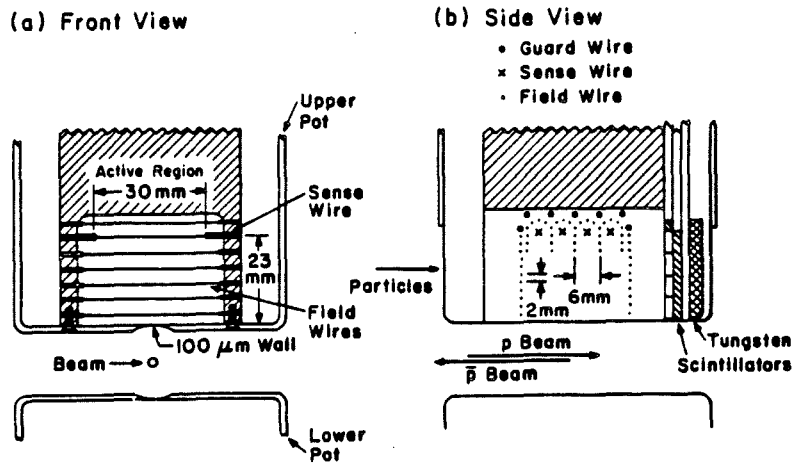


Figure 5: Geometry of the drift chambers for (a) front and (b) side views

shown in Fig. 5 provides a uniform drift field as shown in Fig. 6a where the drift potential distribution is 50 V/line. The pots also had good drift characteristics. Fig. 6b is a map of computed drift times whose distribution is 5 ns/line, or approximately 0.25 mm per line. The bottom plate is grounded, the field wires' voltages increased by 200 V per step up to the arcade voltage of 2200 V. The drain wires were at 2500 V, and the sense wires at 3950 V corresponding to a 1750 V multiplication voltage drop in a 6 mm diameter cage.

The signal was locally amplified and discriminated and then sent to the counting room along 120 m shielded twisted pair cables. There the signal was digitized by 4-D modules[38].

The coordinate of the incident particle in the x direction (along the length of the wire) was needed in order to obtain the azimuthal component of its scattering angle and was read by charge division. The 4-D module digitized the signal into 64 bins in the x direction, where each bin was calibrated to correspond to about 0.5 mm. The x readout displayed nonlinearities that made it imperative that the data be integrated over the entire x range.

The y coordinate of the incident particle was needed to obtain the polar component of its scattering angle, and was digitized into 512 drift-timed bins. Each bin was then calibrated to

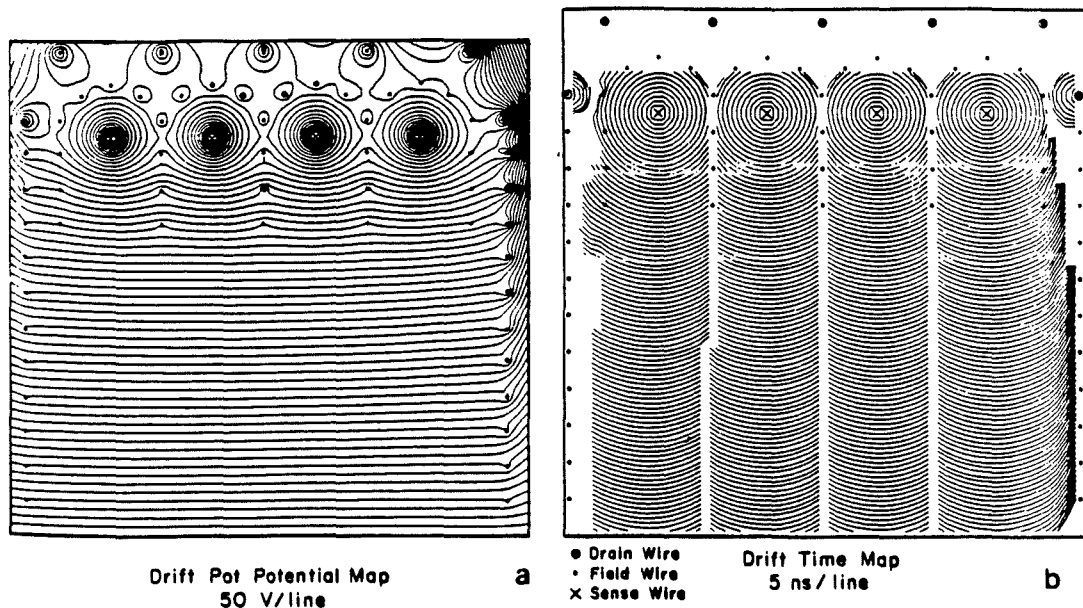


Figure 6: (a) Map of computed drift potentials, (b) Map of computed drift times

correspond to about 65 microns.

3.3.2 Scintillation Counters Inside the Roman Pots

As mentioned earlier, next to each roman pot there were three scintillation counters, where two were used for triggering and the third for the calibration of the coordinate readout system. The former are referred to as the trigger counters, and the latter as the calibration counter. The three counters were housed behind each pot with the first counter covering most of the active area of each chamber. The dimensions of the trigger counters were 22 mm \times 28 mm \times 3.2 mm, and the calibration counter 18 mm \times 20 mm \times 3.2 mm (Fig. 7).

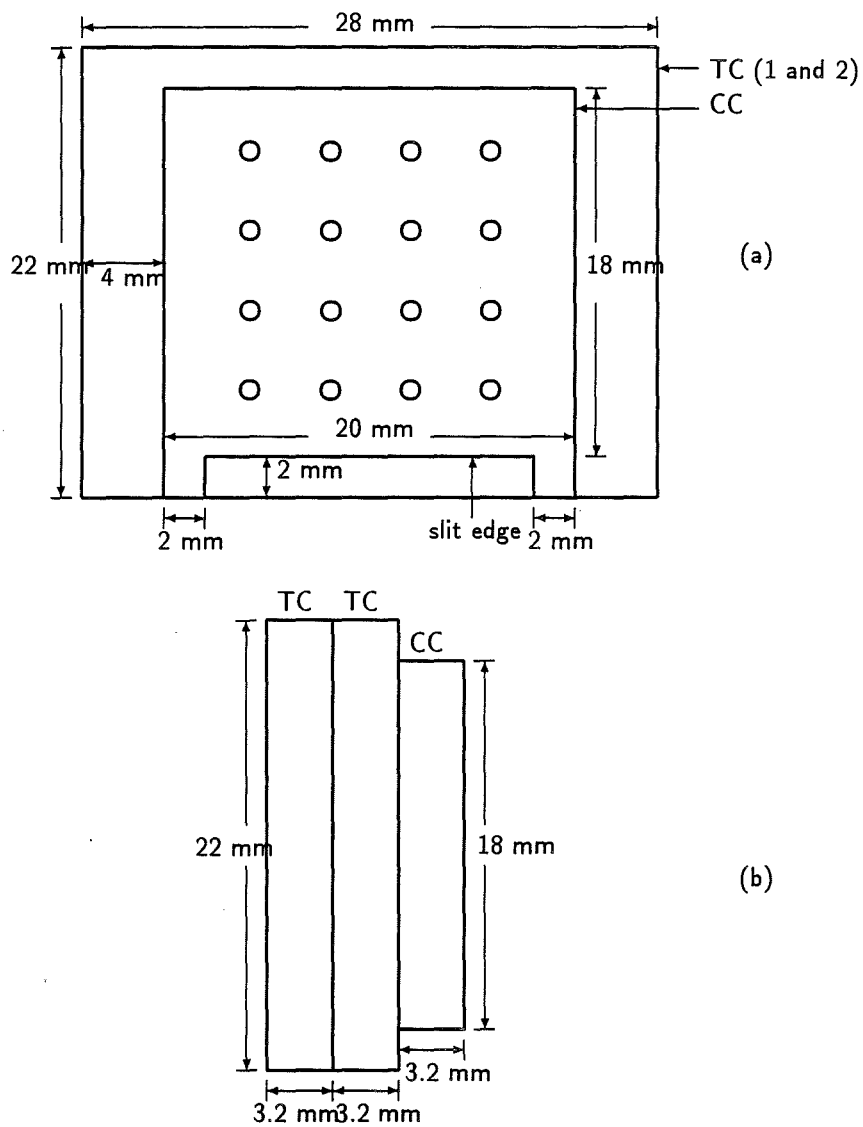


Figure 7: (a) Front and (b) side views of the trigger counters (TC) and the calibration counter (CC)

3.4 The Inelastic Scattering Detectors

3.4.1 The Ring Scintillation Counters

The geometries of the left and right ring scintillation counters are shown in Fig. 8. There were 10

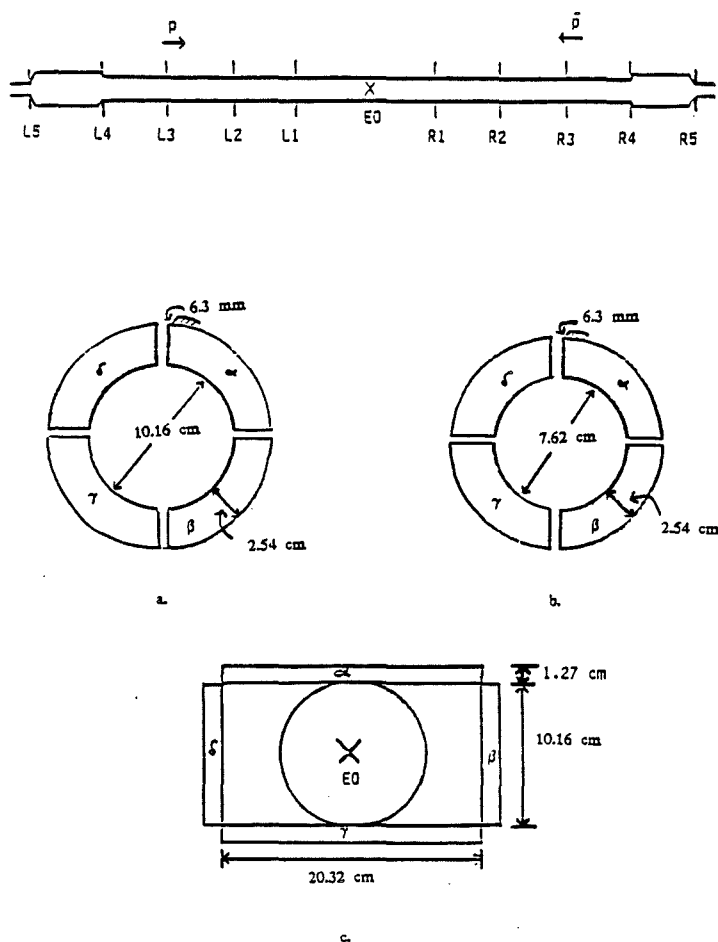


Figure 8: Geometries of the ring scintillation counters around the beam pipe: (a) Ring sets L0-L4, R1-R4, (b) L5, R5, and (c) center counters around E0

ring counter sections, 5 on each side, designated as L1-L5 and R1-R5. Each section subtended a circle around the beam pipe, and was composed of four identical quadrants, α , β , δ , and γ . In addition to these ten, there were another class of scintillation counters, called the central counters, which covered the E0 vertex on all sides. Four of the central counters were occasionally replaced with an L-shaped counter, L0, near E0 to accommodate various η coverages.

Table 3 is a list of the minimum and maximum acceptance angles of all of the ring counters. These counters were used for identification of inelastically scattered particles with high transverse

Counter Section	Distance from E0 (m)	Min. Acceptance Angle (mrad)	Max. Acceptance Angle (mrad)
L0	1.69	29.99	44.98
L1	2.64	19.25	28.87
L2	4.12	12.33	18.50
L3	6.96	7.30	10.95
L4	9.68	5.25	7.87
L5	12.16	3.13	5.22
R1	3.32	15.29	22.94
R2	4.78	10.62	15.93
R3	6.89	7.37	11.06
R4	10.17	4.99	7.49
R5	12.69	3.00	5.00

Table 3: Angular acceptance ranges of the ring counter sections and their distances from E0

momenta that registered a coincidence with a p or \bar{p} on the other side, or events identified by high transverse momentum particles on both sides. The former group are referred to as single diffractive events, and the latter as double diffractive.

3.4.2 The Tracking Telescopes

There were a number of factors that resulted in a significant amount of background noise. The sources of background were initially expected to be beam-gas interactions and single diffractive events. Later, it was found that another major source was beam halo that was deflected in the magnetic field of the Lambertsens. To keep track of this noise, a series of drift chambers, similar in construction to the ones used for elastic scattering measurements, were placed in front of

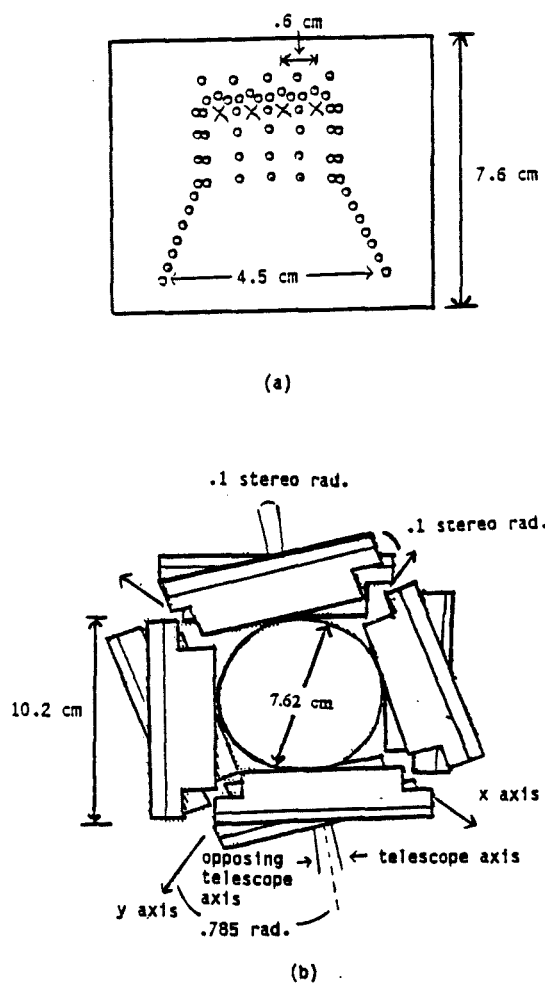


Figure 9: (a) Cross section of the tracking drift chambers, and (b) beam's eye view of the drift chamber telescopes

the Lambertsens on each side of E0 (Fig. 9). These chambers later proved effective in tracking inelastics from the interaction region and differentiating them from those resulting from beam-gas interactions.

A doublet, consisting of two sets of four chambers, were symmetrically placed around the beam pipe, rotated by ± 0.05 radians in drift direction from the vertical axis. This was done in order

to achieve a stereoscopic track reconstruction. These doublets were located along the beam pipe behind the L5 and R5 ring counters as well as 0.8 m downstream before the Lambertsons on each side. Their purpose was to measure the fraction of the time the background set off the single arm diffraction trigger in the logic electronics. A set of four chambers on each side was referred to as a tracking telescope. These chambers allowed measurements of track angles as low as 2.90 mrad.

As shown in Fig. 9, the tracking telescopes were 7.6 cm high and 10.2 cm wide. They were active 3.4 cm in drift direction and 8.9 cm in width. They were filled with a gas mixture of 80% argon and 20% carbon dioxide and designed to have an angular resolution of 0.19 mrad (0.15 mm in drift direction with a 0.8 m separation between the two sets of chambers in a doublet). Inside each chamber, four 8.9 cm long sense wires of 25 micron diameter were equally spaced and surrounded by 22 gauge field shaping wires. The outer field wires were set at 3.4 kV and the inner wires near the sense wires were set at 3.1 kV. This allowed the drift field to act on a larger active area than the drift chambers used for elastic scattering measurements.

The sense wires were placed transverse to the beam direction on all sides of the beam pipe. They were set at 4.8 kV and their signal was read out with preamplifiers. The differential output of the preamplification was sent by 75 m long twisted pair cable to an amplifier/discriminator. The output of all four sense wires were fed into a three-out-of-four majority logic. The output of this majority logic was converted to a standard NIM pulse that was sent into a time-to-digital converter to determine the drift time from the particle track to the sense wire[39].

The telescopes were fastened to an aluminum support that was bolted to the floor. A 25 cm thick layer of lead bricks was erected around the location of these chambers to provide shielding from lost protons emanating from the Main Ring.

4 Data Analysis

4.1 Event Selection

Elastic and inelastic events were read and recorded simultaneously. Therefore, the off-line analysis of the data had to distinguish the two types of events. A number of criteria were used to accomplish this:

4.1.1 TDC Windows

The first filtering criterion of the event selection procedure used the TDC windows. Lecroy 2228 TDCs, 2249 ADCs, and 2551 scalers were used for reading out event information from all scintillation counters. The event trigger was used as a start signal for the TDCs. Signals from the counters were digitized by the ADCs with 150 ns gates. The discriminated signals were sent as stop pulses to the TDCs. For each counter, a time distribution of events was obtained from the TDCs. These distributions were used to determine whether a hit in a counter was in time with the interaction at E0.

A typical TDC distribution for one of the trigger counters is displayed in Fig. 10.

4.1.2 Trigger Selection

Due to the large amount of background noise from the beam halo, particularly in the low $|t|$ region where practically all of the Coulomb information lies, it was imperative to separate the elastic signal from background. To do this, two different kinds of triggers were used. These triggers differed according to whether they corresponded to coincidences between detectors located *diagonally* about the interaction region, or the ones located on the *same side* of the beams.

A candidate for an elastic event was defined as one that registered a trigger in either, but not both, of the diagonal detector pairs 1-8 or 2-7, and no trigger in any other counter (See Fig. 3).

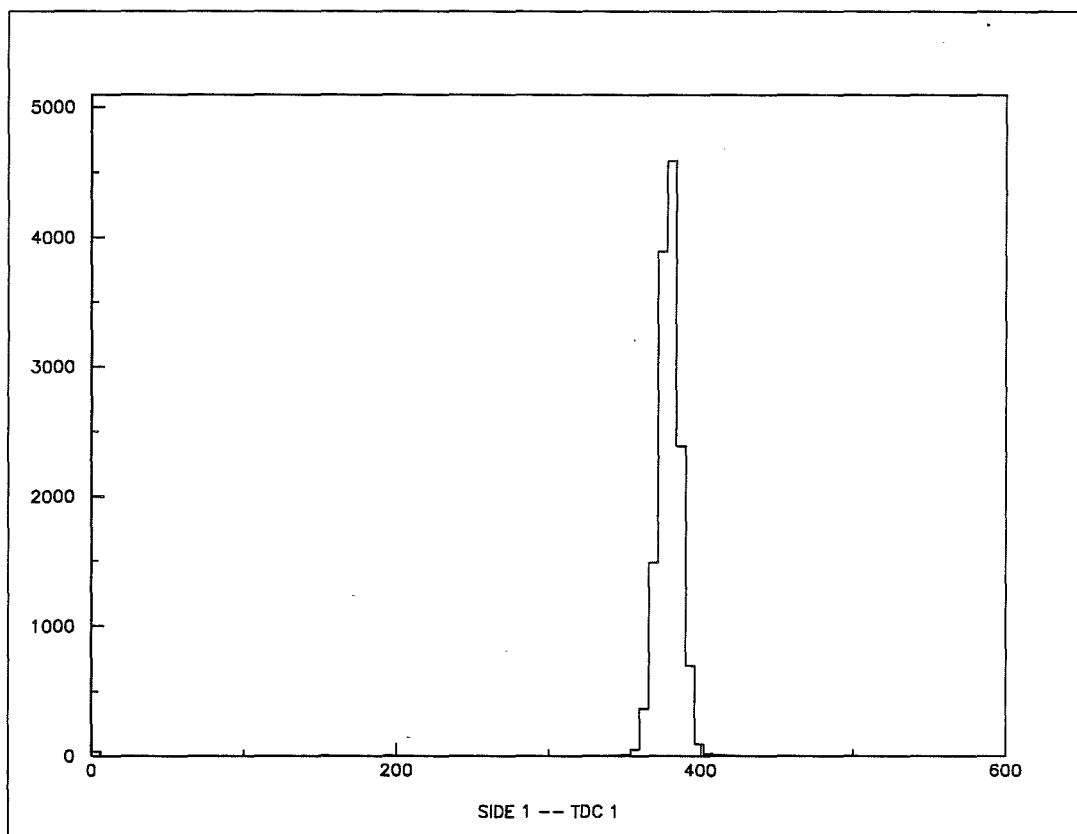


Figure 10: A typical TDC distribution

The sample of events satisfying this selection criterion contained the elastic signal as well as a significant amount of background noise due to beam halo, and is referred to as the elastic sample.

In addition to this, a sample was formed which contained events that registered a trigger on either of the parallel detector pairs, 1-7 or 2-8, but no trigger on any other chamber. This is referred to as the background sample.

4.1.3 Wire and Track Selection

Each drift chamber had four sense wires. At times, the output from one or two of these wires was not used due to low efficiency or exceedingly large number of double or more hits, i.e., events that registered more than one track with a given wire. A track is the computed coordinates of a detected particle. When filtering events based on their tracks, only the y coordinate was used since the measured x coordinate was generally not trusted.

Of the wires that *were* used, at least one was required to have a single hit. The remaining wires were required to have only single or double hits, i.e., if any one of them did not meet this condition, it was discarded *for that event*. Furthermore, it was required that at least two wires satisfy this criterion for the event to be accepted. The track of the wire with the single hit was then used as a reference with which the tracks of the other wires were compared. For the tracks from any two wires to be considered in agreement, they had to be within a specified tolerance of each other. The value of this tolerance was picked by trying a number of values and counting the total number of events after the filtering. The idea was to use the smallest tolerance possible without unnecessarily cutting off the amount of statistics. This tolerance was selected to be 0.7 mm. Fig. 11 shows this stability study for a number of tolerance values. Once agreement within the specified tolerances was established among the tracks, they were all arithmetically averaged and the result was taken as the coordinate of that event.

4.2 The Readout System

The mechanisms of the y and x readout systems are described in Section D.1.1. Here, the calibration procedures of these two systems are described.

Variation of Statistics with Y Tolerance

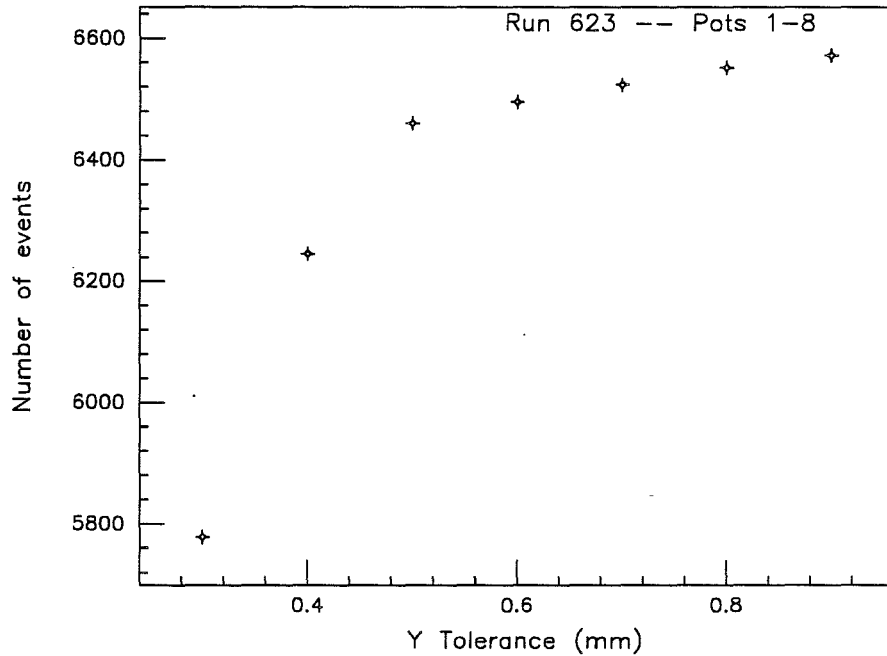


Figure 11: Stability of statistics with track tolerance

4.2.1 Calibration of the y Readout System

The purpose of the circular indentations, as well as the horizontal indentation at the bottom, of the calibration counter (Fig. 7) was to aid in the calibration of the readout system. This was done by observing a sample of events that did *not* register a hit on the calibration counter, but did register a hit on a trigger counter behind it. These are the events that went through the holes as well as the horizontal indentation at the bottom of the calibration counter. Their projection along the y axis is that of four normal distributions (corresponding to the four horizontal rows of circular holes) and one step function (corresponding to the bottom edge) (Fig. 12). The objective here was to calibrate the y readout system by fitting suitable functions to this distribution where the

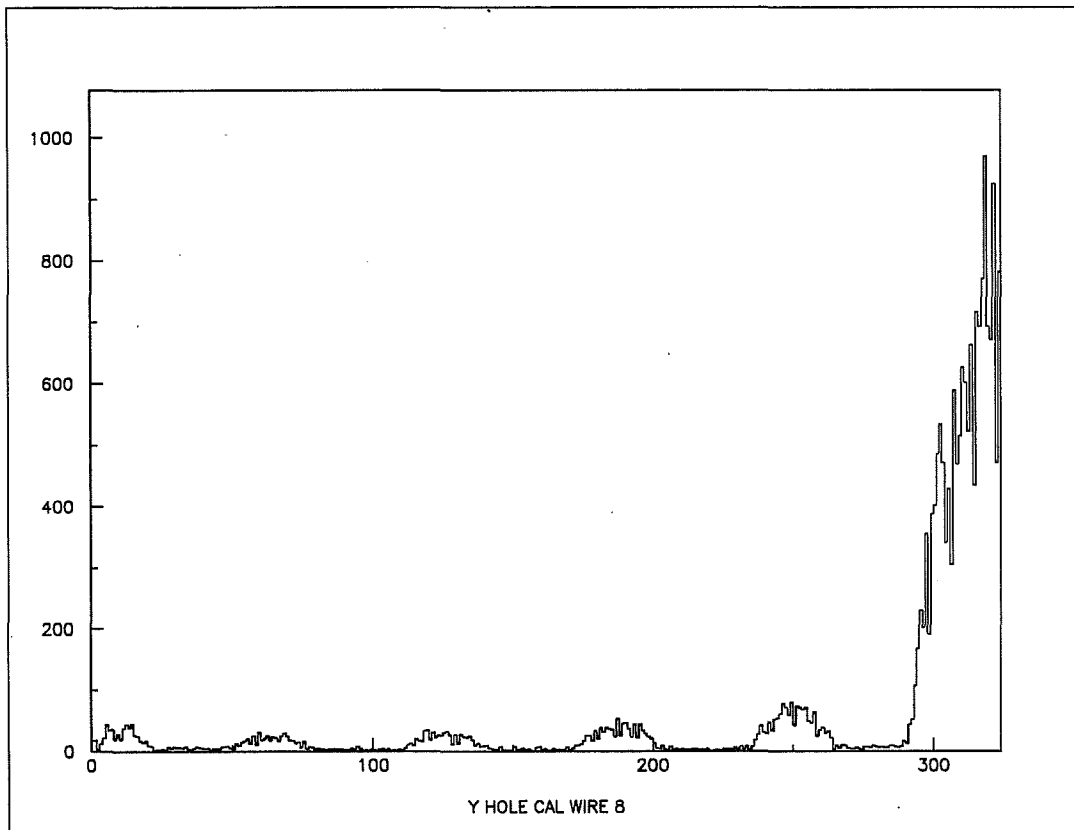


Figure 12: The y projection of the events penetrating through the indentations of the calibration counter

fitted parameters would include the calibration parameters of interest. To do this, an appropriate symmetric function had to be fitted to each of the four normal distributions. The problem was that the amount of statistics across the width of a given hole dropped by as much as 50% due to increasing distance from the beam, hence skewing the distribution and making the fit of a symmetric function impossible. Fig. 13 shows the distribution of *all* events as a function of y which clearly demonstrates this drop in statistics. It was therefore imperative to correct these distributions for their fall-off. This correction was accomplished by normalizing the distribution of Fig. 12 with

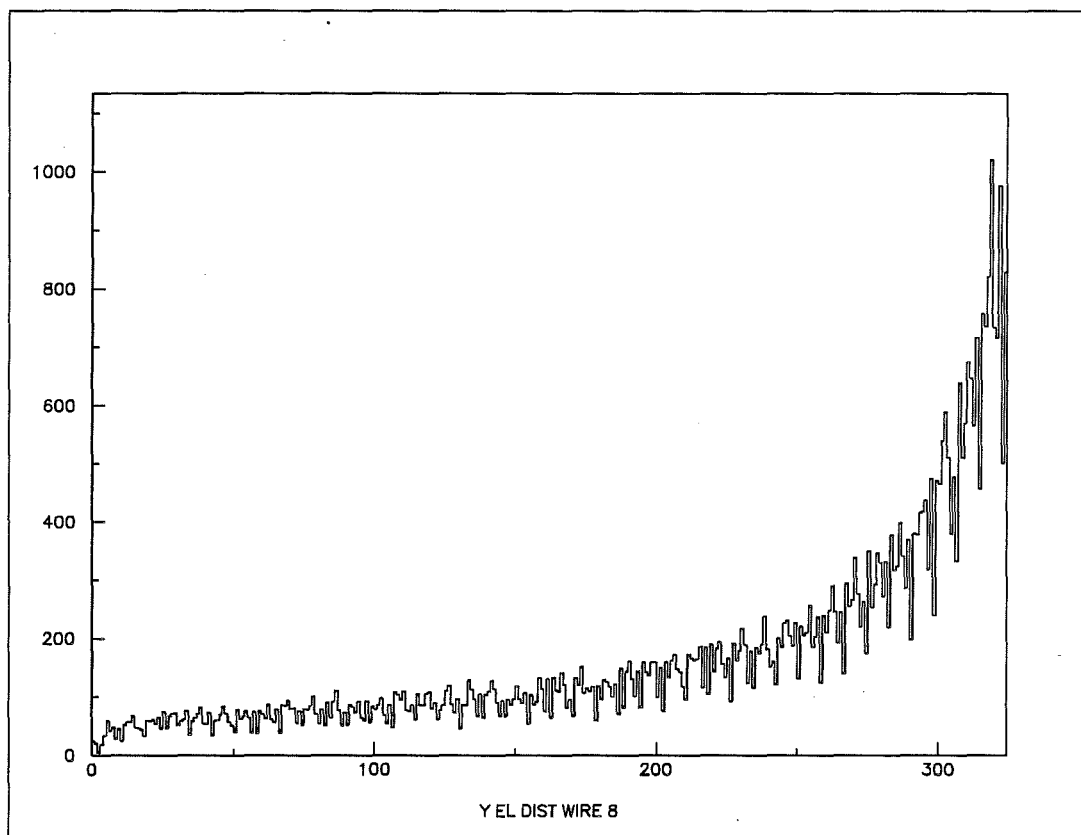


Figure 13: The y projection of all events regardless of which counter is hit

respect to the amount of raw statistics, i.e., the distribution of Fig. 13. This required dividing the contents of the former, bin by bin, by those of the latter. This bin by bin division served to diffuse the skewing effect due to reduction of statistics with increasing distance from the beam. The profile of this normalized distribution is clearly that of a step function and four normal curves of comparable sizes (Fig. 14). Each of these five sub-distributions are then isolated by the imposition around them of fiducial cuts the boundaries of which were selected by inspection.

The finite resolution of the detector system resulted in a smearing of these distributions. The form of this smearing is approximated as a gaussian convoluted with the expected profiles of the

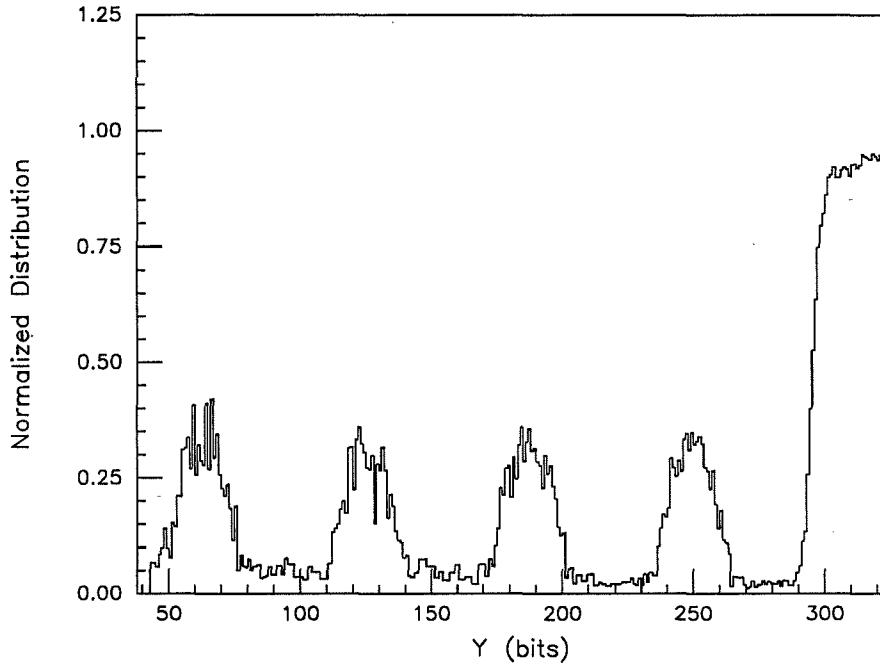


Figure 14: The corrected y projection of events penetrating the calibration counter

edge and the holes if the detector had infinite resolution. The width of this gaussian is a measure of the detector resolution.

For the edge of the counter, the convolution of the expected step function with a gaussian results in an error function. The form of this function is derived in Appendix E and can be expressed as

$$E(y) = \frac{N_e}{2} \left[1 + \operatorname{erf} \left(\frac{(y-p)c}{\sqrt{2}\sigma} \right) \right], \quad (16)$$

where

y is the electronic bit number identifying the vertical coordinate of the particle incident on the detector,

$E(y)$ is the normalized distribution of data at a given bit y ,

N_e is the normalization constant of the function,

p is the bit number corresponding to the edge of the calibration counter ,

σ is the width, in mm, of the gaussian representing the resolution of the detector,

c is the physical dimension corresponding to each bit (commonly referred to as the mm/bit constant),

Θ is a step function.

The profile of the holes are approximated as the convolution of a radial function with a gaussian (see Appendix E). For a given hole, this convolution can be expressed as:

$$I(y) = \frac{N_h}{\sqrt{2\pi}\sigma} \int_{-r}^r dY' e^{-\frac{1}{2\sigma^2}[(y-p)c-\mu-Y']^2} \sqrt{1 - \left(\frac{Y'}{r}\right)^2}, \quad (17)$$

where

$I(y)$ is the normalized distribution of data at a given bit y ,

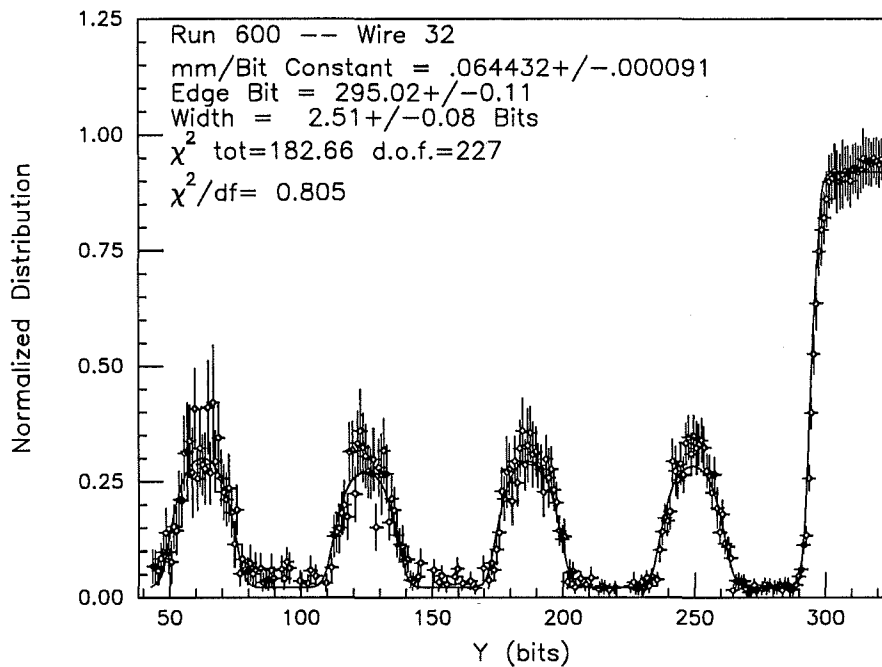
N_h is the normalization constant of the function,

r is the radius of the hole ($r=0.09$ mm),

μ is the location of the hole, in mm, with respect to the edge of the calibration counter.

For each sense wire in a drift chamber, a profile of the particles penetrating the holes and the bottom slit, similar to the one in Fig. 14, was obtained. Eq. 16 was fitted to the data at the edge of the calibration counter. Simultaneously, four functions of the form of Eq. 17 were each fitted to the profile of the holes. The fitted parameters were the five normalization constants, the edge bit p , the mm/bit constant c , and the resolution σ . For all wires, there was also a flat background due to the inclusion of the vertical strips at the left and right edges of the trigger counter which were

19-NOV-92 16:29:32

Figure 15: The y calibration fit

not covered by the calibration counter (See Fig. 7). An extra parameter added to the functions of Eqs. 16 and 17 was fitted to account for this flat noise.

Fig. 15 is the superposition of this fit on the data of Fig. 14. Of all of the fitted parameters, two were of primary interest, namely the mm/bit constant c and the bit number of the edge of the calibration counter p . Knowledge of these two parameters is crucial for determining the precise location of the scattered particle and hence its scattering angle.

4.2.2 Calibration of the x Readout System

The sample of events used here was formed in precisely the same manner as with the y calibration, except that here they were integrated along the y axis, i.e., the projection along the x axis was

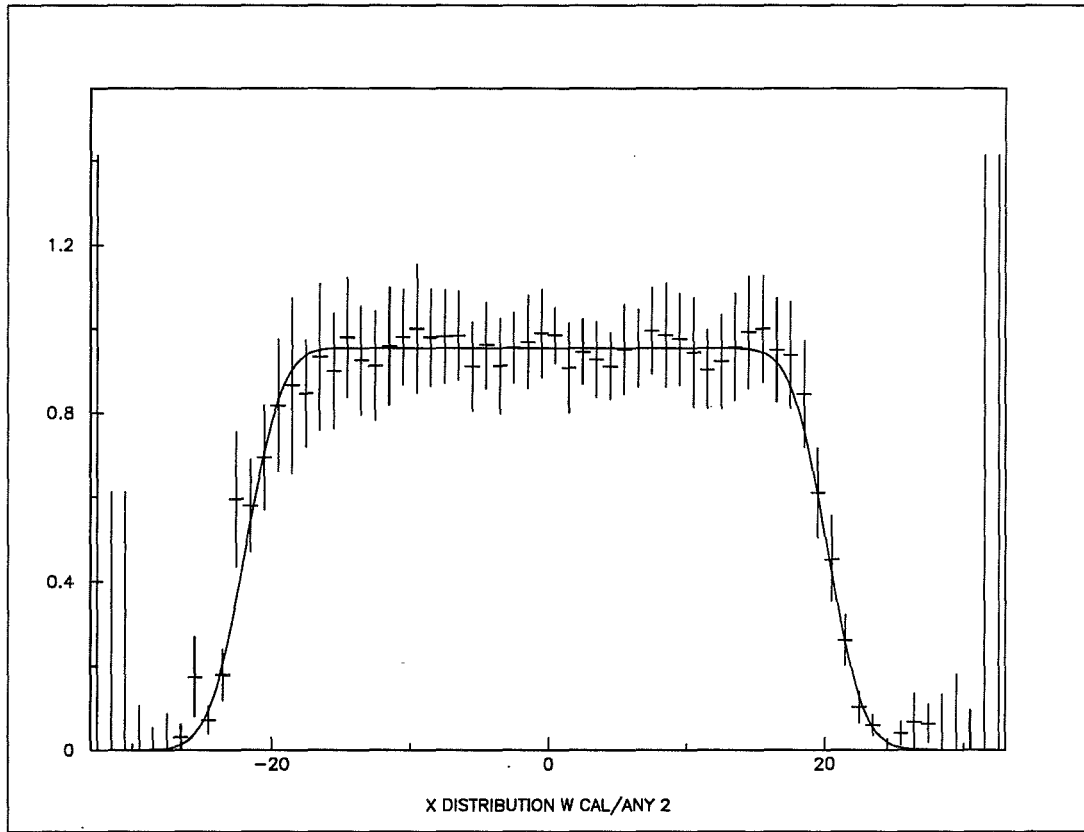


Figure 16: The calibration function superimposed on the normalized x distribution

formed. The abscissa consisted of the 64 electronic bits of the x readout system. As in the y readout case, two distributions were obtained. One corresponded to the events that registered a hit on *both* the trigger and calibration counters, and another to the events that registered a hit on the trigger counter regardless of their hit status on the calibration counter. Again, the former distribution was divided, bin by bin, by the latter. The shape of the normalized distribution was flat in the central 20 mm where the trigger counter was covered by the calibration counter, and rapidly dropped to zero in the outer 4 mm wide regions which were not covered by the calibration counter (refer back to Fig. 7 for counter geometries).

Two error functions of the same width w were simultaneously fitted to the two vertical edges. If the bit numbers corresponding to the left and right edges are labeled as E_1 and E_2 , respectively, then the functions $E_l(x)$ and $E_r(x)$ fitted to the left and right edges were:

$$E_l(x) = N \operatorname{erf} \left(\frac{x - E_1}{w\sqrt{2}} \right), \quad (18)$$

$$E_r(x) = N \operatorname{erf} \left(\frac{E_2 - x}{w\sqrt{2}} \right). \quad (19)$$

Here, N is the normalization constant which is fitted along with E_1 , E_2 , and w . Fig. 16 is the superposition of the fitted edge functions on the normalized distribution. The quantity $|E_1 - E_2|$ is the distance, in bits, between the vertical edges. Dividing this quantity by the known distance of 20 mm yielded the mm/bit constant of the x calibration.

Due to the unexpected nonlinearity of the x readout system, the x information was not used in the analysis.

4.3 Determination of the Scattering Angles

The calibration of the y readout system allowed one to determine the location of a scattered particle relative to the detector itself. If the electronic bit corresponding to the y coordinate of the scattered particle is designated as y_b , following the nomenclature of Section 4.2.1, the y component of the location of the particle with respect to the interaction point can be calculated according to

$$Y = (p - y_b)c + Y_{eb} + Y_{pot}, \quad (20)$$

where Y_{eb} is the distance between the upper vertical edge of the calibration counter and the bottom of the chamber ($Y_{eb} \approx 2$ mm as shown in Fig. 7), and Y_{pot} is the known distance of the chamber from the center of the detector system.

The latter quantity Y_{pot} was determined in the following manner: Before the start of every run, the pots were moved vertically toward the beam until a sudden increase in the counting rate was

detected by the trigger counters. This position was recorded and referred to as the touch position. The halfway point between the touch positions of the upper and lower detectors in a castle is the center of the detector system. To determine the scattering angle, it was necessary to find the position of this detector center with respect to the interaction region.

The position of the center of the detector system relative to the beam center is referred to as the beam offset, and is identified as y_0 in the equations of motion in Section 2.2. To find y_0 , the coordinates of the elastically scattered particles on the two sides of E0 were compared. As mentioned in Section 3, the quadrupole magnets placed in the accelerator ring between the outer drift chambers and E0 forced the measurement of scattering angles to register values other than what they would have been had the magnets not altered their trajectories. Thus, the *effective* lengths and not the actual lengths between the detectors and the interaction region on each side of E0 had to be taken into account. A new *scaled* reference frame was devised. The quantity L is the average of these four effective lengths (L_x , L_y , $L_{x'}$, and $L_{y'}$ in the equations of motion).

The coordinates (X, Y) and (X', Y') are designated as the *scaled* reference frame coordinates of an elastic track on the left and right sides, respectively. They are defined as

$$L \equiv \frac{1}{4}(L_x + L_y + L_{x'} + L_{y'}), \quad (21)$$

$$X \equiv \frac{L}{L_x}x, \quad (22)$$

$$Y \equiv \frac{L}{L_y}y, \quad (23)$$

$$X' \equiv \frac{L}{L_{x'}}x', \quad (24)$$

$$Y' \equiv \frac{L}{L_{y'}}y'. \quad (25)$$

Rescaling the equations of motion and averaging them, we obtain

$$\langle X \rangle = b_x x_0 + L(\alpha_x + \phi_x), \quad (26)$$

$$\langle X' \rangle = -b_{x'} x_0 + L(\alpha_x + \phi_{x'}), \quad (27)$$

$$\langle Y \rangle = b_y y_0 + L(\alpha_y + \phi_y), \quad (28)$$

$$\langle Y' \rangle = b_{y'} y_0 - L(\alpha_y + \phi_{y'}), \quad (29)$$

where the interaction distribution width, the betatron oscillation distribution width, and the detector resolution terms are dropped since they are presumed to average out to zero. The ϕ terms are possible beam tilts. The b terms are defined according to $b_x \equiv \frac{L}{L_x} m_x$, $b_y \equiv \frac{L}{L_y} m_y$, etc.

Again, since the only coordinate of interest is y , the x equations will no longer be used. Adding the y equations yields

$$y_0 = \frac{\langle Y + Y' \rangle}{b_y + b_{y'}}, \quad (30)$$

where $\phi_y - \phi_{y'}$ is absorbed into the measurement of y_0 . Also, since Y is independent of Y' , the average of their sum is taken to be the sum of their averages. The amounts by which the coordinates of the left and right side events should be shifted is then

$$Y_{shift} = b_y y_0, \quad (31)$$

$$Y'_{shift} = b_{y'} y_0. \quad (32)$$

This uniform shifting of the event coordinates will leave the pattern centered about the beam.

Once the scaled coordinates (X, Y) of the scattered particle *on the left side* of E0 is thus determined, its scattering angle θ is found by using the small angle approximation

$$\theta_x = \frac{X}{L}, \quad (33)$$

$$\theta_y = \frac{Y}{L}, \quad (34)$$

$$\theta = \sqrt{\theta_x^2 + \theta_y^2}. \quad (35)$$

4.4 Widths of the Elastic Pattern

In the elastic sample, the differences of the detected coordinates of the two elastically scattered particles, i.e., $|Y| - |Y'|$ and $|X| - |X'|$, were two-dimensional distributions with finite widths.

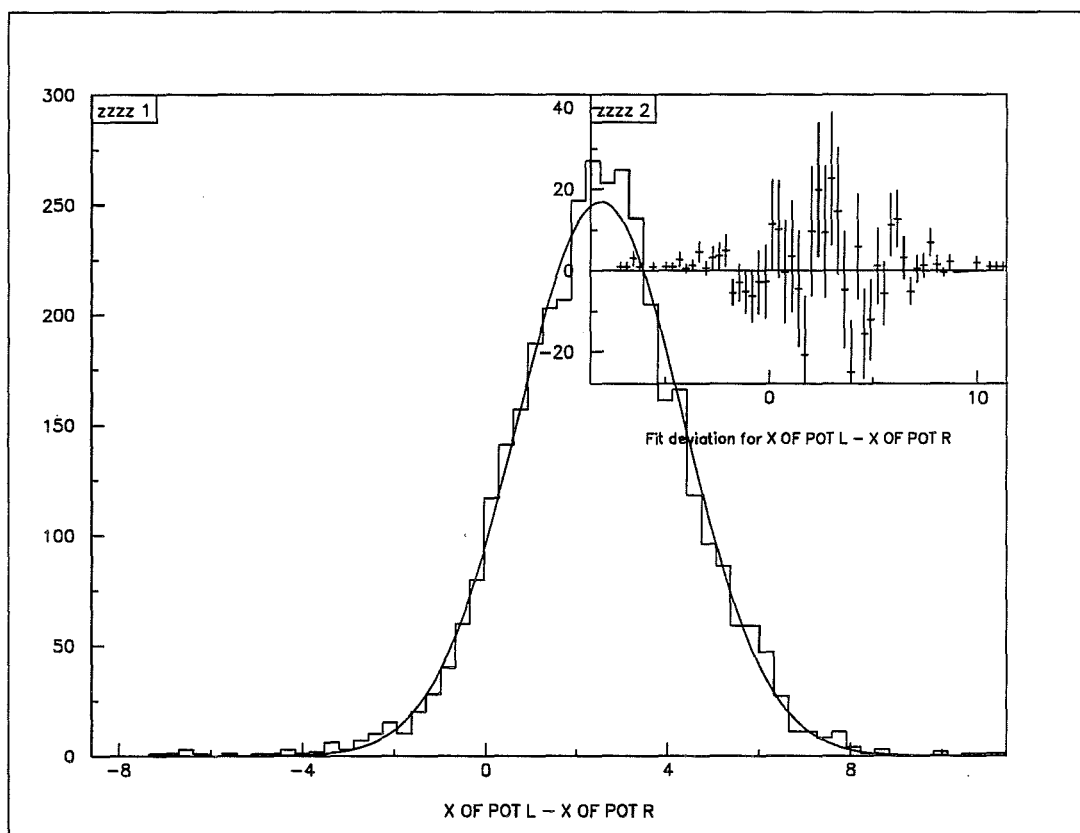


Figure 17: Gaussian fit to the x elastic pattern

These widths were due to the non-zero width of the interaction region, the betatron oscillations, and the detector resolutions. The projections of these distributions on the xz and yz planes are gaussians. The widths of these gaussians are referred to as the x and y pattern widths, respectively, and are designated the symbols σ_x and σ_y . Figs. 17 and 18 show the gaussian x and y patterns with fitted gaussian functions superimposed on them.

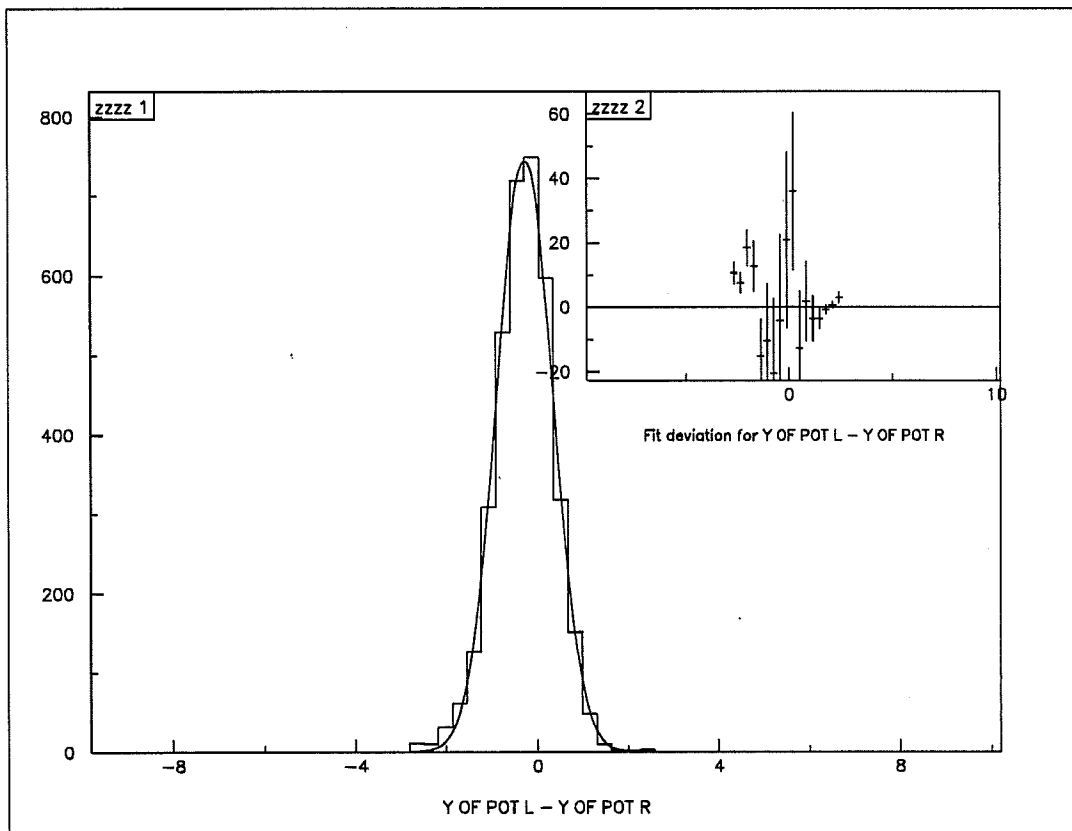


Figure 18: Gaussian fit to the y elastic pattern

4.5 Binning of the Data

As mentioned in Section 4.1.2, the event selection procedure resulted in two different sets of event samples. One set corresponded to events that registered a coincidence between chambers located diagonally about E0 (1-8 or 2-7), and another between chambers on the same side of the beam (1-7 or 2-8). The former was referred to as the elastic sample, and the latter as the background sample.

The x readout system displayed nonlinearities that made it unsuitable for accurate measurement. Consequently, only the y information was used in the analysis, and for each differential y

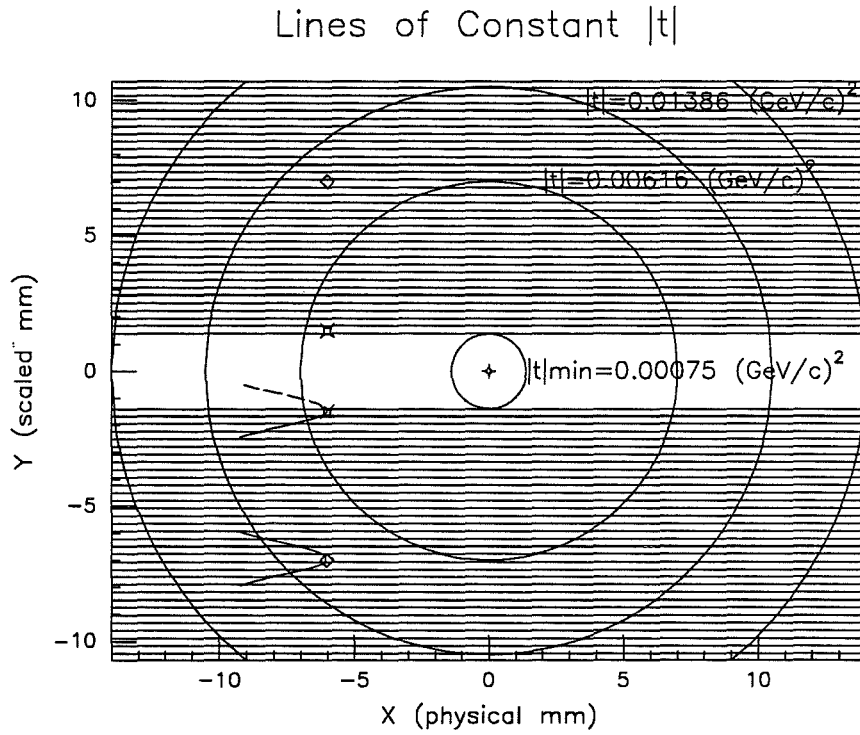


Figure 19: Contours of constant $|t|$ at c.m. energy of 1.8 TeV

strip, the data were integrated over the complete 28 mm x range.

The data in both sets of samples were binned along the y direction in a number of bins, referred to as stacks, for each of the chambers. The width of each stack was chosen as 0.5 mm, approximately equal to the pattern width in y , for the $\sqrt{s}=1.8$ TeV data. This resulted in 40 stacks in order to cover the height of a chamber. For the $\sqrt{s}=1.0$ TeV data, the y pattern width was about 1 mm. Consequently, 20 stacks, each 1 mm wide, were used for this energy. Fig. 19 is a schematic of the stacks, where the t designations correspond to $\sqrt{s}=1.8$ TeV. Fig. 20 is a similar schematic for $\sqrt{s}=1.0$ TeV. The point at the center of either figure represents the beam line which is perpendicular to the plane of the figure. The grids on the top and bottom correspond to the

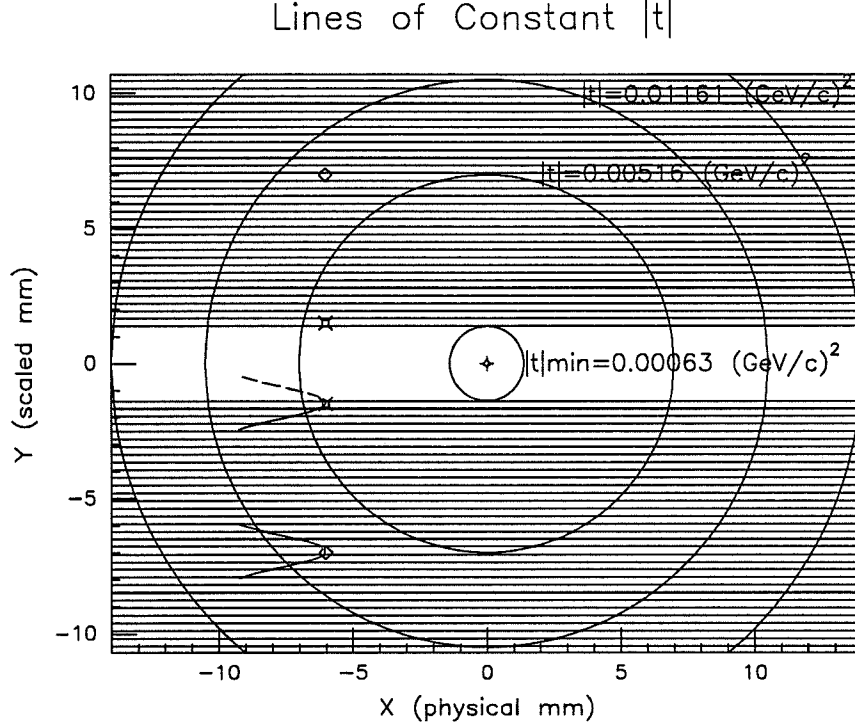


Figure 20: Contours of constant $|t|$ at c.m. energy of 1.0 TeV

stack matrices of the left and right side detectors, respectively. Each stack contained all of the events that registered a coincidence between the y range of that stack and the *entire* detector on the other side of the interaction region. The stacks were numbered so that, for each chamber, stack 1 was closest to the beam. Therefore, stack 1 was the bin covering the lowest $|t|$ values, and stack 40 (20) the bin covering the highest. The circles in the figures are constant $|t|$ loci, the smallest of which corresponded to $|t|_{min}$. It is readily seen that each stack covers a large range of $|t|$ values in the x direction.

The chosen $|t|_{min}$ was that of the largest of the four outer chambers. Each stack of any chamber covered exactly the same solid angle as the corresponding stack of any other chamber. For the

1.8 TeV data, where the relative background amount was about the same for the two elastic chamber combinations (1–8 and 2–7), this equivalency of solid angles allowed the *averaging* of the contents of each of the two corresponding stacks for the two vertically aligned pots 1 and 2. If after the centering there were still a non-zero, *albeit* small, offset between the detector center and the beam, the second largest (after the 0th order) term in a Taylor expansion of the differential cross section about the centered position, with this offset as the expansion parameter, would be the 1st order term. This term would have the same magnitude but opposite signs for the two vertically aligned pots in the same castle. The advantage of this stack by stack averaging would then be the cancellation of the 1st order term. This averaging was not warranted with the 1.0 TeV data due to the large discrepancy in the relative background contents of two combinations. This point will be elaborated on in Section 5.

4.6 Background Subtraction

On the right side detector, the events which registered a coincidence with a high $|t|$ stack on the left side detector, as indicated by the diamonds in Figs. 19 and 20, formed a pattern in the shape of a two-dimensional gaussian which peaked at the same stack number as the left side stack with which they were coincident. There was also a significant amount of background due to beam halo which was concentrated in the lower stacks of the right side chamber. This background was separable from the signal *only* for events coincident between the *high* $|t|$ stacks of one detector and all stacks of the detector on the other side of E0. In such cases, one could clearly identify two peaks in the pattern formed on the latter detector: a high $|t|$ peak corresponding to the elastic signal, and a low $|t|$ peak corresponding to the background. There was a strip of empty stacks between these two peaks which made the isolation of signal from noise straightforward. Fig. 21 demonstrates the two peaks, as well as the separation between them, for a typical case. For events coincident with

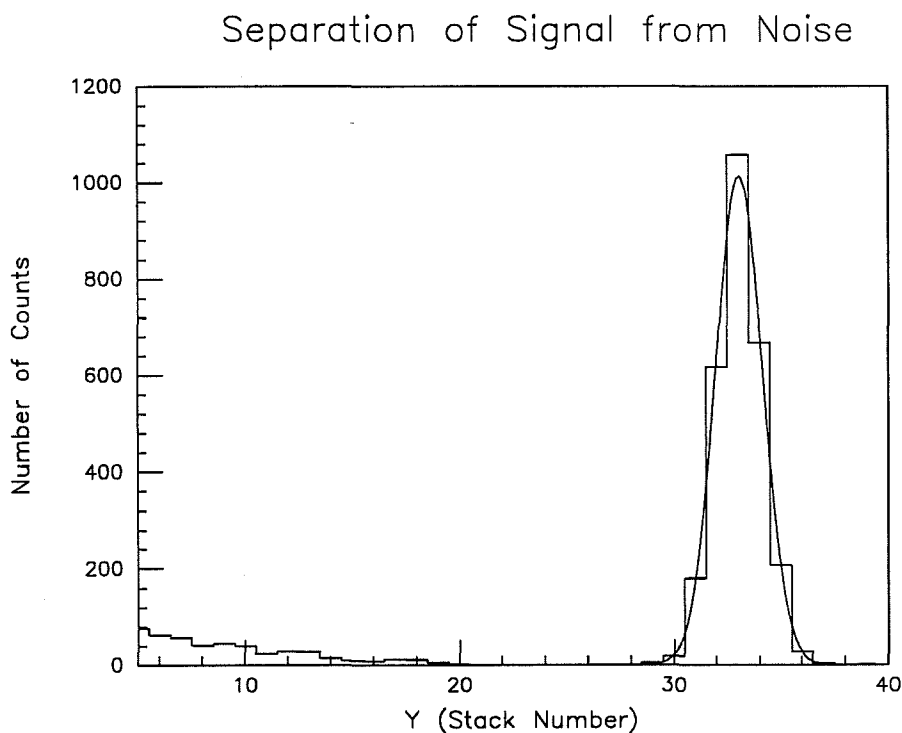


Figure 21: The separation between the background and the signal peaks

a *low* $|t|$ stack on the left side, the right side pattern was *not* that of clearly discernible signal and background peaks. Since all of the Coulomb and interference information resided in the low $|t|$ stacks, a method had to be devised to separate the background noise from the elastic signal in this region. To do this, the magnitude and shape of the background was derived from the background peak that was separable from the elastic signal at high $|t|$ stacks.

A comparison was made between the shapes of the distributions corresponding to (a) events in the elastic sample coincident between the high $|t|$ region of the left side detector and the low $|t|$ region of the right side detector, i.e., the background subset of the elastic sample which, as mentioned, was separable from the elastic signal, and (b) events in the background sample coincident between the *same* high $|t|$ region of the left side detector and *all* of the right side detector. These

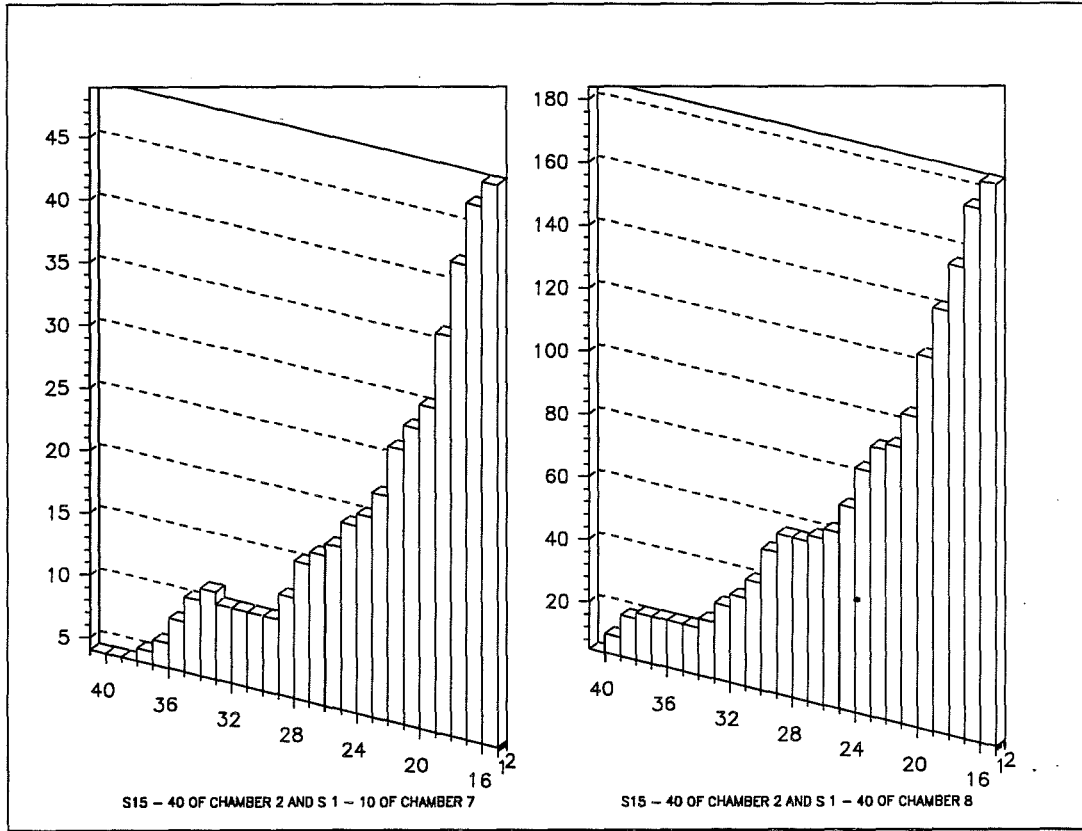


Figure 22: Comparison of background shapes from elastic and background samples

two shapes were shown to be the same. Fig. 22 is a comparison of these two distributions.

The background content B_i^I of a stack i belonging to a left side chamber I can be expressed in the following way

$$B_i^I = \sum_{j=1}^{j_{cutoff}} N_{ij}^{IJ}, \quad (36)$$

where

N_{ij}^{IJ} is the number of events coincident between stack i of chamber I and stack j of chamber J .

j_{cutoff} is the upper cutoff stack of the region containing the background and is

found by inspection, such as in Fig. 21,

In Eq. 36, chamber J is the elastic partner of chamber I , i.e., the two chambers are located diagonally about E0, and therefore N_{ij}^{IJ} belongs to the elastic sample.

The similarity of background shapes from the two samples, as shown in Fig. 22, indicated that B_i^I can alternatively be *calculated* according to

$$B_i^I = C_i P_i^I, \quad (37)$$

where C_i is an empirically determined proportionality constant. The normalized background content P_i^I of stack i of chamber I is determined according to

$$P_i^I = \frac{\sum_{k=1}^{max} N_{ik}^{IK}}{N_{tot}^{IK}}. \quad (38)$$

This normalization is specified by the right side of Eq. 38. The numerator is the pre-normalized background content, i.e., the number of events coincident between stack i of chamber I and *all* of chamber K which is located at the same side of the beam as I . It is clear that N_{ik}^{IK} is obtained from the background sample. The denominator, N_{tot}^{IK} , is the total number of events coincident between chambers I and K . It is with respect to the latter quantity that the background content is normalized.

Equating Eqs. 36 and 37, one can solve for C_i

$$C_i = \frac{\sum_{j=1}^{j_{cutoff}} N_{ij}^{IJ}}{P_i^I}. \quad (39)$$

Here, i is a high $|t|$ stack. The constant C_i is calculated for all high $|t|$ stacks on chamber I where typically $i \geq j_{cutoff} + 4$. The 4 stack, and hence 4σ , separation between the lowest i and j_{cutoff} was to prevent inclusion of any elastic events in the N_{ij}^{IJ} sample. Inversely, the same was done for the low $|t|$ stacks on chamber I and high $|t|$ stacks on chamber J , yielding a series of C_j values.

All of these C_i and C_j values were equal within errors, and were therefore averaged together. This average, C^{IJ} , was the background normalization constant for the elastic chamber combination $I-J$, where $I-J$ was either 1-8 or 2-7. The background content of cell i was then calculated according to Eq. 37.

We can see here that although the background normalization constant was determined by using information from high $|t|$ regions only, it allowed the calculation of background in *all* $|t|$ regions, particularly in the low $|t|$ stacks where all Coulomb and interference data reside.

Calculating the background content for each stack also provided the signal to noise ratio for that stack. For a typical subset of the 1.8 TeV data, these ratios for the bottom 10 stacks are tabulated below:

Stack	Signal + Noise	Noise	Signal	Signal/Noise
1	720.	$388. \pm 15.$	$332. \pm 31.$	0.85
2	746.	$299. \pm 12.$	$447. \pm 30.$	1.50
3	656.	$227. \pm 10.$	$429. \pm 27.$	1.89
4	600.	$181. \pm 8.$	$419. \pm 26.$	2.31
5	619.	$151. \pm 7.$	$468. \pm 26.$	3.11
6	548.	$127. \pm 7.$	$421. \pm 24.$	3.31
7	523.	$109. \pm 6.$	$414. \pm 24.$	3.80
8	506.	$92. \pm 5.$	$414. \pm 23.$	4.48
9	493.	$82. \pm 5.$	$411. \pm 23.$	5.02
10	488.	$74. \pm 5.$	$414. \pm 23.$	5.63

4.7 Normalization of the Data

The data were normalized simultaneously by the number of inelastics and the accelerator luminosity.

4.7.1 The Inelastics

The luminosity-free method was discussed in Section 2.1. The number of inelastics, N_{inel} , was counted by the ring scintillation counters (refer back to Fig. 3). Also in Section D.1.2, the L, R, and LR triggers are defined. These triggers were the primary sources of information about the number of inelastic events. Several corrections were made to these numbers due to differences in bunch intensity and incomplete angular coverage. These corrections were estimated to be [41]

$$\frac{\text{single arm L} + \text{single arm R}}{\text{LR}} = 0.354 \pm 0.075, \quad (40)$$

$$\frac{\text{extrapolated L Loss} + \text{extrapolated R Loss}}{\text{LR}} = 0.028 \pm 0.014 \text{ (small angle)}, \quad (41)$$

$$\frac{\text{extrapolated L Loss} + \text{extrapolated R Loss}}{\text{LR}} = 0.016 \pm 0.008 \text{ (large angle)}. \quad (42)$$

Using these corrections, the number of inelastics was calculated and used to normalize the data at $\sqrt{s} = 1.8$ TeV *only*. The error of the inelastics is composed of two parts. One part is simply the square root of the number of LR counts. The other part is due to the errors of the corrections identified above.

4.7.2 The Accelerator Luminosity

In addition to the inelastics, the accelerator luminosity was used to normalize the measured counting rate.

Two of the scaler constants that were recorded at the end of each run were the monitor constants M and M' . M was the electronics logic coincidence of all the counters in the R5 quadrant (in a 6 ns coincidence) put into a 15 ns electronics logic coincidence with that of all the counters in the L5

quadrant, all latched to a 30 ns coincidence with the RF signal (refer to Section D.1). Scaler M' was the same as M , but with the RF signal delayed by 21 μs in its coincidence with the L5×R5 logic pulse.

Two other scaler constants were *clock* and *g(ated)clock*. The ratio of the latter to the former was the fraction of the time the experiment was not cut off by the signal indicating beam in the Main Ring above the Tevatron.

The integrated accelerator luminosity for a given run was calculated by the relation

$$\mathcal{L} = K(M - M') \frac{\text{clock}}{g\text{clock}}, \quad (43)$$

where K is the fitted slope of a straight line to the integrated luminosities vs $M - M'$ values for a series of dedicated runs whose luminosities were recorded at the intersection region B0 along the Tevatron. The value of K was known to an accuracy of about 15%.

4.8 Subdivisions within the Data

For the 1.8 TeV data, four series of runs, corresponding to four stores, were analyzed. Within each series, the runs were first individually analyzed to check for internal consistency. They were then combined at the outset to form what was referred to as a superrun, the run composed of the entire usable data for that series. The integrated luminosity of a superrun was simply the sum of the luminosities of its constituent runs. The four series were labeled as the 600 series (runs 623 to 626), the 650 series (runs 627 to 630), the 700 series (runs 754, 755, 757, and 758) and 750 which was the only usable run from its store.

The 1.02 TeV data were taken from only one store. The runs used were 788 to 793.

4.9 Fitting the Data

Eq. 113 is the expression for the differential elastic cross section. The data, however, do *not* obey the form of this relation since each datum point is not the number of counts at a t value. Rather, each $28 \text{ mm} \times 0.5$ (or 1) mm stack covers a large range of t values, as seen in Figs. 19 and 20. Furthermore, as elaborated on in Section 4.4, the elastic pattern had a finite width due to beam thickness, betatron oscillations, and detector resolution. In the vicinity of the beam, near the horizontal edges of the right side detector, a portion of the elastic pattern was lost, and therefore not all of the possible events near the detector edges were recorded. In Figs. 19 and 20, the half-dashed gaussian represents the elastic pattern coincident with the low $|t|$ stacks of the left side detector. The dashed part is the portion of the pattern that lies outside of the detector boundaries. This problem did not exist for the vertical edges of the chamber, since in scaled space the right side chambers are wide enough to contain the entire x component of the elastic pattern. The theoretical function describing the data at a given t value was not simply the differential elastic cross section, but a new function which takes these limitations into account. This function was the convolution of the differential elastic cross section, $\frac{d\sigma_{el}}{dt}$, with a two-dimensional gaussian, where the limits of integration were the boundaries of the right side detector.

The t value of each detected particle is calculated using Eq. 94, i.e., $t = -p^2\theta^2$, where θ is the particle's scattering angle. The latter can be expressed in terms of its polar and azimuthal components, θ_x and θ_y

$$\theta^2 = \theta_x^2 + \theta_y^2, \quad (44)$$

where

$$\theta_x = \frac{X + X'}{2L}, \quad (45)$$

$$\theta_y = \frac{Y + Y'}{2L}. \quad (46)$$

Here, the lowercase coordinates are in physical mm and the uppercase coordinates are in scaled mm, where this scaling is defined in page 42. The unprimed coordinates are those of the events as measured by the left side detectors, and the primed coordinates those of the events measured by the right side detectors. The quantity L is the average of the x and y effective lengths of the two sides.

The theoretical function describing the data contained in stack i is derived in Appendix F. Its final form is

$$\left\langle \frac{d\sigma_{el}}{dt} \right\rangle_i = \frac{1}{\Delta x \Delta y} \int_{-\frac{\Delta x}{2}}^{\frac{\Delta x}{2}} \int_{y_{min_i}}^{y_{min_i} + \Delta y} dy dx \left[\int_{-\infty}^{\infty} \int_{y'_{min}}^{y'_{max}} \frac{d\sigma_{el}}{dt} \frac{e^{-\frac{1}{2}(\frac{x-x'}{\sigma_x})^2}}{\sqrt{2\pi}\sigma_x} \frac{e^{-\frac{1}{2}(\frac{y-y'}{\sigma_y})^2}}{\sqrt{2\pi}\sigma_y} dy' dx' \right]. \quad (47)$$

The bracketed portion of the integrand is the theoretical function describing the data at a given t value. The form of this function is due to the finite width of the elastic pattern. The quantities σ_x and σ_y are the x and y pattern widths, respectively. The limits of integration in y' correspond to the boundaries of the right side chamber. The integration limits in x' are approximated as infinities due to the sufficiently large width of the right side detector.

As mentioned before, the data points are integrated counts over the area of each stack. Therefore, the function bracketed in the above expression was averaged over the dimensions of stack i . The width and thickness of each stack are labeled as Δx ($=28$ mm) and Δy ($=0.5$ mm at $\sqrt{s}=1.8$ TeV and 1 mm at 1.02 TeV), respectively. The quantity y_{min_i} is the y coordinate, measured with respect to the beam, of the lowest $|t|$ point of stack i .

The integrals in Eq. 47 were evaluated numerically using gaussian quadratures[42]. Appendix F describes the methodology used in deriving and evaluating these integrals.

The measured quantity for stack i was the number of counts contained in that stack, ΔN_i . The incremental t range covered by that stack, Δt , is expressed as

$$\Delta t = \frac{p^2}{\pi} \Delta \Omega, \quad (48)$$

where $\Delta\Omega$ is the solid angle subtended by each stack and is equal to $\frac{\Delta y}{L_y} \times \frac{\Delta x}{L_x}$. The differential count $\frac{\Delta N_i}{\Delta t}$ can be expressed in terms of $\left\langle \frac{d\sigma_{el}}{dt} \right\rangle_i$ according to

$$\frac{\Delta N_i}{\Delta t} = \mathcal{L} \left\langle \frac{d\sigma_{el}}{dt} \right\rangle_i. \quad (49)$$

The luminosity term \mathcal{L} is fitted in addition to σ_t , B , and ρ . Both the accelerator luminosity provided by the accelerator group at Fermilab *and* the number of inelastics are used to normalize the fit.

The χ^2 to be minimized by the fit contained three classes of terms. For a stack i , one class utilized Eq. 49, fitting \mathcal{L} as well as σ_t , B , and ρ . The next class of terms employed the relation

$$N_{inel} = \mathcal{L}\sigma_{inel}. \quad (50)$$

In the fit, the inelastic cross section σ_{inel} was expressed as $\sigma_t - \sigma_{el}$, where the latter was a quantity in terms of the elastic scattering parameters (see Eq. 6). The last χ^2 term fitted \mathcal{L} with the empirical accelerator luminosity value which had an error of 15%.

5 Results

Two sets of data corresponding to center of mass energies of $\sqrt{s}=1.80$ and 1.02 TeV were analyzed using the procedure outlined in the analysis section (Section 4).

5.1 The 1.8 TeV Data

As explained in Section 4.8, four sets of superruns were individually analyzed. The results of these analyses are presented in Section 5.1.1. Once internal consistency among these superruns was established, they were fit simultaneously in a global fit the result of which is shown in Fig. 23. The downward curvature of the experimental points at low stacks is due to loss of statistics resulting

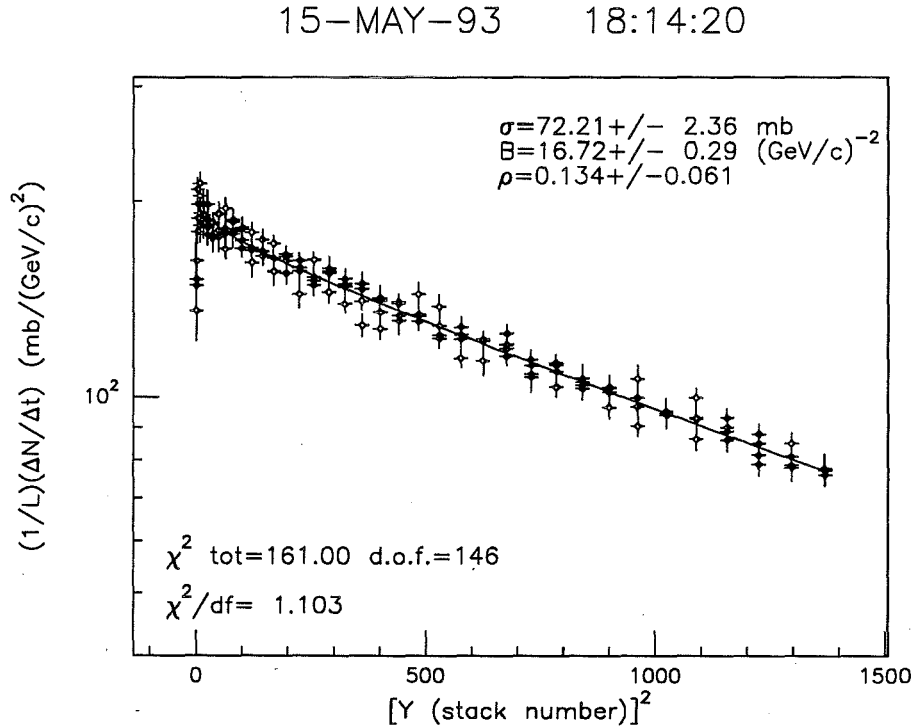


Figure 23: Fit to the 1.8 TeV data

Source	ρ	σ_t (mb)	B ((GeV/c) $^{-2}$)
Background normalization constant	0.0328	0.61	0.034
L_x	0.0004	0.18	0.001
L_y	0.0016	0.93	0.331
Pot position	0.0059	0.16	0.042
Calibration	0.0020	0.07	0.023
Pattern width	0.0001	0.01	0.001
Quadrature sum of systematic errors:	0.033	1.1	0.33
Statistical error:	0.061	2.4	0.29
Overall error:	0.069	2.7	0.44

Table 4: Systematic error contributions for 1.8 TeV data

from decreasing acceptance. These losses were modeled and factored into the calculation of the effective differential cross section as described in Appendix F. The designation along the abscissa is the *square* of Y since, in the nuclear region, the logarithm of the differential cross section varies linearly with $|t|$, which in turns is proportional to the square of the scattering angle. The data were normalized by the number of inelastics *and* the accelerator luminosity.

The errors are purely statistical. These errors were later enlarged due to systematic contributions to the overall uncertainty from a number of factors such as effective lengths, pot positions, pattern widths, readout calibrations and the background normalization constant. The breakdown of the contribution of each of these factors to the overall errors is shown in Table 4. The overall errors are the quadrature sum of the statistical and systematic uncertainties. This yields the final results for the 1.8 TeV data of

$$\sigma_t = 72.2 \pm 2.7 \text{ mb},$$

$$B = 16.72 \pm 0.44 \text{ (GeV/c)}^{-2},$$

$$\rho = 0.134 \pm 0.069,$$

$$\frac{\sigma_{el}}{\sigma_t} = 0.225 \pm 0.164,$$

where the ratio σ_{el}/σ_t was calculated using Eq. 6.

5.1.1 Results from Individual 1.8 TeV Superruns

The four superruns described in Section 4.8 were individually analyzed to check for internal consistency among the results. In addition to the $\Delta N/\Delta t$ values, the input data consisted of the number of inelastics N_{inel} and the accelerator luminosity \mathcal{L} . These values are presented in Table 5 for each of the four superruns. The rightmost column is the luminosity which resulted from the *global* fit

Superrun	N_{inel}	Accelerator Luminosity (mb^{-1})	Fitted Luminosity (mb^{-1})
600	300298	5376	5374 ± 437
650	291295	6049	5065 ± 412
750	134862	2679	2311 ± 188
700	268601	4743	4751 ± 386

Table 5: Normalization parameters of the 1.8 TeV superruns

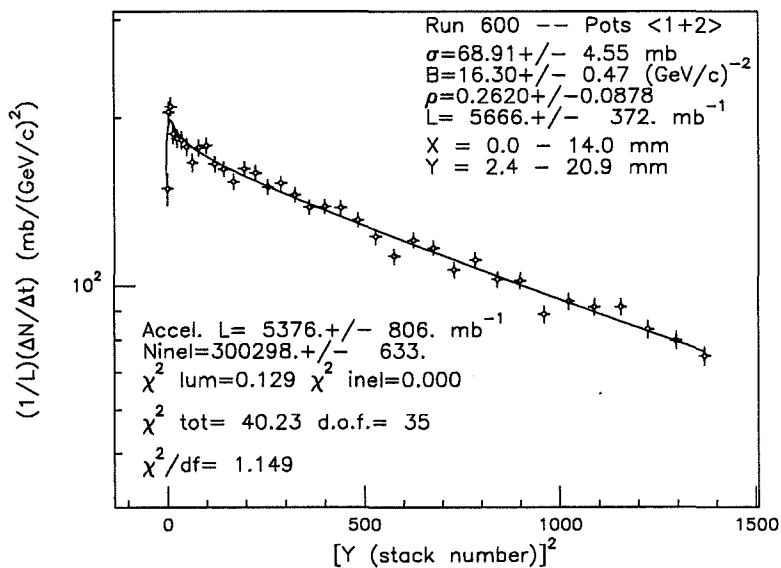
to the entire data. Plots of the fits are presented in Figs. 24 and 25.

5.1.2 Earlier E710 Elastic Scattering Results at 1.8 TeV

As mentioned in the introductory section, Section 1.4, E710 has analyzed the low $|t|$ 1.8 TeV data three times. The results emphasized in this work correspond to the third and final attempt.

The first attempt was in 1989, when no strategy for background subtraction was yet developed[24]. Analysis, therefore, was restricted to the relatively background-free region in the higher $|t|$ portion ($0.02 < |t| < 0.08 \text{ (GeV/c)}^2$) of the data. Consequently, no ρ value was measured; it was instead

14-MAY-93 20:56:45



14-MAY-93 21:17:22

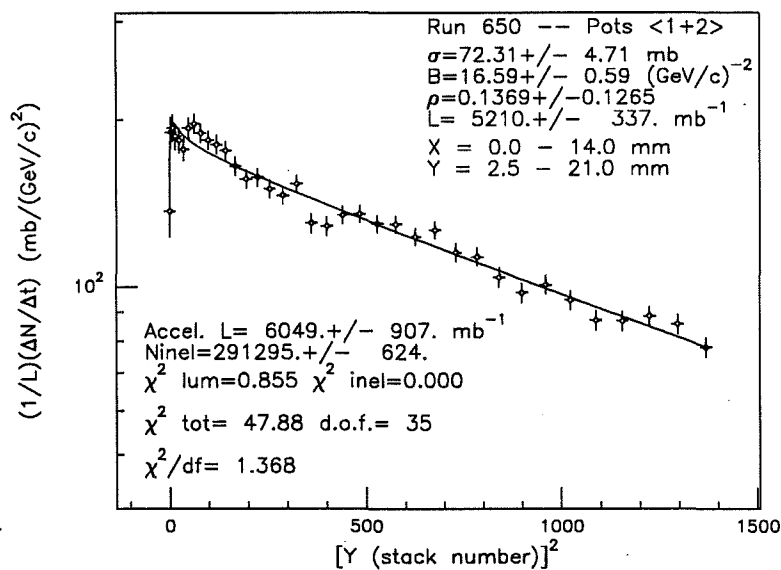
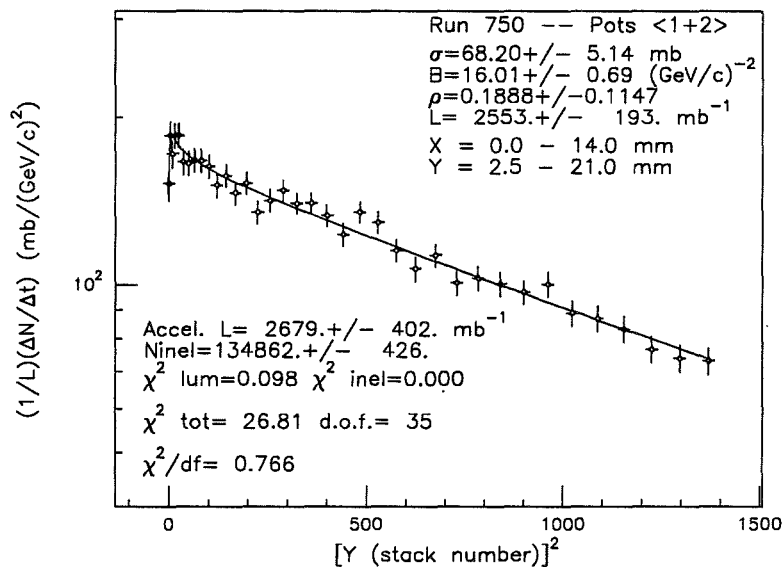


Figure 24: Fits to the 600 and 650 series of the 1.8 TeV data

14-MAY-93 22:15:36



14-MAY-93 22:12:25

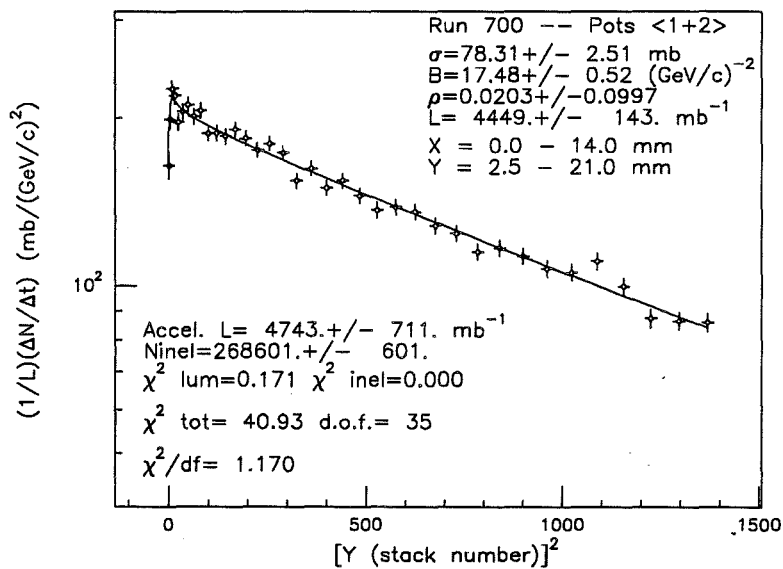


Figure 25: Fits to run 750 and the 700 series of the 1.8 TeV data

RUN 600

--

CHAMBERS 2-7

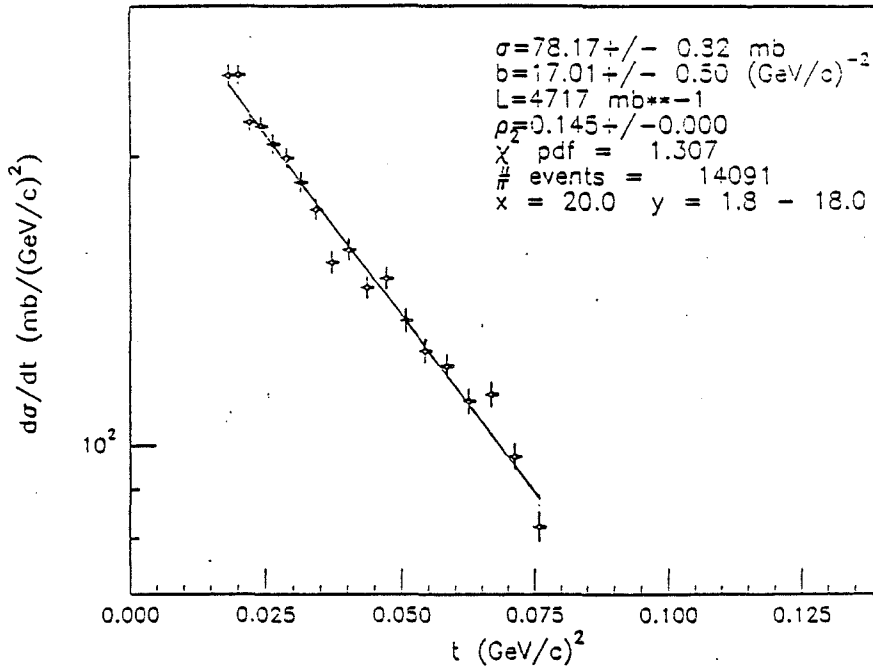


Figure 26: A $d\sigma/dt$ vs $|t|$ fit for σ_t and B from the E710 1989 analysis of the 1.8 TeV data

fixed at the theoretically predicted value of 0.145. No knowledge of the number of inelastics was available at the time either, so the data were normalized only by the accelerator luminosity. This analysis resulted in: $\sigma_t = 78.3 \pm 5.9$ mb, $B = 16.3 \pm 0.5$ (GeV/c) $^{-2}$, $\sigma_{el} = 19.6 \pm 3.0$ mb, and $\sigma_{el}/\sigma_t = 0.25 \pm 0.02$. Fig. 26 shows a fit to one of the series of runs analyzed.

Results from the second analysis of the 1.8 TeV data were released in 1991. This time, the beam halo background noise was modeled and removed from the data[26]. This allowed the extension of the analysis to a much lower $|t|$ region ($|t| \geq 0.0014$ (GeV/c) 2) than before. The data were normalized only by the number of inelastics, i.e., the luminosity-free method described in Section 2.1. The lower $|t|$ coverage allowed the simultaneous fit of σ_t , B , and ρ . The results were $\sigma_t = 72.8 \pm 3.1$ mb, $B = 16.99 \pm 0.47$ (GeV/c) $^{-2}$, and $\rho = 0.140 \pm 0.069$. The curve for the best fit to these data is shown in Fig. 27.

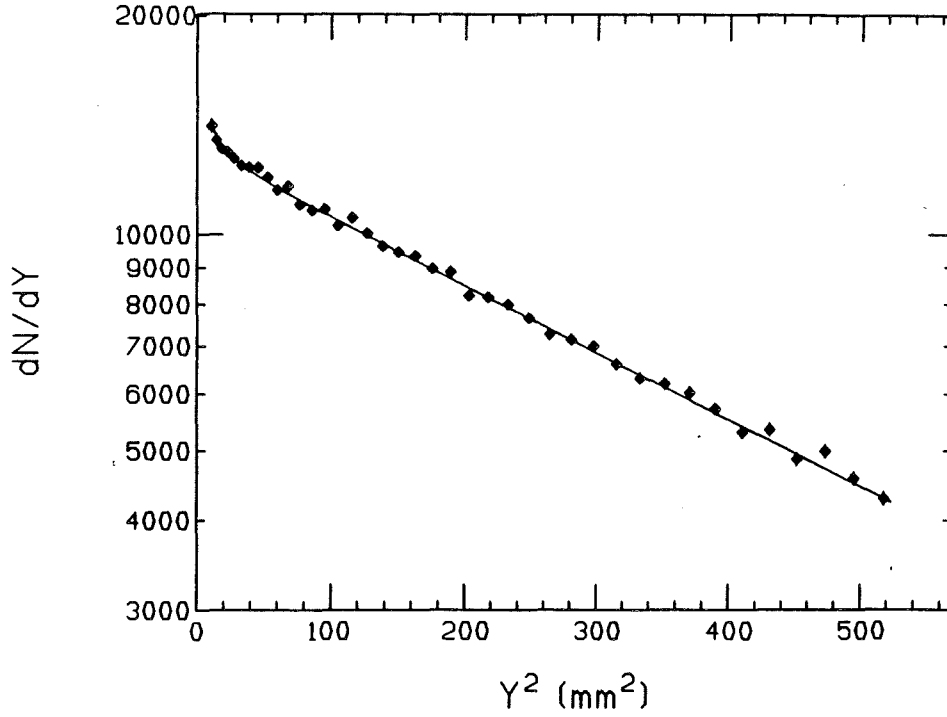


Figure 27: The dN/dy vs y^2 fit for elastic scattering distribution, for almost all of the E710 1991 analysis

The results discussed in this work represent the third and final analysis of the E710 low $|t|$ data at $\sqrt{s} = 1.8$ TeV. A modified background-subtraction procedure and more straightforward acceptance corrections allow penetration to a minimum $|t|$ of $0.00075 \text{ (GeV/c)}^2$. The simultaneous normalization of the data by the inelastics and the luminosity allow a more accurate determination of the cross section.

E710 has also conducted measurements at a *high* $|t|$. The parameters measured were the nuclear curvature parameter C and the ratio of the elastic to total cross section σ_{el}/σ_t . Fig. 28 is a plot of the fit to $d\sigma/dt$ vs high $|t|$. The curvature parameter was measured to be $C = 0.14 \pm 0.70 \text{ (GeV/c)}^{-4}$, i.e., compatible with zero. This result, in conjunction with the positive C values measured at lower energies at the ISR[44,1] and the SppS[1,51], signal the transformation of the nucleon to a sharp disk with increasing s . The Tevatron energy of 1.8 TeV is the energy at which

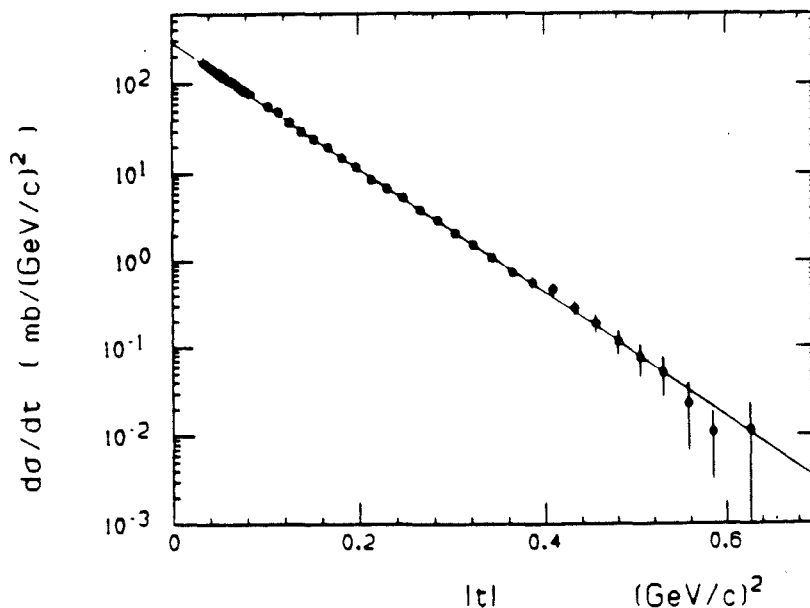


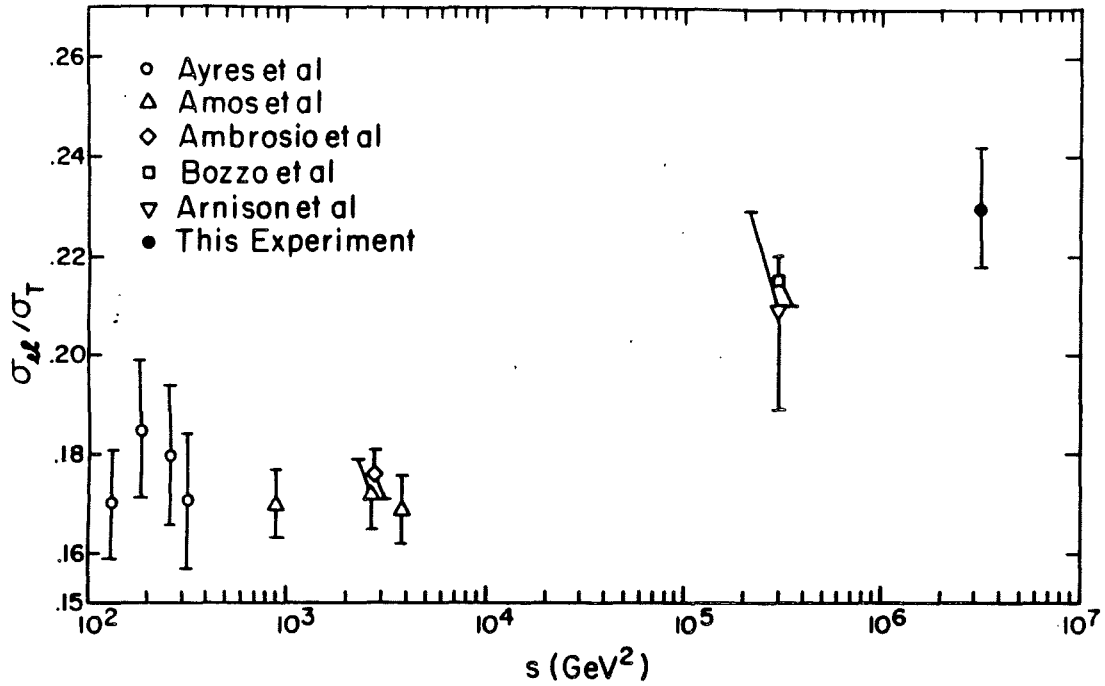
Figure 28: Fit to $d\sigma/dt$ vs $|t|$ in the high $|t|$ region at 1.8 TeV

the curvature parameter C makes the transition from positive to negative values.

The ratio of the elastic to total cross section was measured to be 0.230 ± 0.024 . This value, along with the lower energy data from other experiments, is shown in Fig. 29. From this figure it can be seen that as s increases from ISR energies, the ratio σ_{el}/σ_t rises. This indicates that the nucleon becomes blacker with increasing energy, although this ratio is still well below the asymptotic value of 0.5 which would indicate the transformation of the nucleon to a black disk.

5.1.3 Diffraction Dissociation at 1.8 TeV

In 1990, E710 normalized their single diffraction events to LR events. The LR events were discussed in the section on inelasticities (Section 4.7.1). E710 measured the total single-diffractive cross section[41] of $2\sigma_{sd} = 11.7 \pm 2.3$ mb at $\sqrt{s} = 1.8$ TeV. The factor 2 indicates that the quantity is

Figure 29: The world σ_{el}/σ_t data

the *total* cross section, i.e., the sum of the diffractive dissociation of the proton *and* the antiproton; the two are always taken to be equal. In 1993, E710 studied single diffractive dissociation ($\bar{p}p \rightarrow \bar{p}X$) at $\sqrt{s} = 1.8$ TeV[32] using an experimental technique different from that used in 1990. The dissociated particle mass and momentum transfer covered the ranges $3 < M_X < 200$ GeV and $0.05 < |t| < 0.11$ (GeV/c) 2 , respectively. The quantities M_X and t are assumed independent, i.e.,

$$\frac{d\sigma}{dt dM_X^2} = A f(t) g(M_X^2). \quad (51)$$

For functions f and g , E710 used the forms

$$f(t) = e^{bt}, \text{ and} \quad (52)$$

$$g(M_X^2) = (M_X^2)^{-\alpha}, \quad (53)$$

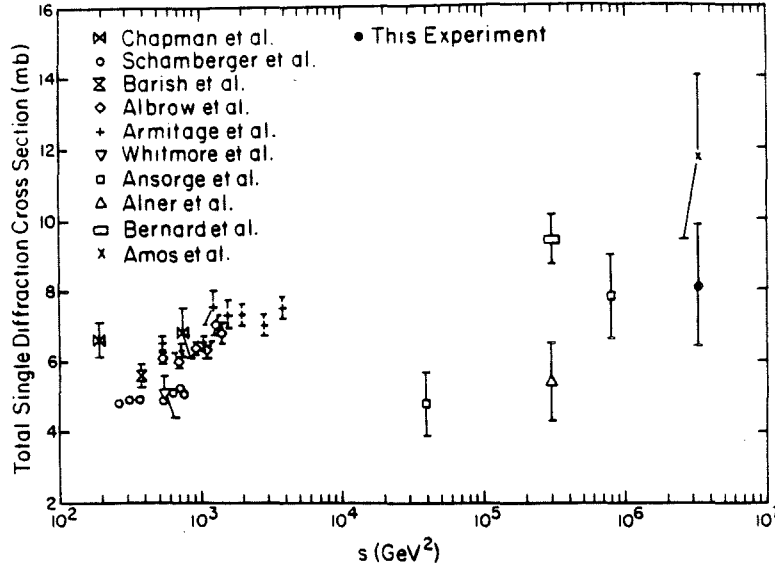


Figure 30: The world pp and $\bar{p}p$ total single-diffractive cross section data

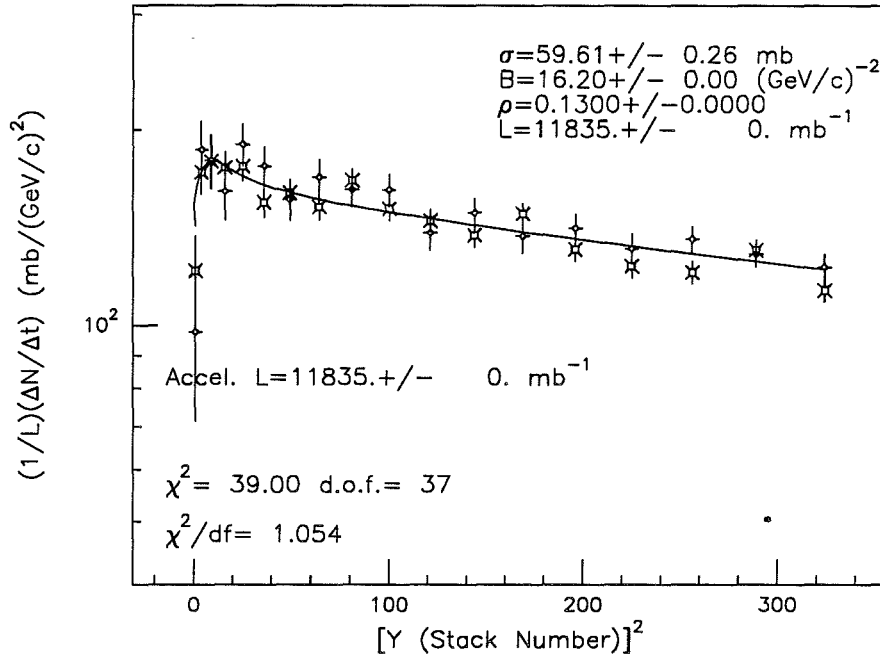
and used the data to obtain b , α , and the total cross section for diffraction dissociation given by

$$2\sigma_{sd} = 2 \int \int \frac{d\sigma}{dt dM_X^2} dt dM_X^2, \quad (54)$$

where the integrations are carried out over all values of t and $2 \text{ GeV}^2 < M_X^2 < 0.05 s$.

The fit to the data yielded $\alpha = 1.13 \pm 0.07$, which was consistent with some theoretical models expecting an M_X^{-2} dependence. Furthermore, b was measured to be $10.5 \pm 1.8 (\text{GeV}/c)^{-2}$, which was about half of the nuclear slope parameter for elastic scattering. The total single-diffractive cross section was measured to be $2\sigma_{sd} = 8.1 \pm 1.7 \text{ mb}$, which was in reasonable agreement with the 1990 result. The $\chi^2/\text{degree of freedom}$, however, was quite high at 3.5. This is probably due to the breakdown of the assumption that M_X and t are independent. On the other hand, the elastic nuclear slope parameter B measured by the procedure used here was found to be $B = 17.9 \pm 2.5 (\text{GeV}/c)^{-2}$, which agrees well with the published value of $17.0 \pm 0.5 (\text{GeV}/c)^{-2}$. This reinforces

8-NOV-93 11:38:57

Figure 31: Fit to the 1.02 TeV data at low $|t|$ range

confidence in the results for α and b . The total single-diffractive cross section result from this experiment together with previous pp and $\bar{p}p$ data, and the earlier E710 result[41] are shown in Fig. 30.

5.2 The 1.02 TeV Data

The 1.02 TeV data were from only one store. The fit to the data is shown in Fig. 31. Here, B was fixed at $16.2 \text{ (GeV/c)}^{-2}$, which was obtained from an independent measurement using data at a higher $|t|$ range[43]. The data were normalized by the the accelerator luminosity only, since there was no reliable estimate of the number of inelastics.

These data did not contain enough information in the Coulomb region to yield a reliable ρ

Source	σ_t (mb)
Luminosity	4.15
Background normalization constant	0.287
B	0.370
L_x	0.225
L_y	0.1792
Pot position	0.0238
Calibration	0.00691
Pattern width	0.00300
Quadrature sum of systematic errors:	4.19
Statistical error:	0.264
Overall error:	4.2

Table 6: Systematic error contributions for 1.02 TeV data

value. The only parameter fitted to the data was therefore the total cross section σ_t . The ρ value was fixed at 0.13, which is the most current value predicted by theory (see Section 6). The 15% error of the luminosity was treated as systematic. The breakdown of the contribution of various factors to the overall errors is shown in Table 6. The overall errors are the quadrature sum of the statistical and systematic uncertainties. The 1.0 TeV total cross section obtained from these data, which are taken at *low* $|t|$, is

$$\sigma_t = 59.6 \pm 4.2 \text{ mb},$$

$$\frac{\sigma_{el}}{\sigma_t} = 0.191 \pm 0.016.$$

An independent measurement of elastic scattering at $\sqrt{s} = 1.02$ TeV at a higher $|t|$ range ($0.065 \leq |t| \leq 0.21$ (GeV/c)²) was conducted by E710[43] in 1992. The slope parameter was measured to be $B = 16.2 \pm 0.7$ (GeV/c)⁻², which was the value at which B was fixed in the low $|t|$

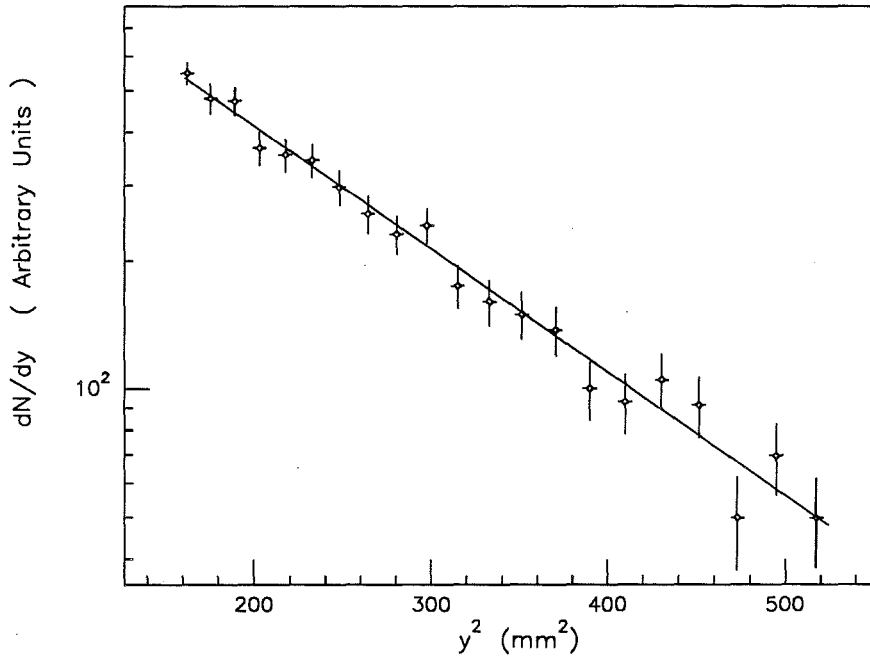


Figure 32: Fit to the 1.02 TeV data at high $|t|$ range

analysis described above. Using the optical theorem and the accelerator luminosity, they obtained $\sigma_t \sqrt{1 + \rho^2} = 61.7 \pm 5.7$ mb. The fit to the measured variation of dN/dy vs y^2 is shown in Fig. 32. The solid line is the fit to an exponential function in y^2 in the range $161.3 \text{ mm}^2 \leq y^2 \leq 501.8 \text{ mm}^2$.

Substituting the theoretical value of $\rho = 0.13$ into the high $|t|$ E710 measurement of $\sigma_t \sqrt{1 + \rho^2}$, one obtains the total cross section of $\sigma_t = 61.2 \pm 5.7$ mb. This cross section is virtually independent of that obtained from the low $|t|$ measurement. The only common parameter between the two measurements is B , which is measured at high $|t|$ and fixed at low $|t|$. However, since the uncertainty of B has a negligible effect on the low $|t|$ measurements, as indicated in Table 6, one can consider the high and low $|t|$ measurements independent of each other, and therefore average their total

cross sections. This yields a complete cross section measurement at $\sqrt{s} = 1.02$ TeV:

$$\sigma_t = 60.2 \pm 3.4 \text{ mb, and}$$

$$\frac{\sigma_{el}}{\sigma_t} = 0.193 \pm 0.014.$$

6 Models of Elastic Scattering

The E710 energy of $\sqrt{s} = 1.8$ TeV is the highest so far achieved for this class of experiments. It therefore provides a very large lever arm for the fits that are discussed here.

Three independent and apparently contradictory theoretical models have been fitted to the world data of σ_t , B , and ρ for both pp and $\bar{p}p$ scattering:

- The Regge pole scenario[52],
- An analytic asymptotic amplitude analysis[51], and
- A QCD-inspired eikonal model[49].

All *three* models fit the data quite well.

6.1 The Regge Pole Picture

The Regge pole model of the Pomeron was constructed by Landshoff and Donnachie[52]. According to this model, the world σ_t vs. s data for pp and $\bar{p}p$ can be approximated as

$$\sigma_t = 22 s^{0.08} \text{ mb.} \quad (55)$$

Furthermore, a Regge pole amplitude using the Regge trajectory

$$\alpha(t) = 1.08 + 0.2t \quad (56)$$

provides a good first approximation to near-forward elastic scattering from ISR to Tevatron energies. The increase of B with s is generally associated with a single Pomeron Regge pole having a linear trajectory whose slope is the derivative $\alpha' = 0.2$ of the Regge trajectory of Eq. 56, and can be expressed as

$$B = B_0 + 2\alpha' \log s. \quad (57)$$

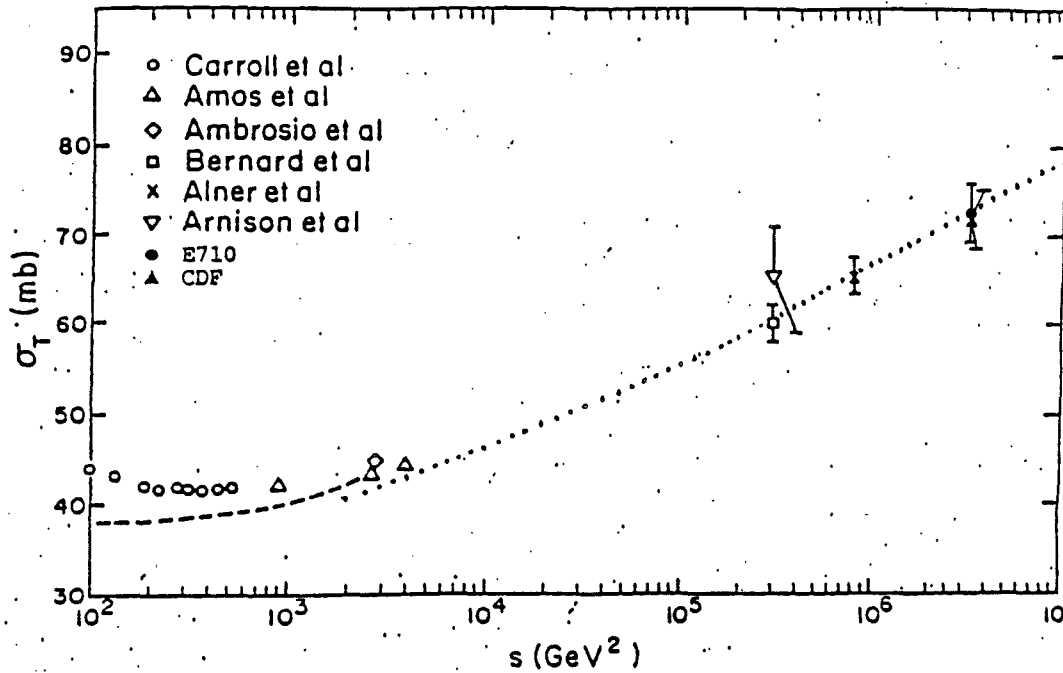


Figure 33: $\sigma_t(\bar{p}p)$ vs. s . The dashed line shows the behavior of $\sigma_t(pp)$, and the dotted line is given by the Regge pole formula of Landshoff and Donnachie (Eq. 55).

The fit of this model to the current world data of σ_t and B for $\bar{p}p$ scattering is shown⁵ in Figs. 33 and 34.⁶ The dashed line in Fig. 33 is the power behavior of the cross section given by Eq. 55. Both of these figures demonstrate that the E710 and CDF results are consistent with this simple model.

From the differential dispersion relations, the real part of the pp scattering amplitude f_{pp} can be approximated as

$$\frac{4\pi}{p} \text{Re} f_{pp} \approx \frac{\pi}{2} \frac{d\sigma_t}{d(\log s)}. \quad (58)$$

⁵The figures in this section are taken from the review by Block, Kang, and White[48].

⁶The datum points used in Figs. 33-47 are limited to those published prior to June, 1992. Specifically, the CDF and E710 σ_t and ρ values are those released in 1991.

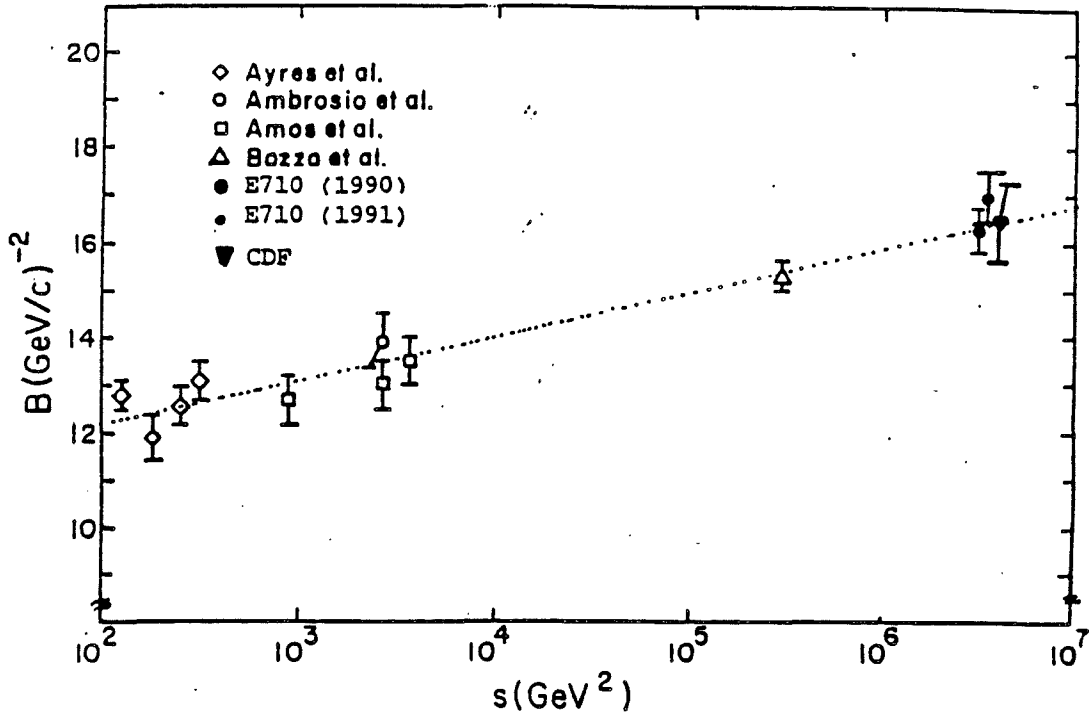


Figure 34: $B(\bar{p}p)$ vs. s . The dotted line is given by the Pomeron Regge trajectory formula of Landshoff and Donnachie (Eq. 57).

Using the power behavior of σ_t with s given in Eq. 55, the right side of Eq. 58 can be evaluated as

$$\frac{4\pi}{p} \text{Re} f_{pp} \approx \frac{\pi}{2} \times 0.08 \times \sigma_t. \quad (59)$$

The imaginary part of the scattering amplitude is related to the total cross section according to the optical theorem (Eq. 98). The ratio of the real to the imaginary part of the amplitude thus yields a ρ value of

$$\rho = \frac{\pi}{2} \times 0.08 \approx 0.12. \quad (60)$$

This Regge pole model therefore yields a constant value of ρ which is about *half* of the UA4 value of 0.24 ± 0.04 [9]. As mentioned in the Introduction section (Section 1), the UA4/2 group eventually re-measured[22] ρ to be 0.135 ± 0.02 which was in agreement with the prediction of the Regge pole model.

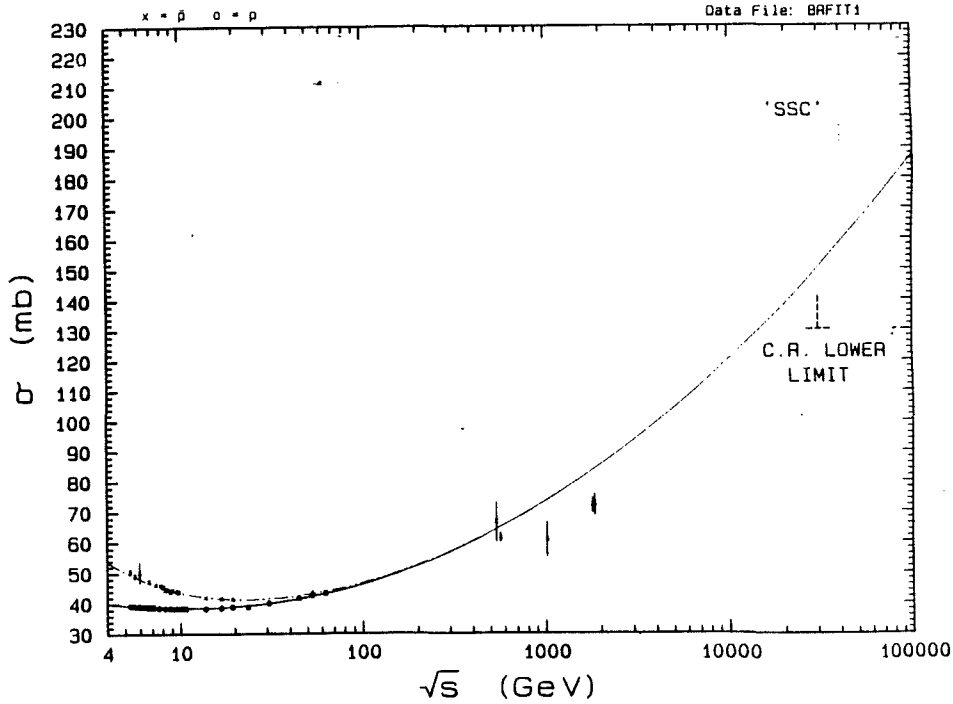


Figure 35: Cross section vs. energy for pp (\circ) and $\bar{p}p$ (\times) scattering, with a $\log^2 s$ variation, and no Odderon.

There are serious problems with this simple picture that are not readily resolvable. First, it is immediately obvious that the simple s dependence given in Eq. 55 does not satisfy unitarity. Secondly, the t dependence of the differential cross section in this model is that of a constant slope with *no* curvature. Although this model can be modified to exhibit positive curvature at $\sqrt{s} \leq 540$ GeV, as measured at the ISR[1,44,51] and $S\bar{p}pS$ [1,51], it cannot at the same time explain the vanishing of curvature at $\sqrt{s} = 1.8$ TeV[53]. By the same token, this model cannot explain the secondary diffraction maxima observed at large $|t|$ at the ISR[15] and $S\bar{p}pS$ [16].

Since the Regge model of the rise of the cross section with energy, given in Eq. 55, violates unitarity, its prediction of the cross section at higher energies provides an upper bound to the predicted cross sections of the future accelerators.

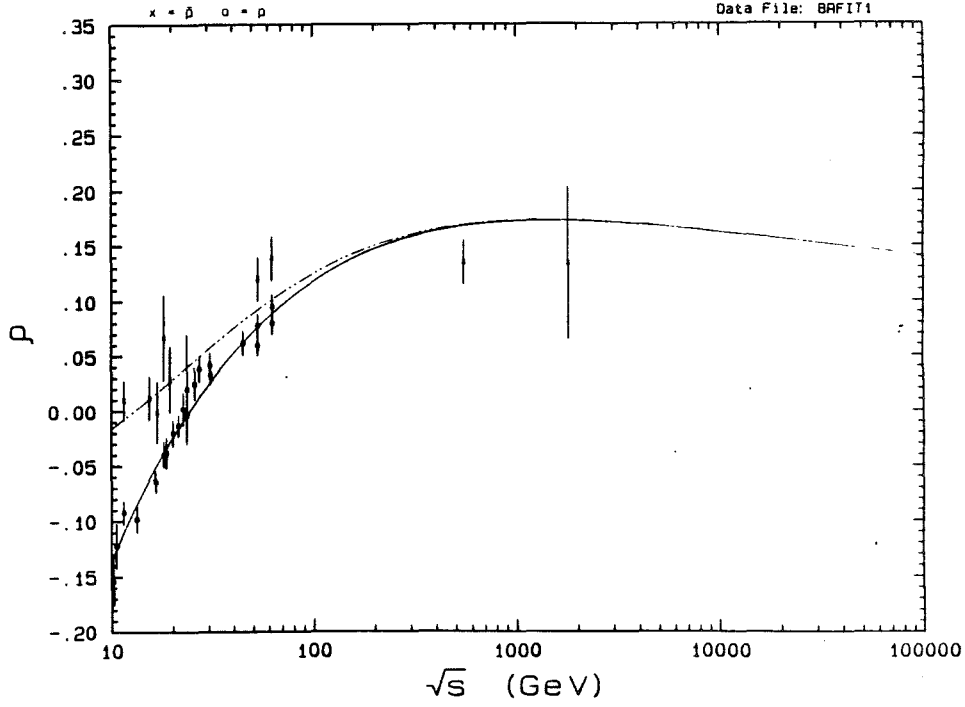


Figure 36: ρ vs. energy for pp (\circ) and $\bar{p}p$ (\times) scattering, with a $\log^2 s$ variation, and no Odderon.

6.2 Analytic Asymptotic Amplitude Analysis of Elastic Scattering

The Froissart bound states that the rise of pp and $\bar{p}p$ cross sections with s is asymptotically bounded by $\frac{\pi}{m_\pi^2} \log^2 \frac{s}{s_0}$, where m_π is the rest mass of pion and s_0 is a scale factor[14]. The scattering amplitude, therefore, cannot cause σ_i to asymptotically rise faster than $\log^2 s$.

Based on the available data corresponding to the energy range $5 \leq \sqrt{s} \leq 1800$ GeV, Block and Cahn[44] parametrized the elastic scattering amplitude f in terms of an even amplitude f_+ and an odd amplitude f_- such that

$$f_{pp} = \frac{f_+ - f_-}{2}, \quad (61)$$

$$f_{p\bar{p}} = \frac{f_+ + f_-}{2}. \quad (62)$$

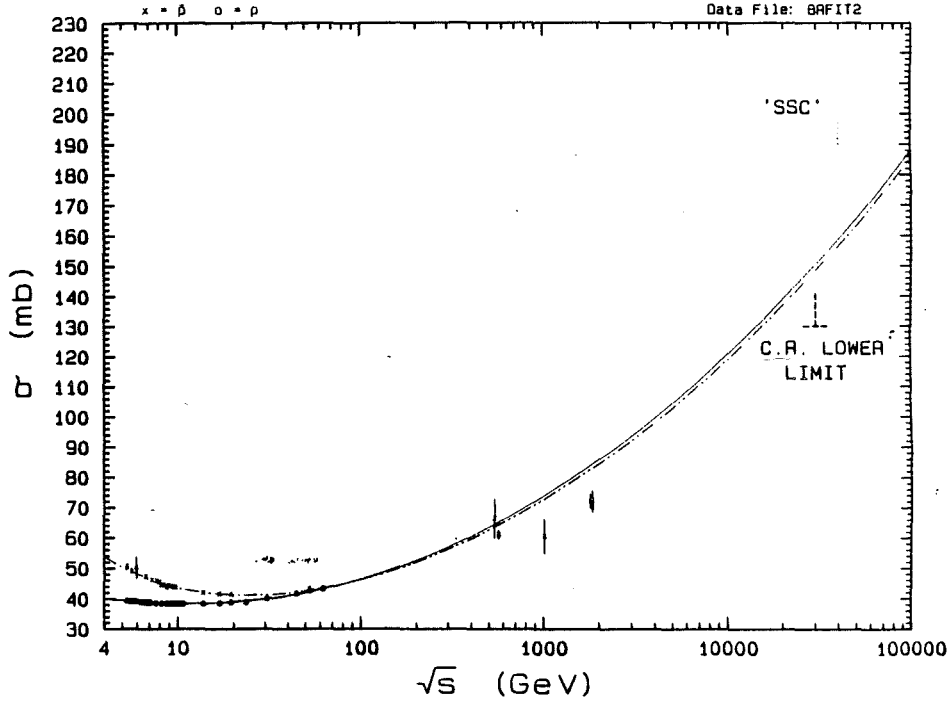


Figure 37: Cross section vs. energy for pp (\circ) and $\bar{p}p$ (\times) scattering, with a $\log^2 s$ variation, and Odderon 2.

These amplitudes had the form

$$\frac{4\pi}{p} f_+ = i \left(A + \beta \left[\log \left(\frac{s}{s_0} \right) - i \frac{\pi}{2} \right]^2 + c s^{\mu-1} e^{i\pi(1-\mu)/2} \right), \quad (63)$$

$$\frac{4\pi}{p} f_- = -D s^{\alpha-1} e^{i\pi(1-\alpha)/2}. \quad (64)$$

Here, A , β , s_0 , c , μ , D , and α are all parameters fitted to existing experimental data. The quantities s and p are the square of the c.m. energy and the c.m. momentum of either incoming particle, respectively. From the optical theorem, we have

$$\sigma^\pm = \frac{4\pi}{p} \text{Im} f_\pm, \quad (65)$$

from which follows that

$$\sigma(pp) = \frac{\sigma^+ - \sigma^-}{2}, \quad (66)$$

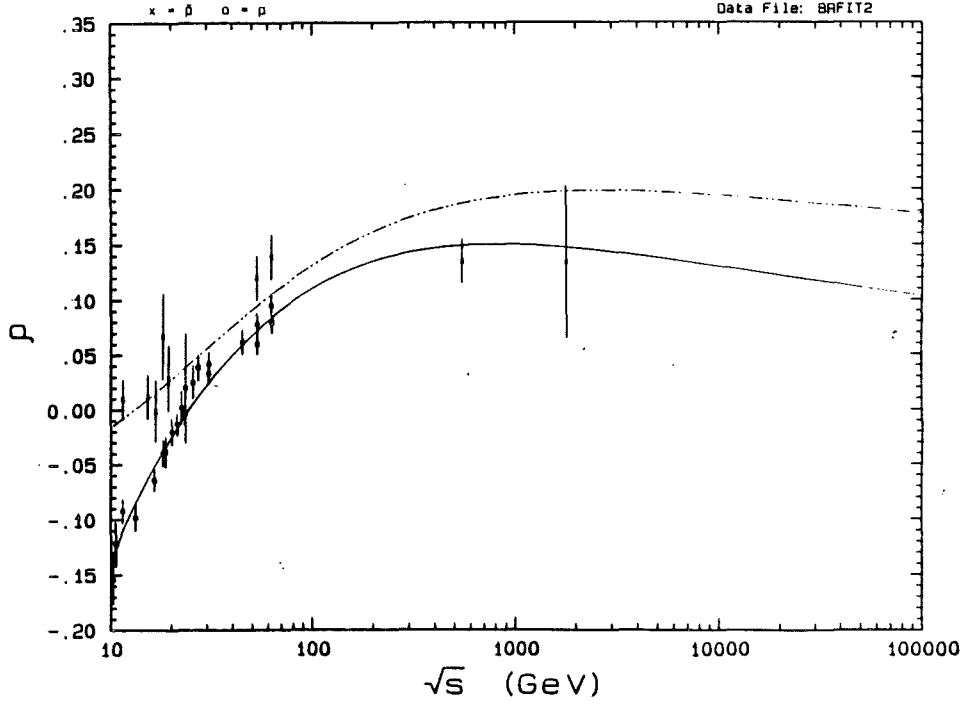


Figure 38: ρ vs. energy for pp (\circ) and $\bar{p}p$ (\times) scattering, with a $\log^2 s$ variation, and Odderon 2.

$$\sigma(p\bar{p}) = \frac{\sigma^+ + \sigma^-}{2}, \quad (67)$$

$$\rho_{pp} = \frac{\text{Re}(f_+ - f_-)}{\text{Im}(f_+ - f_-)} \quad (68)$$

$$\rho_{p\bar{p}} = \frac{\text{Re}(f_+ + f_-)}{\text{Im}(f_+ + f_-)}. \quad (69)$$

The $cs^{\mu-1}$ and $Ds^{\alpha-1}$ terms are referred to as the even and odd Regge exchange terms, respectively. The term in β results in a $\log^2 s$ rise, and A is the constant part of the cross section. In the fit to the data, the parameter α was found to be about 0.5, and therefore the odd amplitude vanishes as $s \rightarrow \infty$.

Block and White[51] fitted the above asymptotic amplitudes to the world data. It is important to keep in mind that the data by themselves may not exhibit the asymptotic behavior. These measurements were taken at energies of up to $\sqrt{s} = 1.8$ TeV. Below this energy, the ISR[1,44,51]

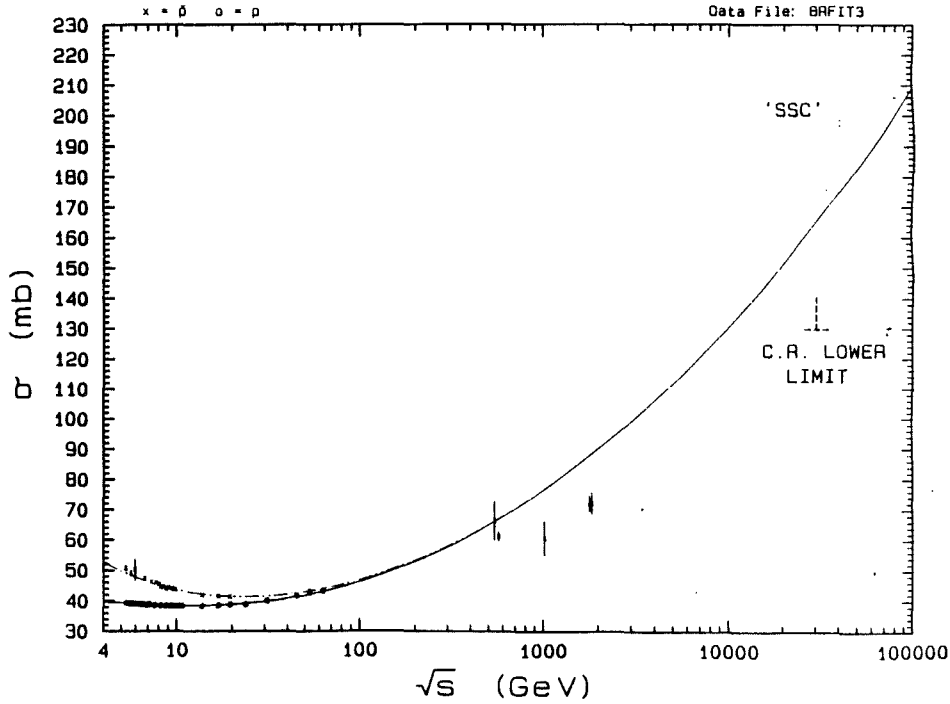


Figure 39: Cross section vs. energy for pp (\circ) and $\bar{p}p$ (\times) scattering, with a $\log^2 s$ variation, and Odderon 1.

and $\bar{S}ppS$ [1,51] experiments measured positive values for the nuclear curvature parameter C . E710 measured the curvature C to be consistent with zero[53], indicating that this is the energy at which the nucleon begins the transition to disk-like behavior, i.e., to 'asymptopia'.

There are no data available at higher energies, and hence it is likely that we are not yet in 'asymptopia'. The analysis being discussed here therefore may *not* be using asymptotic data. It *does*, however, describe the data exceedingly well at present energies.

Eden and Kinoshita[18] have derived that if $\sigma(p\bar{p})$ and $\sigma(pp)$ grow as $\log^\gamma s$, then $\sigma(p\bar{p}) - \sigma(pp) \rightarrow \log^{\gamma/2} s$ as $s \rightarrow \infty$. Fitting the above asymptotic amplitudes to the data, on the other hand, results in $\sigma(p\bar{p}) - \sigma(pp) \rightarrow 0$ and $\rho(p\bar{p}) - \rho(pp) \rightarrow 0$ as $s \rightarrow \infty$. Therefore, three types of odd amplitudes,

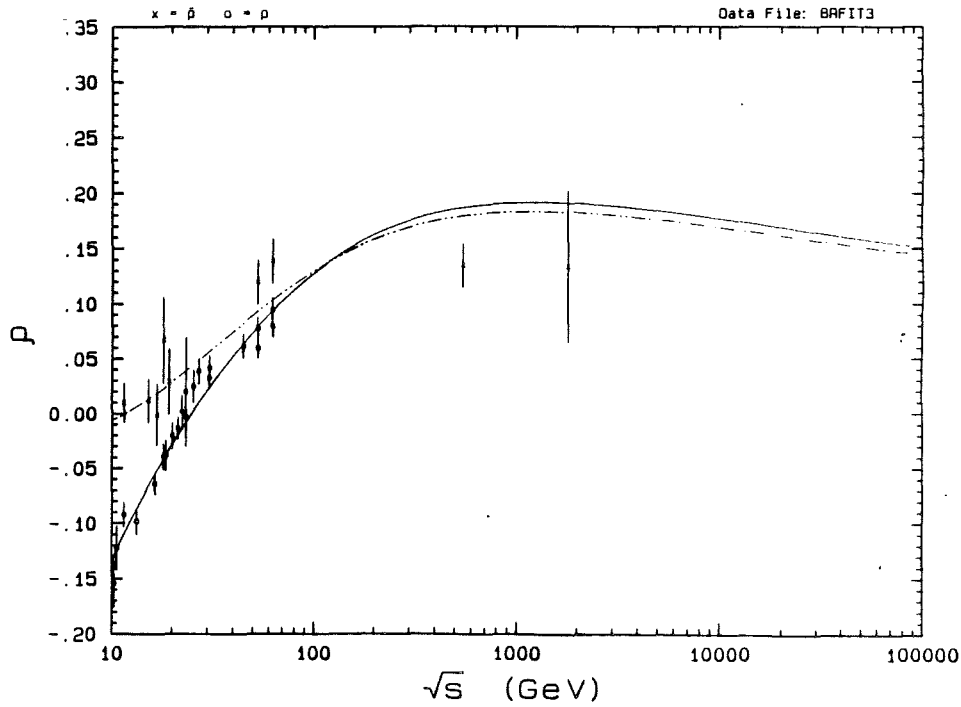


Figure 40: ρ vs. energy for pp (\circ) and $\bar{p}p$ (\times) scattering, with a $\log^2 s$ variation, and Odderon 1.

referred to as Odderons, that do *not* vanish asymptotically were introduced via the forms

$$\frac{4\pi}{p} f_-^{(0)} = -\epsilon^{(0)}, \quad (70)$$

$$\frac{4\pi}{p} f_-^{(1)} = -\left[\log \frac{s}{s_0} - i\frac{\pi}{2}\right] \epsilon^{(1)}, \quad (71)$$

$$\frac{4\pi}{p} f_-^{(2)} = -\left[\log \frac{s}{s_0} - i\frac{\pi}{2}\right]^2 \epsilon^{(2)}. \quad (72)$$

The complete odd amplitude is the sum of the conventional odd amplitude of Eq. 64 with one (or none) of the Odderons of Eqs. 70-72. Block and White[51] constructed these composite odd amplitudes and fitted them to the world pp and $\bar{p}p$ data of σ_t and ρ . The results of each fit are summarized below⁷

⁷The figures in this section are taken from Ref. [51].

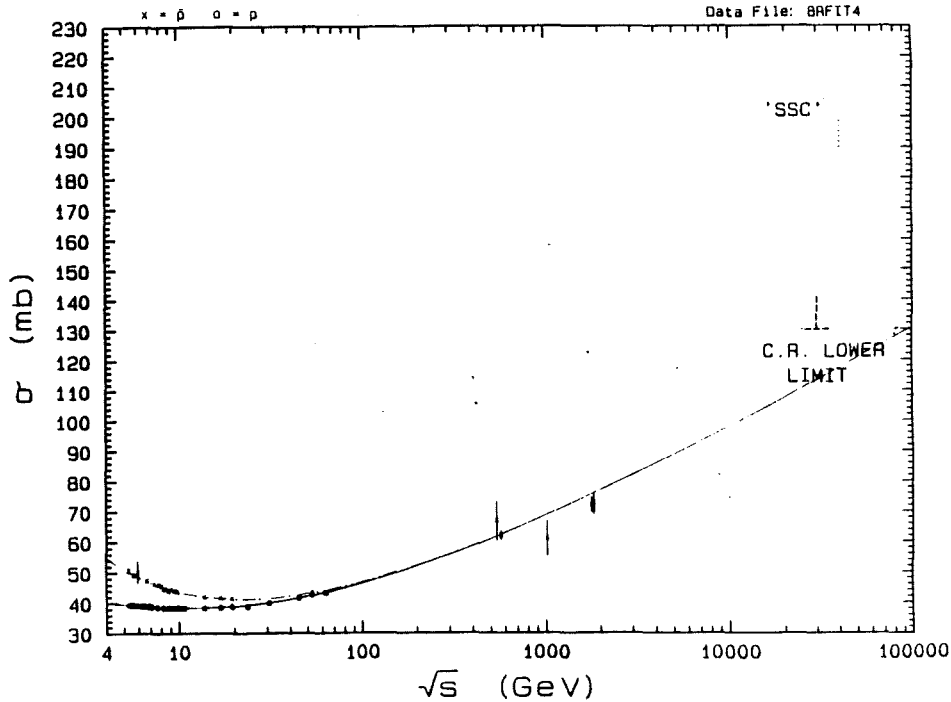


Figure 41: Cross section vs. energy for pp (\circ) and $\bar{p}p$ (\times) scattering, with a $\log s$ variation, and no Odderon.

- The first fit used the conventional even amplitude and no Odderons in the odd amplitude. The $\chi^2/\text{d.f.}$ ($\chi^2/\text{degree of freedom}$) of this fit was 2.03, indicating a poor fit. The computed curves are shown in Figs. 35 and 36. As the figures show, there is more than a 3 standard deviation discrepancy between the Tevatron (E710 and CDF) total cross sections and the predicted value of the fit. Furthermore, it predicts too high a ρ at 546 GeV and 1.8 TeV. It is therefore concluded that a simple $\log^2 s$ behavior does not fit the data.
- The second fit added the Odderon of Eq. 72 (Odderon 2) to the conventional odd amplitude of Eq. 64, and used it along with the conventional even amplitude. The curves are shown in Figs. 37 and 38. The $\chi^2/\text{d.f.}$ of this fit was 1.93, i.e., another poor fit. Again, the predicted cross section at 1.8 TeV is too high, as is the predicted ρ value at 540 GeV. The fitted value of

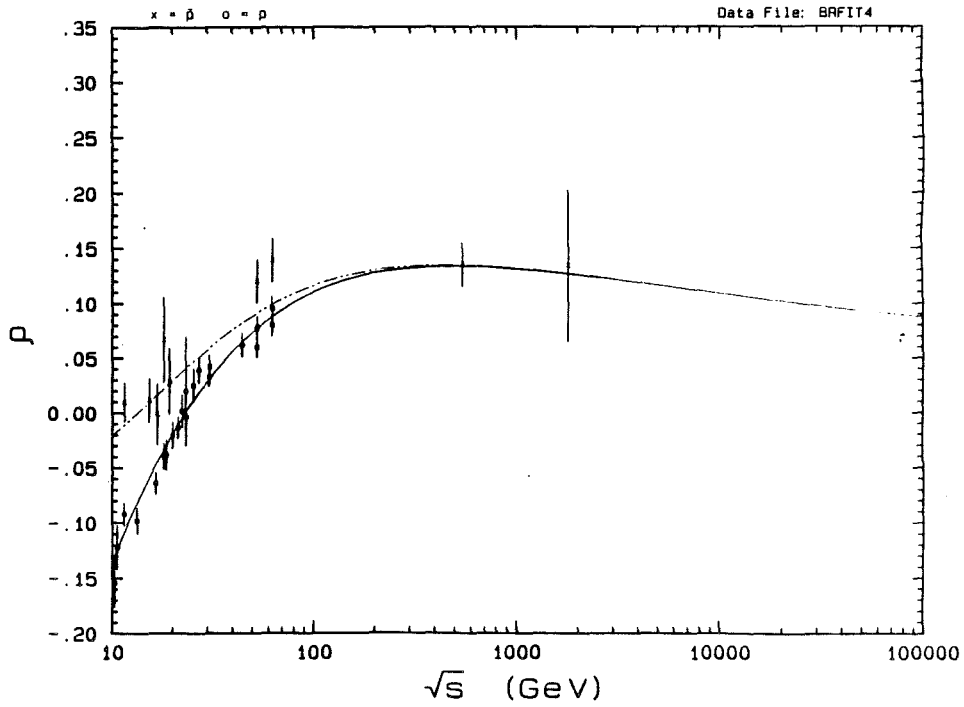


Figure 42: ρ vs. energy for pp (\circ) and $\bar{p}p$ (\times) scattering, with a $\log s$ variation, and no Odderon.

the Odderon amplitude was $\epsilon^{(2)} = -0.022 \pm 0.011$ mb which is only two standard deviations from zero, and does not play a major role in the fit.

- The third fit added Odderon 1 (Eq. 71) to the odd amplitude and used it along with the conventional even amplitude. The curves are shown in Figs. 39 and 40. This fit was the worst of the first three with a $\chi^2/\text{d.f.}$ of 2.65. It exhibited the same problems as the first two fits.

Block and White thus concluded that an even amplitude varying as $\log^2(s/s_0)$ does *not* fit the world data. This demonstrates that the experimental cross section does not rise as rapidly as $\log^2(s/s_0)$ in the currently accessible energy region. The addition of an Odderon does not affect this situation. Block and White then considered an asymptotic variation that goes as $\log(s/s_0)$

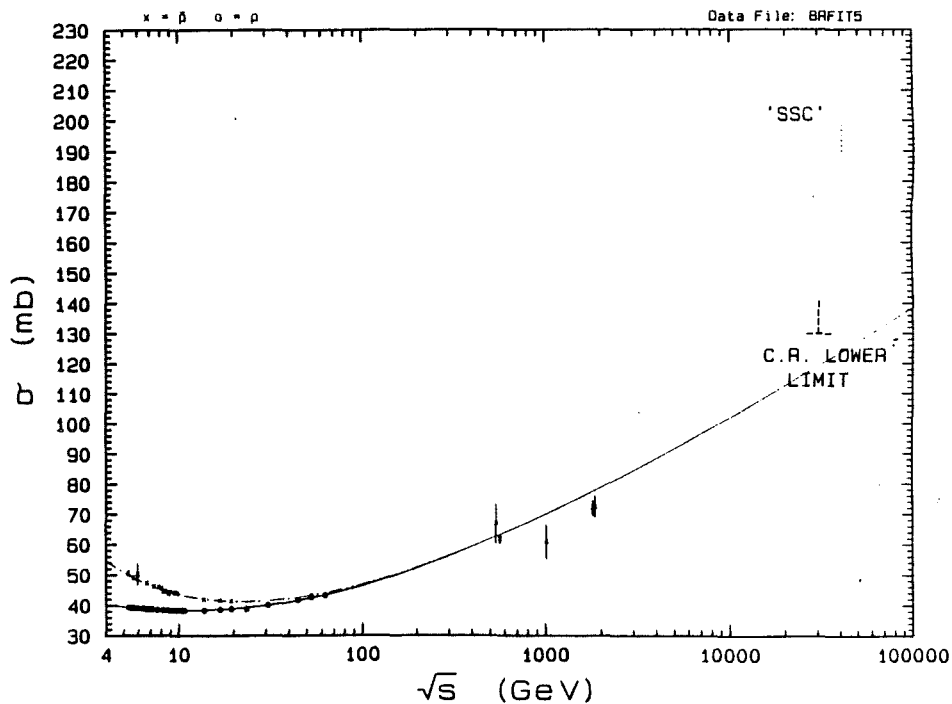


Figure 43: Cross section vs. energy for pp (\circ) and $\bar{p}p$ (\times) scattering, with a $\log s$ variation, and Odderon 1.

with an even amplitude of the form

$$\frac{4\pi}{p} f_+ = i \left(A + \beta \left[\log \left(\frac{s}{s_0} \right) - i \frac{\pi}{2} \right] + cs^{\mu-1} e^{i\pi(1-\mu)/2} \right). \quad (73)$$

They then used the conventional odd amplitude of Eq. 64, along with no Odderon or Odderon 1, but *not* Odderon 2 since it is not allowed for a $\log s$ fit:

- The first fit used no Odderon in the odd amplitude, and used the new even amplitude of Eq. 73. The curves are plotted in Figs. 41 and 42. The $\chi^2/\text{degree of freedom}$ of the fit was 1.26, which was much more reasonable than the high values (> 2) corresponding to the $\log^2 s$ models.
- The last fit added Odderon 1 to the odd amplitude, and used the even amplitude of Eq. 73. The curves are plotted in Figs. 43 and 44. The $\chi^2/\text{d.f.}$ of this fit was 1.24, making it almost

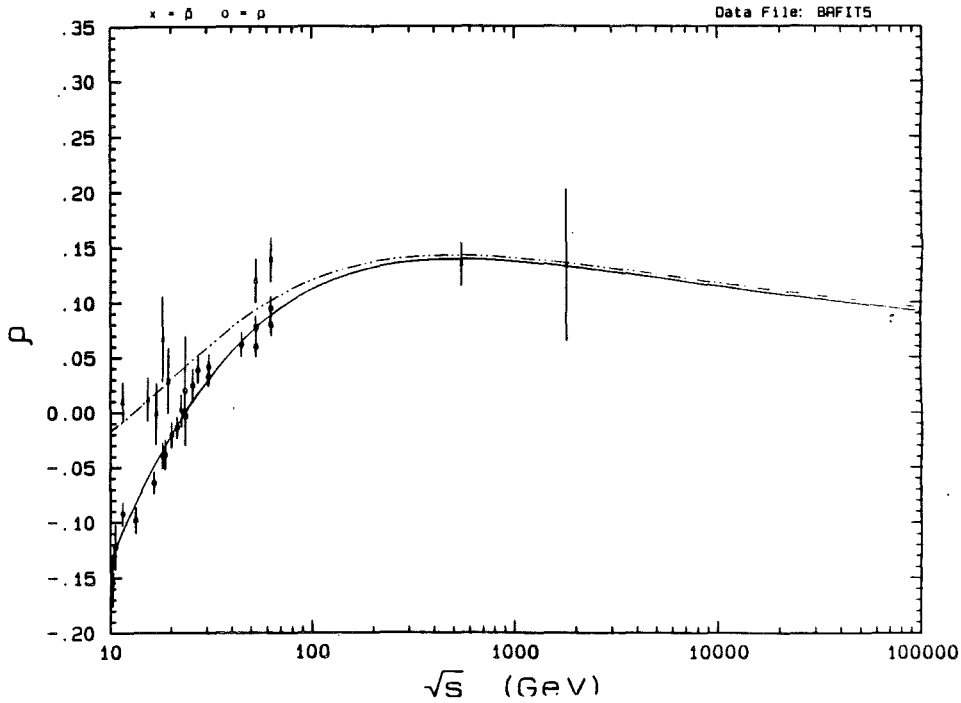


Figure 44: ρ vs. energy for pp (\circ) and $\bar{p}p$ (\times) scattering, with a $\log s$ variation, and Odderon 1.

indistinguishable from the fit with no Odderon.

It is observed that the introduction of an Odderon is *not* needed to explain the experimental data. Therefore, an analytic asymptotic amplitude analysis shows that σ_t values in the energy range 5-1800 GeV follow a $\log \frac{s}{s_0}$ behavior, and introduction of a non-vanishing odd amplitude is not required.

At the LHC energy of 16 TeV, this analytic asymptotic model predicts the total cross section to be 104.4 ± 1.0 mb, and at the SSC energy of 40 TeV, 117.4 ± 1.3 mb. The errors are statistical, and are due to the errors of the fitted parameters. As mentioned earlier, the current world data do not extend to high enough energies to contain information about the asymptotic behavior of the cross section, i.e., we are not yet in 'asymptopia'. It is likely that the cross section will ultimately rise faster than $\log s$. The values predicted by this model at the LHC and SSC energies should

therefore be treated as possible lower limits to the actual values.

6.3 QCD-Inspired Model of Elastic Scattering

The eikonalized QCD model of Block, Halzen, and Margolis[49] also explains the pp and $\bar{p}p$ data for σ_t , B , and ρ using the quark-quark, quark-gluon, and gluon-gluon interactions, the last of which is the cause of the rise of the cross section. It also predicts the nuclear curvature parameter to be zero at $\sqrt{s} = 1.8$ TeV and positive at lower energies. Using an impact parameter representation[44], the even and odd scattering amplitudes can be expressed as

$$f^\pm = \frac{p}{\pi} \int d^2b e^{i\mathbf{q} \cdot \mathbf{b}} a^\pm(b, s), \quad (74)$$

where $|\mathbf{b}| = b$ is the impact parameter, and $|\mathbf{q}| = q$ is the momentum transfer such that $t = -q^2$. The impact parameter space representation, $a(b, s)$, of the scattering amplitude can be expressed in terms of even and odd eikonals χ^\pm according to

$$a^\pm(b, s) = \frac{i}{2} \left[1 - e^{-\chi^\pm(b, s)} \right]. \quad (75)$$

As $s \rightarrow \infty$, χ^- vanishes.

To understand the properties of this eikonal model, χ can be re-written in the form

$$2\chi(b, s) = P(b, s), \quad (76)$$

where $P(b, s)$, the probability of collision, can be expressed in terms of the interaction probabilities between the constituents of the colliding nucleons as

$$P = P_{qq} + P_{qg} + P_{gg}. \quad (77)$$

The terms in the summation correspond to quark-quark, quark-gluon, and gluon-gluon interactions, respectively. The gluon-gluon term P_{gg} is factorized into the impact parameter space description

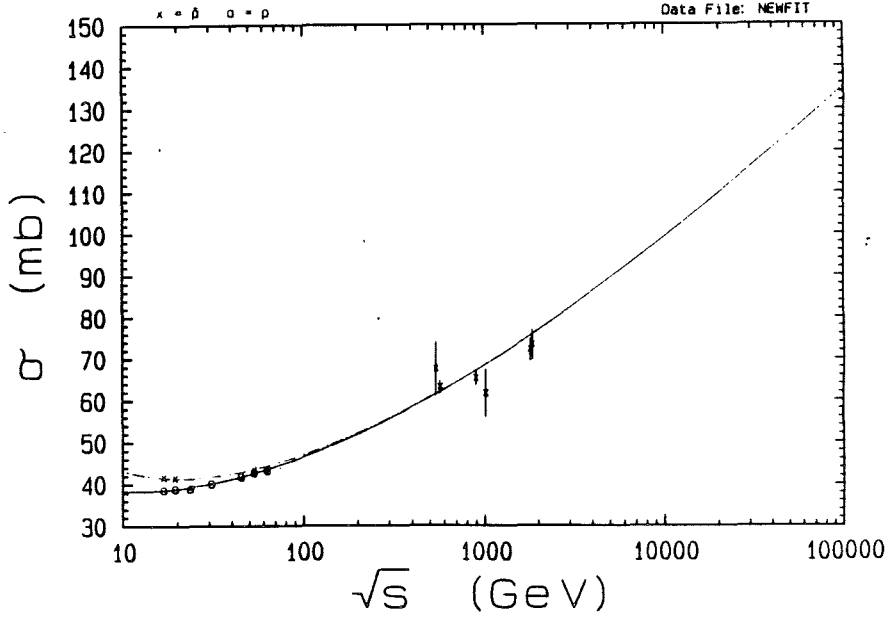


Figure 45: Cross section vs. energy for pp (\circ) and $\bar{p}p$ (\times) scattering, along with eikonalized QCD fit

$\dot{W}_{gg}(b)$, and the QCD glue-gluon cross section, $\sigma_{gg}^{QCD}(s)$, as

$$P_{gg}(b, s) = W_{gg}(b) \sigma_{gg}^{QCD}(s), \quad (78)$$

where

$$W_{gg}(b) = \frac{\mu_{gg}^2}{96\pi} (\mu_{gg} b)^3 K_3(\mu_{gg} b), \quad (79)$$

where K_3 is the modified Bessel function. The mass μ_{gg} sets the scale of the variation in b space, and is the mass in the dipole form factor (Eq. 100) from electron-proton scattering. The glue-gluon cross section is calculated as

$$\sigma_{gg}^{QCD}(s) = \int d\tau F_{gg}(x_1 x_2 = \tau) \sigma_{gg}(\tau s), \quad (80)$$

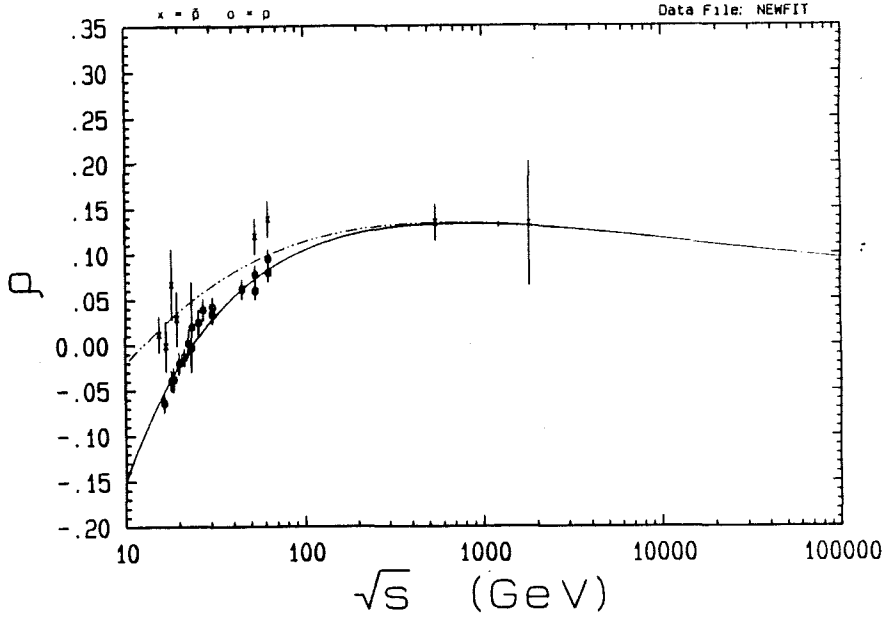


Figure 46: ρ vs. energy for pp (\circ) and $\bar{p}p$ (\times) scattering, along with eikonalized QCD fit

where

$$F_{gg} = \int dx_1 dx_2 f_g(x_1) f_g(x_2) \delta(x_1 x_2 - \tau), \quad (81)$$

$$\sigma_{gg}(\hat{s}) = \frac{9\pi\alpha_s^2}{\delta^2} \theta(\hat{s} - m_0^2). \quad (82)$$

The form used for the gluon structure function is

$$f_g(x) \sim \frac{(1-x)^5}{x^J}. \quad (83)$$

In Regge language, J is known as the Pomeron intercept, and controls the evolution of the gluon structure at small x . In high energies, the energy dependence is controlled by the factor

$$\begin{aligned} \lim_{s \rightarrow \infty} \int_{m_0^2/s}^1 d\tau F_{gg}(\tau) &\sim \int_{m_0^2/s}^1 d\tau \frac{-\log \tau}{\tau^J} \\ &\sim \left(\frac{s}{m_0^2} \right)^{J-1}. \end{aligned} \quad (84)$$

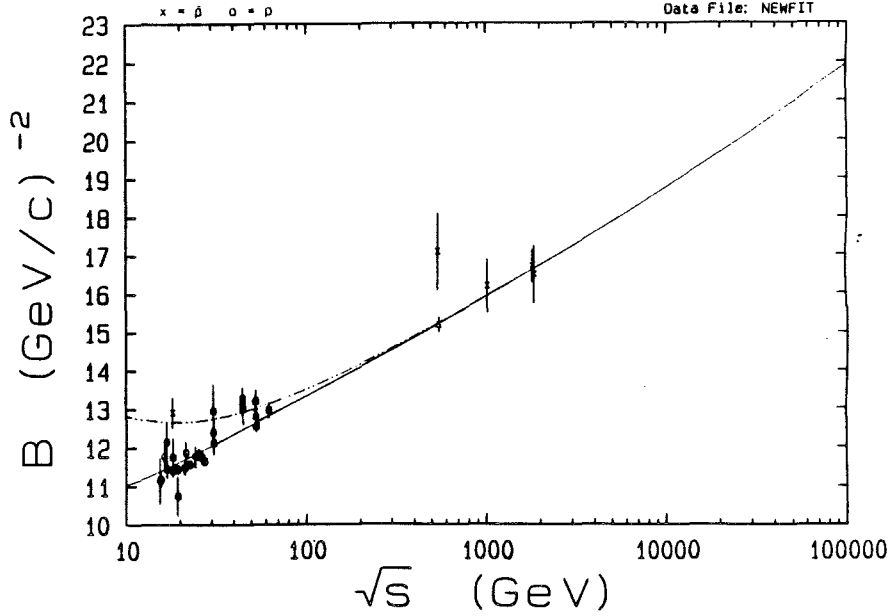


Figure 47: B vs. energy for pp (\circ) and $\bar{p}p$ (\times) scattering, along with eikonalized QCD fit

F_{gg} counts the number of gluons in the colliding hadrons. The number increases rapidly at $x \simeq \frac{m_0}{\sqrt{s}}$ and this is the origin of the rising cross section[49]. In other words, the glue-gluon interaction probability goes as $P_{gg}(b, s) \sim W_{gg}(b)s^{J-1}$. When the number of gluons becomes large, the glue-gluon interaction probability P_{gg} approaches unity for a critical impact parameter b_c given by

$$cW_{gg}(\mu_{gg}b_c)s^{J-1} \sim 1, \quad (85)$$

where c is a constant. Substituting from the expression for W_{gg} (Eq. 79), at large values of μb

$$c'(\mu_{gg}b_c)^{3/2}e^{-\mu_{gg}b_c}s^{J-1} \sim 1, \quad (86)$$

where c' is another constant. Solving for b_c , we have

$$b_c \approx \frac{J-1}{\mu_{gg}} \log \frac{s}{s_0}. \quad (87)$$

The quantity b_c can be interpreted as the radius of a sharp disk containing a large number of gluons. The total cross section can thus be found

$$\sigma_t = 2\pi b_c^2 = 2\pi \left(\frac{J-1}{\mu_{gg}} \right)^2 \log^2 \frac{s}{s_0}. \quad (88)$$

The parameter J determines the energy behavior by controlling the number of gluons, while μ_{gg} controls the size of the area occupied by the gluons inside the nucleon.

To reproduce the cross section at lower energies, the qq and qg contributions must also be considered. Using toy structure functions $f_q \sim \frac{(1-x)^5}{\sqrt{x}}$ and $f_g \sim \frac{(1-x)^6}{x}$; at high energies we have[45]

$$P_{qq} = W(\mu_{qq}b) \left(\mathcal{A} + \mathcal{B} \frac{m_0}{\sqrt{s}} \right), \quad (89)$$

$$P_{qg} = W(\sqrt{\mu_{qq}\mu_{gg}}b) \left(\mathcal{A}' + \mathcal{B}' \log \frac{s}{m_0^2} \right), \quad (90)$$

where \mathcal{A} , \mathcal{B} , \mathcal{A}' , and \mathcal{B}' are free parameters. To insure correct analyticity properties of the model amplitudes, the substitution $s \rightarrow s e^{-i\pi/2}$ is made everywhere for the even amplitude. As suggested by Regge theory, an asymptotically vanishing odd amplitude is also introduced

$$P_{odd} = W(\mu_{odd}b) \mathcal{A}'' \frac{m_0}{\sqrt{s}} e^{-i\pi/4}, \quad (91)$$

where \mathcal{A}'' is also a free parameter, and the $e^{-i\pi/4}$ factor insures analyticity.

This QCD-inspired eikonal model was fit simultaneously to the world data of σ_t , ρ , and B for pp and $\bar{p}p$ in the energy region 15-1800 GeV. The results are shown in Figs. 45- 47⁸. The six parameter model reproduces the experimental data with a $\chi^2/\text{degree of freedom}$ of 1.59. Although this model predicts a $\log^2 s$ asymptotic rise of the cross section, at the present energies it provides an adequate fit to the world data.

This QCD fit can be used to predict the cross sections at the LHC and SSC supercolliders. At the LHC energy of $\sqrt{s} = 16$ TeV, the cross section is predicted to be 106 ± 4 mb, and at the SSC

⁸The figures in this section are taken from Ref. [49].

Accelerator	\sqrt{s} (TeV)	Lower Bound ($\log s$) (mb)	QCD (Eikonal) (mb)	Upper Bound (Regge) (mb)
LHC	16	104 ± 1	106 ± 4	115
SSC	40	117 ± 1	120 ± 5	135

Table 7: Supercollider cross section predictions

energy of $\sqrt{s} = 40$ TeV, 120 ± 5 mb. The errors are statistical, and are due to the errors of the fitted parameters.

Table 7 lists the predictions, by all three models, of the collider cross sections at the LHC and SSC energies.

6.4 Conclusion

From the E710 results, it can be concluded that:

- The total cross section σ_t and the nuclear slope parameter B rise continually with energy.
- The increasing ratio of the elastic to total cross section, σ_{el}/σ_t , indicates that the nucleon becomes blacker as energy increases.
- The nuclear curvature parameter C is compatible with zero at $\sqrt{s} = 1.8$ TeV. This result along with the positive values measured by the ISR and SppS experiments at lower energies, signal the onset of ‘asymptopia’. Measurements at higher energies are needed in order to confirm the expected negative value of the curvature, and the transformation of the nucleon to a sharp disk.

The E710 results provide a very large lever arm for the three models presented. These three models are quite contradictory, and yet all give good fits to the same data. These fits show that:

- Since the Regge model of the rise of the cross section with energy, given in Eq. 55, violates unitarity, its prediction of the cross section at higher energies provides an upper bound to the predicted cross sections of the future accelerators.
- It is believed that the highest experimental energy thus far attained, the E710 energy of $\sqrt{s} = 1.8$ TeV, is still too low for ‘asymptopia’, and that eventually the cross section may rise more rapidly than the data indicate. Therefore, the $\log(s/s_0)$ behavior of the cross section derived from the analytic asymptotic amplitude analysis should be viewed as a lower bound prediction.
- The QCD eikonal fits are bounded by the other two models.

Appendix A

Theoretical Formulation of Elastic Scattering

We consider elastic $\bar{p}p$ scattering with the initial 4-momenta p_1 and p_2 and the final 4-momenta p_3 and p_4 (Fig. 48). In the center of mass frame, the magnitude of the momentum of each particle

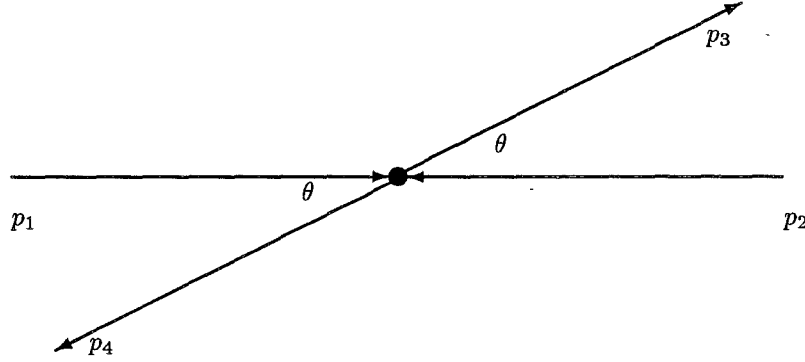


Figure 48: Two-Body Elastic Scattering

is designated as p . The square of the center of mass energy is given by

$$\begin{aligned} s &= (p_1 + p_2)^2 \\ &= 4(p^2 + m^2), \end{aligned} \tag{92}$$

where m is the proton (or anti-proton) mass.

The square of the 4-momentum transfer is

$$\begin{aligned} t &= (p_1 - p_3)^2 \\ &= -4p^2 \sin^2(\theta/2), \end{aligned} \tag{93}$$

where θ is the c. m. scattering angle. For the t values in the range of interest, the scattering angles are small enough to allow the approximation

$$t \approx -p^2 \theta^2. \tag{94}$$

The third Mandelstam variable is u , defined as

$$u = (p_1 - p_4)^2. \quad (95)$$

For the remainder of this formulation, we will use a system of units in which $\hbar=c=1$. Furthermore, in collider experiments where the incoming particles have the same energy and equal but opposite momenta, the center of mass and lab frames are the same.

The differential elastic cross section can be defined in terms of the elastic nuclear scattering amplitude f_n , such that

$$\frac{d\sigma_{el}}{d\Omega} = |f_n|^2, \quad (96)$$

$$\frac{d\sigma_{el}}{dt} = \frac{\pi}{p^2} |f_n|^2, \quad (97)$$

$$\sigma_t = \frac{4\pi}{p} \text{Im} f_n(\theta = 0). \quad (98)$$

where the last relation is the optical theorem. The differential solid angle is $d\Omega$.

At first, we will consider *separately* the effects of a Coulombic or a hadronic field. Later, we will a formulation in which these fields are combined to act simultaneously. For Coulomb scattering, the Lorentz invariant form of the elastic differential cross section is given by

$$\frac{d\sigma_c}{dt} = \frac{\pi}{p^2} \frac{d\sigma_c}{d\Omega} = \pi \left| (\pm) G^2(t) \frac{2\alpha}{|t|} \right|^2. \quad (99)$$

This is the familiar Rutherford result where $-$ and $+$ refer to pp and $\bar{p}p$ systems, respectively. The fine structure constant α is approximately $\frac{1}{137}$. The proton's electromagnetic dipole form factor $G(t)$ is

$$G(t) = \left(1 + \frac{|t|}{\Lambda^2} \right)^{-2}, \quad (100)$$

where $\Lambda^2 = 0.71 \text{ (GeV/c)}^2$.

The nuclear contribution to the differential cross section can be parametrized as

$$\frac{d\sigma_n}{dt} = \frac{d\sigma_n}{dt} \Big|_{t=0} e^{Bt + Ct^2 + \dots} \quad (101)$$

where

$$B \equiv \left(\frac{d}{dt} \log \frac{d\sigma_n}{dt} \right)_{t=0}. \quad (102)$$

B is the nuclear slope parameter. In the t range of interest, the 1st order term Bt dominates the exponent in Eq. 101. Therefore in this formulation, unless specified otherwise, the terms of 2nd and higher order in the nuclear parametrization equation are neglected.⁹

Defining $\rho \equiv \frac{\text{Re}f_n(\theta=0)}{\text{Im}f_n(\theta=0)}$, the differential cross section at $t = 0$ can be written as

$$\begin{aligned} \left. \frac{d\sigma_n}{dt} \right|_{t=0} &= \left. \frac{\pi}{p^2} \frac{d\sigma_n}{d\Omega} \right|_{\theta=0} \\ &= \frac{\pi}{p^2} |\text{Re}f_n(\theta=0) + i \text{Im}f_n(\theta=0)|^2 \\ &= \pi \left| \frac{\rho + i}{p} \text{Im}f_n(\theta=0) \right|^2. \end{aligned} \quad (103)$$

Substituting for $\text{Im}f_n(\theta=0)$ from the optical theorem (Eq. 98),

$$\left. \frac{d\sigma_n}{dt} \right|_{t=0} = \pi \left| \frac{\rho + i}{4\pi} \sigma_t \right|^2, \quad (104)$$

The differential elastic scattering cross section for nuclear scattering is therefore

$$\frac{d\sigma_n}{dt} = \pi \left| \frac{\rho + i}{4\pi} \sigma_t e^{\frac{Bt}{2}} \right|^2. \quad (105)$$

In our formulation, we use the invariant amplitude, f , with the properties

$$\frac{d\sigma_{el}}{dt} = |f|^2. \quad (106)$$

It is therefore convenient to introduce the Coulomb and nuclear $\bar{p}p$ invariant scattering amplitudes,

f_c and f_n :

$$f_c = \frac{2\alpha G^2(t)\sqrt{\pi}}{|t|}, \quad (107)$$

$$f_n = \frac{(\rho + i)\sigma_t e^{\frac{Bt}{2}}}{4\sqrt{\pi}}. \quad (108)$$

⁹The truncation of the polynomial in t in the exponent of Eq. 101 after the first order term is allowed at low $|t|$, and as E710 demonstrated, at *all* t at the Tevatron energy of 1.8 TeV.

The invariant differential cross sections can then be expressed as

$$\frac{d\sigma_c}{dt} = |f_c|^2, \quad (109)$$

$$\frac{d\sigma_n}{dt} = |f_n|^2. \quad (110)$$

Each of the above expressions is valid in the presence of its respective field *only*. If the nuclear and Coulomb fields are both present, however, we cannot simply superimpose the two amplitudes. A phase factor $\alpha\phi(t)$ must be introduced into the Coulomb amplitude such that the complete elastic differential cross section is given by

$$\frac{d\sigma_{el}}{dt}(t) = \left| f_c e^{i\alpha\phi(t)} + f_n \right|^2. \quad (111)$$

This phase factor reflects the distortion of the pure amplitudes f_c and f_n due to the simultaneous presence of both hadronic and Coulombic scattering. In the language of Feynman diagrams, f_c corresponds to the sum of all diagrams in which only photons are present and f_n to the sum of all diagrams in which only hadronic exchanges are present. When both fields are present, however, there are new diagrams possible which have both kinds of exchanges present. This gives rise to the phase $\alpha\phi(t)$. This phase was first investigated by Bethe[28] and later by West and Yennie[30], using a QED calculation of Feynman diagrams. It was recalculated by Cahn[31], using an eikonal approach, with the result

$$\phi(t) = (\mp) \left[\gamma + \log \left(\frac{B|t|}{2} \right) + \log \left(1 + \frac{8}{B\Lambda^2} \right) + \left(\frac{4|t|}{\Lambda^2} \right) \log \left(\frac{4|t|}{\Lambda^2} \right) + \frac{2|t|}{\Lambda^2} \right], \quad (112)$$

where $\gamma = 0.577$ is Euler's constant. The upper sign is for pp and the lower sign for $\bar{p}p$. Over the t range of interest, $\phi(t)$ varies very slowly and is about 2, and $\alpha\phi \ll 1$, so the differential elastic cross section can be written as

$$\frac{d\sigma_{el}}{dt}(t) = \pi \left[\left(\frac{2\alpha}{|t|} \right)^2 G^4(t) \mp (\rho + \alpha\phi) \frac{\alpha\sigma_t}{\pi} \frac{G^2(t)}{|t|} e^{\frac{Bt}{2}} + \left(\frac{\sigma_t}{4\pi} \right)^2 (1 + \rho^2) e^{Bt} \right]. \quad (113)$$

Again, the $-$ and $+$ refer to pp and $\bar{p}p$ systems, respectively.

The second term of the summation is known as the interference term and assumes its largest weight relative to the other two terms when $|f_c| = |f_n|$, i.e., when $d\sigma_c/dt = d\sigma_n/dt$. If $\rho + \alpha\phi$ is positive, the interference is destructive for pp and constructive for $\bar{p}p$. A typical value for $|\alpha\phi|$ is ≈ 0.02 . This interference term allows the measurement of the quantity $\rho + \alpha\phi$, and hence the determination of ρ . The t value at which interference is maximum, i.e., when $|f_c| = |f_n|$, is given in $(\text{GeV}/c)^2$ by

$$\begin{aligned} |t|_{int} &\approx \frac{8\pi\alpha}{\sigma_t} \\ &= \frac{0.071}{\sigma_t(\text{mb})} \\ &= (p\theta_{int})^2, \end{aligned} \tag{114}$$

where θ_{int} is the interference angle.

The first term of the summation dominates in the Coulomb region where $|t| \ll |t|_{int}$ and $d\sigma_{el}/dt$ goes nearly as $1/t^2$. It is independent of the σ_t , B , and ρ , and can be used to normalize the experimental data.

The third term dominates in the nuclear region where $|t| \gg |t|_{int}$ and $d\sigma_{el}/dt$ goes nearly as e^{Bt} . It is the main term that determines B .

Table 8 gives $|t|_{int}$ and θ_{int} values for the existing $\bar{p}p$ colliders and their c.m. energies. Experiment E710 at the Tevatron attained a maximum energy of $\sqrt{s} = 1.8$ TeV. At this energy, $|t|_{int} \approx 0.00098$ $(\text{GeV}/c)^2$. As we shall see, this is very close to the minimum value, $|t|_{min} = 0.00075$ $(\text{GeV}/c)^2$, covered by the detectors of this experiment. The interference angle for this experiment was $\theta_{int} = 0.035$ mrad, i.e., a very small angle. At a distance of 80 m from the interaction region, it corresponds to a transverse displacement of only 2.8 mm. This demonstrates the primary challenge of this experiment: To penetrate into the Coulomb interference region, one needs to probe very close to the beam. This experimental problem is bound to be even more severe for the proposed SSC experiments that are to be conducted at $\sqrt{s} = 40$ TeV, where θ_{int} is only about 0.001 mrad.

\sqrt{s} (GeV)	Accelerator	$ t _{int} \left((\text{GeV}/c)^2 \right)$	θ_{int} (mrad)
23.5	ISR	0.0017	3.6
30.7	ISR	0.0017	2.7
52.8	ISR	0.0016	1.5
62.5	ISR	0.0016	1.3
540	SPS	0.0011	0.120
1800	Tevatron	0.00098	0.035
40000	SSC	0.00059	0.00122

Table 8: Values of $|t|_{int}$ and θ_{int} for $\bar{p}p$ elastic scattering

The total elastic cross section σ_{el} is defined as $\int_{-\infty}^0 (d\sigma_n/dt)dt$, where $d\sigma_n/dt$, the nuclear differential cross section, is the square of the nuclear invariant amplitude (Eq. 108). Performing the integration, we obtain

$$\sigma_{el} = \frac{\sigma_t^2 (1 + \rho^2)}{16\pi B}. \quad (115)$$

This result will be given the special name Σ_{el} . It is the same as σ_{el} if, in the nuclear parametrization equation (Eq. 101), the coefficients of terms of second (Ct^2) and higher orders are negligible compared to the first (Bt) order for *all* t values. The ratio of the elastic to total cross section is given as

$$\frac{\Sigma_{el}}{\sigma_t} = \frac{\sigma_t (1 + \rho^2)}{16\pi B}. \quad (116)$$

The total elastic cross section is useful in correlating the asymptotic rise of σ_t with B since σ_{el}/σ_t must be less than unity. Therefore, a model that predicts σ_t to rise with s at a certain rate must predict at least as rapid a rise for B .

Appendix B

The Beam Lattice

In an accelerator lattice, equations of motion for a charged particle can be written in the following manner:

$$\eta = A(z) \sin[\psi(z) + \phi], \quad (117)$$

$$\eta' = A'(z) \sin[\psi(z) + \phi] + A(z) \psi' \cos[\psi(z) + \phi], \quad (118)$$

where

z is the beam path position,

η is the horizontal or vertical component of displacement from the beam direction,

the primed quantities are derivatives with respect to z , i.e., $\eta' = d\eta/dz$,

$\phi' = d\phi/dz$, etc.,

$A(z)$ is the amplitude of the displacement at z ,

ϕ is a constant phase,

$\psi(z)$ is a periodic phase function dependent on the lattice frequency of particles in the machine[40].

Eqs. 117 and 118 can be manipulated to yield

$$A^2 \psi' = \gamma \eta^2 + 2\alpha \eta \eta' + \beta \eta'^2. \quad (119)$$

Eq. 119 describes an ellipse of area $\frac{\pi A^2 \psi'}{\sqrt{\gamma \beta - \alpha^2}} = \pi A^2 \psi'$, where $\alpha = -A'/A\psi'$, $\beta = 1/\psi'$, and $\gamma = A'^2/A^2\psi' + \psi'$.

Before any displacement, the transverse and longitudinal coordinates of a particle can be identified as (η_0, z_0) , and the equations of motion are:

$$\eta_0 = A_0 \sin \phi, \quad (120)$$

$$\eta'_0 = A'_0 \sin \phi + A_0 \psi'_0 \cos \phi. \quad (121)$$

Solving for $\sin \phi$ and $\cos \phi$ in terms of η_0 and η'_0 , Eqs. 117 and 118 can be written in the form

$$\begin{pmatrix} \eta \\ \eta' \end{pmatrix} = \begin{pmatrix} m_{11} & m_{12} \\ m_{21} & m_{22} \end{pmatrix} \begin{pmatrix} \eta_0 \\ \eta'_0 \end{pmatrix}. \quad (122)$$

The matrix elements m_{ij} can be shown to be

$$m_{11} = (\beta/\beta_0)^{1/2} [\cos \psi(z) + \alpha_0 \sin \psi(z)], \quad (123)$$

$$m_{12} = (\beta\beta_0)^{1/2} \sin \psi(z), \quad (124)$$

$$m_{21} = (\beta\beta_0)^{-1/2} [(\alpha_0 - \alpha) \cos \psi(z) - (1 + \alpha\alpha_0) \sin \psi(z)], \quad (125)$$

$$m_{22} = (\beta_0/\beta)^{1/2} [\cos \psi(z) - \alpha \sin \psi(z)]. \quad (126)$$

The quantity m_{11} can be thought of as a focusing factor along the η axis, and m_{12} can be thought of as the effective length along the z axis.

Appendix C

Drift Chamber Operation and Control

As mentioned earlier, the drift chambers used for elastic scattering measurements were housed in roman pots, two pots per castle, one above and one below the beam line. The pots could

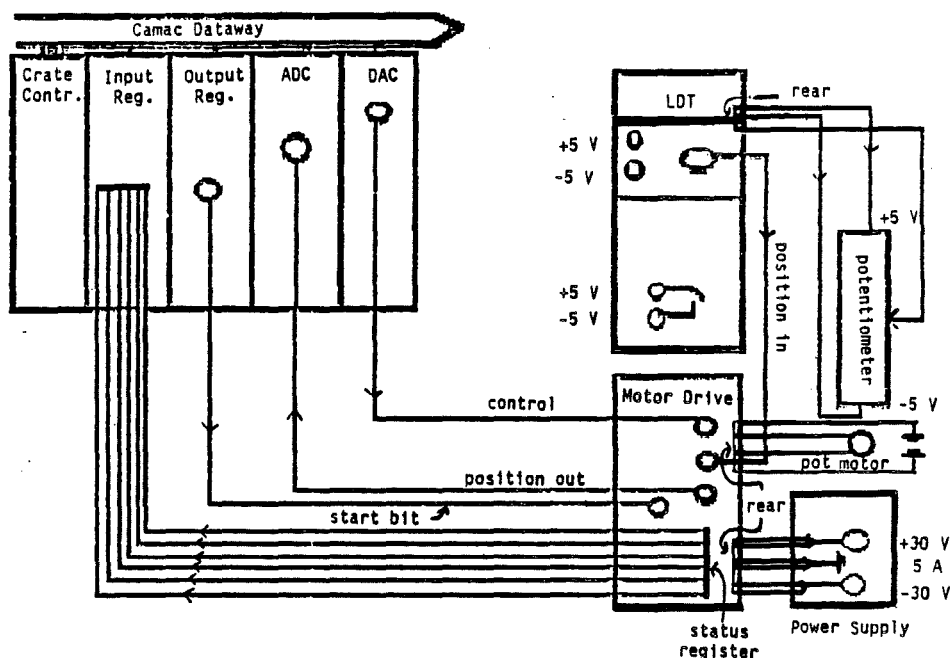


Figure 49: Schematic of the pot movement system

be moved remotely by a potentiometer motor tied by a belt to the spring upon which the pots rested. A motor drive unit[37] and a Linear Drive Transducer (L.D.T.) allowed computer-controlled motion of the pots. The motor drive unit and the L.D.T. interfaced the Camac dataway with the potentiometer motor. A digital number sent from the computer via the Camac dataway to a 12 bit, 16 channel, NEL type 9091 multiDAC triggered the DAC to send a potential voltage through a motor drive unit to the 10 V range pot potentiometer motor, thus allowing movement of the pot

to the desired location. Fig. 49 is a schematic of the pot movement system.

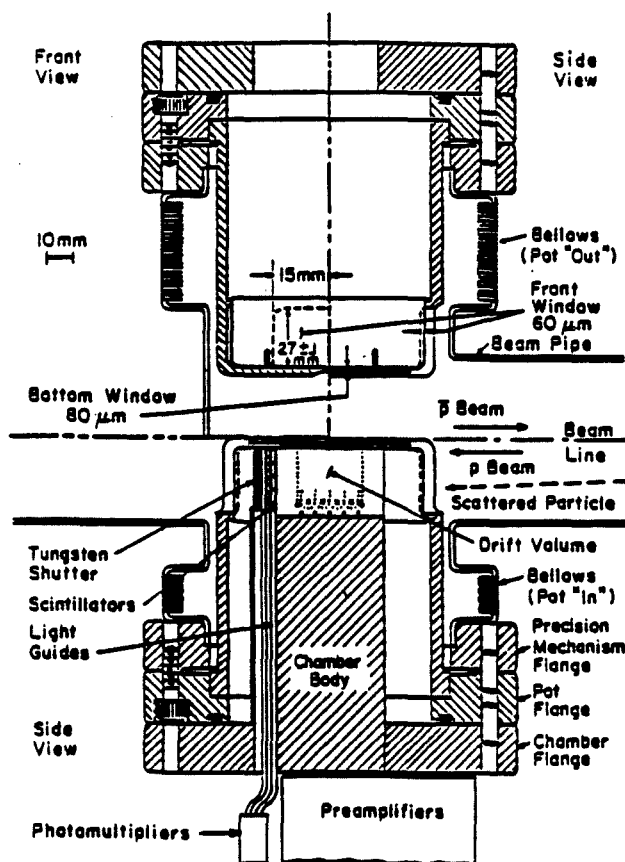


Figure 50: Front and side views of drift chambers inside their castle

The pots had a 24 mm distance in which to move vertically toward and away from the beam. The active area of each chamber was about 1.950 mm above the bottom of each roman pot, which could reach within 100 microns of the center of the castle (see Fig. 50)[35]. The pot potentiometer position was read with a Borer dual-slope 1241 ADC whose input was the analog signal produced by the 10 V range L.D.T.

The motor drive unit provided six bits of status information about the pot. This information was then sent to a DSP dual I/O 612 register and fed into the computer for on-line monitoring of the pots. The motor drive unit set one bit if the pot were at a limit switch, another if the pot were

moving, another if the pot reached its designated position, another as an alarm if the pot could not reach its designated position within a specified time limit, and another was used as a calibration bit.

The DAC and ADC used for the pot movement each had a resolution of 1 count per 2.44 mV. Each pot potentiometer was calibrated at about 0.4 V/mm, corresponding to an accuracy of ± 6 microns in pot location. The potentiometer calibration itself was done by surveyors to an accuracy of 0.1%. A straight line was fit to the ADC mV per bit calibration, with an error of 0.4%. Therefore, the error in the remote positioning of the pot by 1 mm from its base near the castle center was ± 5 microns. The pot offset from the castle center was measured by surveyors with an error of 20 microns, except for the pots 7 and 8 which had an error of 100 microns. Table 9 lists the calibration constants for the DAC and ADC channels associated with each pot, along with each pot's potentiometer calibration distance and each pot's base position offset with respect to the center of the castle.

Pot	Potentiometer Cal. Constant (V/mm)	Offset from Castle Center (mm)	DAC Cal. Constant (mV/bit)	ADC Cal. Constant (mV/bit)
LUO	0.3984	0.199	2.440	2.440
LDO	0.3952	0.199	2.440	2.440
ILU	0.3955	0.211	2.440	2.440
ILD	0.4003	0.211	2.440	2.440
IRU	0.3951	0.085	2.440	2.440
IRD	0.4072	0.085	2.440	2.440
RUO	0.3960	0.349	2.440	2.440
RDO	0.3931	0.349	2.440	2.440

Table 9: Calibration constants for pot position measurements

Appendix D

Data Acquisition

D.1 The Trigger System

The stored beams in the Tevatron were divided into six bunches. A radio frequency (RF) system, located at the F0 intersection region, kept the p and \bar{p} bunches confined inside guiding buckets. There were 1113 RF buckets along the circumference of the Tevatron. Of these, only twelve were populated with particles, six for each species. The relative positions of the six counter-rotating bunches were such that collisions occurred at the designated interaction points. The time of the interactions was determined by using signals from the guiding RF clock which were received over the accelerator local area network (ACNET). A gate was thus constructed, with the duration of a few ns, and centered on the arrival time of the interaction products to the location of the counters. The triggers were constructed from the coincidences of counters firing while the gate was open. Such a coincidence was defined as an in-time hit.

The event trigger types used in this experiment fall into nine categories. They are listed below, along with a brief definition of each type:

OO: One out of two hit trigger counters in any outer chamber on one side ANDed with that on the other side (for small angle elastic scattering).

II: One out of two hit trigger counters in any inner chamber on one side ANDed with that on the other side (for large angle elastic scattering).

OI: One out of two hit trigger counters in any outer chamber on one side ANDed with that of an inner chamber on the other side (for any inelastic scattering).

LR: Any hit ring counter on the left side ANDed with that on the right side (for double arm inelastic and diffractive scattering).

L: Left side OR of any ring counter hit (for single arm inelastic and diffractive scattering).

R: Right side OR of any ring counter hit (for single arm inelastic and diffractive scattering).

C: OR of any central counter hit (for any inelastic scattering).

I: One out of two hit trigger counters in any inner chamber (for any inelastic scattering where an inner chamber was hit).

O: One out of two hit trigger counters in any outer chamber (for any inelastic scattering where an outer chamber was hit).

As mentioned in Section 3.2, there were two sets of detectors used for the detection of the elastic and inelastic events. The inner and outer drift chambers were used for the detection of the elastic events, as well as beam halo background. The rest of the system, i.e., the ring and central scintillation counters, were used for detecting the inelastic events.

D.1.1 The Elastic Trigger

For each drift chamber, its corresponding trigger counters (see Section 3.3.2) were used to trigger its readout.

To obtain the signals from the trigger and calibration counters, Phillips XP1911 10-stage photomultiplier tubes were used. Signals from the trigger counters were sent to a 30 ns coincidence gate with the RF signal. For triggering, the coincidence between any of the two trigger counters in a left side detector and any of the two trigger counters in a right side detector were used. This event trigger, referred to as outer-outer or OO, was the trigger used for all of the elastic scattering events that made up the data analyzed in this work.

The signal from the drift chambers was digitized by 4-D modules[38]. Each datum word read by the data acquisition system consisted of 16 bits. The last of these 16 bits was a status bit. The remaining 15 consisted of 6 low bits for the x and 9 higher bits for the y coordinates of the charged

particle incident on the chamber. The RAM memory of the 4-D unit accepted data from the ADC and encoder every 40 ns, thus allowing the last 640 ns of information (16 data words) to be stored and read out by the data acquisition system. A new trigger would erase the memory and allow the process to start over.

The coordinates of the incident particle were read according to the following mechanisms:

- *The x readout:* A charged particle incident on a drift chamber produced charges at each end of the sense wires. These charges were sent, individually, through preamplifiers into a 50 MHz flash ADC which measured the difference in the proportional voltage of each current. This produced a charge division signal proportional to the x component of the location of the incident particle. This signal was digitized into 64 bins, where each bin corresponded to approximately 0.5 mm.
- *The y readout:* The discriminated signal of the sum of the two charges at wire ends produced a drift time signal. A priority encoder's clock started counting when a trigger was input to the 4-D unit, and stopped with the drift time pulse, thus producing the 9 bit drift time readout. This signal was digitized into 512 bins, where each bin corresponded to about 65 microns.

D.1.2 The Inelastic Trigger

To obtain the signals from the ring and central scintillation counters, Phillips XP2262 12-stage photomultiplier tubes were used. The main inelastic trigger was constructed from the coincidence of any of the twelve counters in rings L3, L4, and L5 with any of the twelve counters in the rings R3, R4, and R5. The signals from the counters of each side were put in an OR and then in coincidence with the RF signal. Most of the non single diffractive events were recognized from this trigger, which was also referred to as left-right, or LR.

Another inelastic trigger was made by an OR of the eight central counters with the twenty from rings L0, L1, L2, R1, and R2. This was not used as an active trigger, but was occasionally used as a veto.

D.1.3 The Master Trigger

The number of inelastic collisions was so high that it was not practical to read every one of them on to data tape. Instead, the number of inelastic triggers was prescaled by a factor which was decided on empirically from observation of these triggers, ranging from 2 to 500. This prescaling was *not* done for the elastic triggers, however, due to the low machine luminosity and signal-to-noise ratio (see Section 4.6). The grand OR of the prescaled triggers made up the master trigger, which in turn initiated the readout of the timing and pulse height of the scintillation counters, the 4-D modules, etc. Fig. 51 is a block diagram of the master trigger logic.[36].

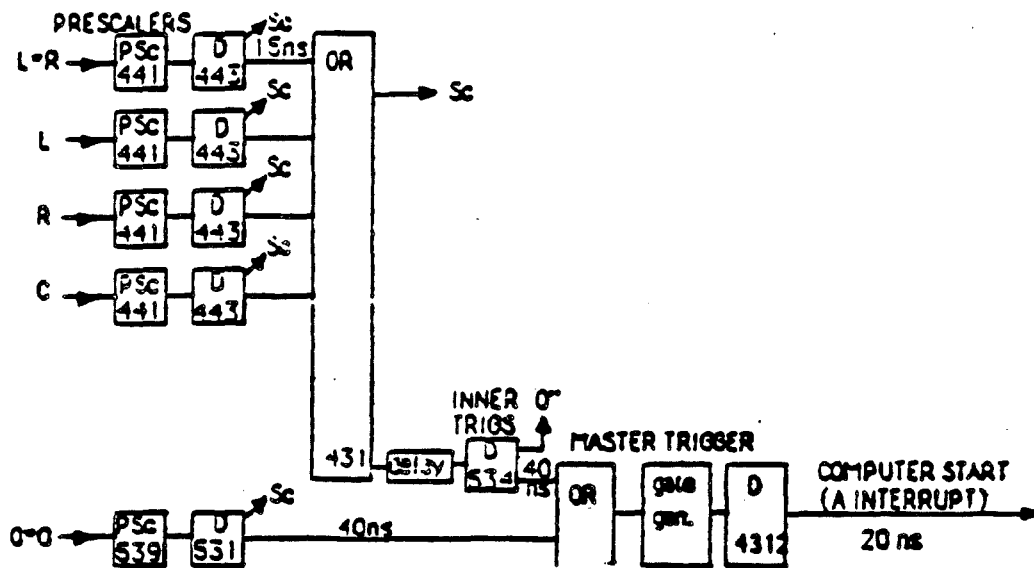


Figure 51: The master trigger logic

D.2 On-line Data Analysis

Data acquisition and on-line analysis was done with a DEC PDP 11/34 computer. The operating system used was RT version 5.3, issued by DEC, Inc. The data acquisition program was a modified version of RT-Multi, a system developed at Fermilab[54]. The processed data was stored on magnetic tape. The processor could be accessed interactively by a Decwriter II hardcopy terminal, two VT240 terminals, and two serially connected PC/ATs. A port selector allowed access to the Fermilab VAX cluster as well as a MicroVax II running under the VMS 5.0 operating system. The primary purpose of the MicroVax was to allow access to ACNET. It was later used for part of the off-line data analysis.

As mentioned in Section D.1.3, the master trigger initiated the data collection cycle. A NIM pulse was sent from the logic to the Bison interface box[55]. The Bison box interrupted the PDP, and the RT-Multi routine began executing a pre-defined Camac definition list. Data from a set of Camac crates were then sequentially transferred, through a Jorway branch bus, to the data buffer. Each event buffer contained the following information:

- The ADCs of the 52 ring and central scintillation counters and the 24 trigger and calibration counters of the drift chambers,
- The TDCs of the above counters, as well as those of the chambers from the tracking telescopes.
- The scaler values. The scalers were a set of numbers that included the integrated single rates read from all of the ring and central counters, as well as those from the trigger counters. An example of the scaler readouts for a typical run is displayed below:

SCALERS FOR RUN 623

<i>L1</i>	3874349.	<i>L2</i>	4147832.	<i>L3</i>	12287859.	<i>L4</i>	10303276.
<i>L5</i>	4927250.	<i>L2 - 5</i>	9099065.	<i>L</i>	765798.	<i>L PRE</i>	957.
<i>R1</i>	4361079.	<i>R2</i>	5102984.	<i>R3</i>	6073593.	<i>R4</i>	4490484.
<i>R5</i>	7317536.	<i>R2 - 5</i>	16449130.	<i>R</i>	319085.	<i>R PRE</i>	639.
<i>C1 - 8</i>	13077251.	<i>C</i>	692014.	<i>C PRE</i>	692.	<i>LCR</i>	1495072.
<i>LCRI</i>	2419862.	<i>LR</i>	28111.	<i>LR PRE</i>	703.		0.
<i>L I 1 - 6</i>	11141783.	<i>L I</i>	721370.	<i>R I 1 - 6</i>	8982744.	<i>R I</i>	380282.
<i>I</i>	1097892.	<i>II</i>	3760.	<i>II PRE</i>	0.		0.
<i>IE</i>	173102.	<i>IE PRE</i>	0.	<i>L O 1 - 6</i>	3095425.	<i>L O</i>	5469706.
<i>R O 1 - 6</i>	3499423.	<i>R O</i>	3373514.	<i>O</i>	5469706.		0.
<i>OO</i>	39146.	<i>OO PRE</i>	39146.	<i>OE</i>	5469706.	<i>OE PRE</i>	6077.
<i>OI</i>	11637.	<i>OI PRE</i>	0.	<i>INTRIGS</i>	2985.	<i>MASTER</i>	48173.
<i>CLOCK</i>	2963.	<i>CLOCK G</i>	2460.	<i>L5*</i>	219028.	<i>L5 * RF</i>	144871.
<i>L5 *</i>	144792.	<i>R5*</i>	222383.	<i>R5 * RF</i>	52766.	<i>M(G)</i>	3630.
<i>M"(G)</i>	17.	<i>LR*</i>	377232.	<i>LR *</i>	377004.	<i>L21R</i>	166.

- The output of the 4-D modules (See Section D.1.1).

After the buffer sent its contents to the tape drive, it was cleared and set for the arrival of the next event. The maximum rate of data transfer to tape was 220 events/sec. Fig. 52 is a block diagram of the on-line data acquisition system.

In addition to the above itemized parameters, another set of parameters that were *not* event-dependent were read on to the data tape at the beginning of each run. They consisted of the following:

- The pot positions, which were controlled by a Camac crate with a Borel dual slope ADC. In addition to being recorded at the beginning of each run, they were accessible interactively during data taking.

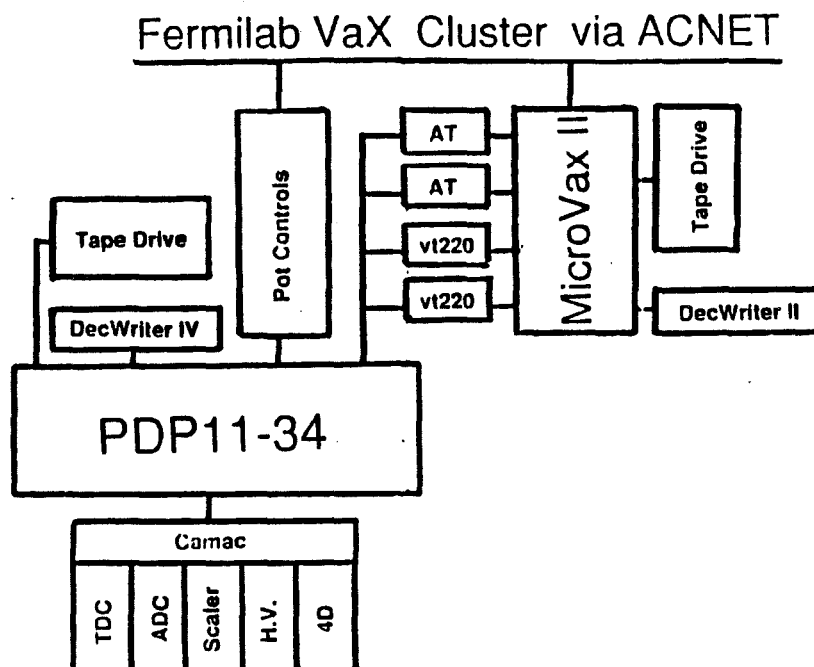


Figure 52: Block diagram of on-line data acquisition system

- The values of the high voltages for the field and sense wires in all drift chambers and all scintillation counters, which were monitored from five ADC modules.
- A set of accelerator-related parameters. This included information about the intensity of the beams, their emittances, the luminosity values at various intersection regions, the positions of the steel yokes of the Lambertson magnets, and the gas pressure inside the beam pipe. This information was transmitted to the MicroVax over ACNET and was recorded on tape.

Appendix E

Derivation of Readout Calibration Functions

E.1 The Calibration Counter Edge

If the resolution of the detectors were indeed infinite, the observed distribution at the edge of the slit at the bottom of the calibration counter would be a step function:

$$E'(y) = N_e \Theta(y - p), \quad (127)$$

where

y is the electronic bit number identifying the vertical coordinate of the particle incident on the detector,

$E'(y)$ is the normalized distribution of data at a given bit y ,

N_e is the normalization constant of the function,

p is the bit number corresponding to the edge of the calibration counter ,

Θ is a step function.

Since the resolution is finite, however, $E'(y)$ is convoluted with a gaussian dispersion function to yield a new expression $E(y)$:

$$E(y) = \int_{-\infty}^{\infty} E'(y') \frac{1}{\sqrt{2\pi\sigma/c}} e^{-\frac{1}{2(\sigma/c)^2}(y-y')^2} dy'. \quad (128)$$

Here, σ is the width, in mm, of the gaussian representing the resolution of the detector, and c is the physical dimension corresponding to each bit (commonly referred to as the mm/bit constant). σ/c is the resolution in bits, and will be referred to as Σ .

Substituting Eq. 127 into Eq. 128 and simplifying, we get

$$\begin{aligned} E(y) &= \frac{N_e}{\sqrt{2\pi}\Sigma} \int_{-\infty}^{\infty} \Theta(y' - p) e^{-\frac{1}{2\Sigma^2}(y-y')^2} dy' \\ &= \frac{N_e}{\sqrt{2\pi}\Sigma} \int_p^{\infty} e^{-\frac{1}{2\Sigma^2}(y-y')^2} dy'. \end{aligned}$$

Making the variable substitution $t = \frac{1}{2\Sigma^2}(y - y')^2$ and performing some simple algebra yields:

$$\begin{aligned} E(y) &= \frac{N_e}{2} \times \frac{2}{\sqrt{\pi}} \int_{\frac{p-y}{\sqrt{2}\Sigma}}^{\infty} e^{-t^2} dt \\ &= \frac{N_e}{2} \operatorname{erfc} \left(\frac{p-y}{\sqrt{2}\Sigma} \right) \\ &= \frac{N_e}{2} \left[1 + \operatorname{erf} \left(\frac{y-p}{\sqrt{2}\Sigma} \right) \right]. \end{aligned} \tag{129}$$

Substituting the expression for Σ into Eq. 129, the function describing the data at the horizontal edge of the calibration counter is:

$$E(y) = \frac{N_e}{2} \left[1 + \operatorname{erf} \left(\frac{(y-p)c}{\sqrt{2}\sigma} \right) \right]. \tag{130}$$

E.2 The Calibration Counter Hole

If the detector resolution were infinite, the profile of the particles going through the holes would be circular, with the maximum flux occurring at the center of the hole, and then radially decreasing to zero toward its perimeter. The observed distribution could be described by

$$\begin{aligned} I'(y) &= N_h \sqrt{1 - \left[\frac{(y-p)c - \mu}{r} \right]^2}, \text{ for } |(y-p)c - \mu| \leq r, \\ &= 0, \text{ for } |(y-p)c - \mu| > r, \end{aligned} \tag{131}$$

where

$I'(y)$ is the normalized distribution of data at a given bit y ,

N_h is the normalization constant of the function,

μ is the location of the hole, in mm, with respect to the edge of the calibration

counter,

r is the radius of the hole ($r=0.09$ mm).

Since the resolution is finite, $I'(y)$ is convoluted with the same gaussian dispersion function that was used for the edge, to yield a new expression $I(y)$:

$$\begin{aligned}
 I(y) &= \int_{-\infty}^{\infty} I'(Y') \frac{1}{\sqrt{2\pi}\sigma} e^{-\frac{1}{2\sigma^2}[(y-p)c-\mu-Y']^2} dY' \\
 &= \frac{N_h}{\sqrt{2\pi}\sigma} \int_{-r}^r dY' e^{-\frac{1}{2\sigma^2}[(y-p)c-\mu-Y']^2} \sqrt{1 - \left(\frac{Y'}{r}\right)^2}, \quad (132)
 \end{aligned}$$

Appendix F

Evaluation of the Fitting Function

As mentioned briefly in Section 2.2, each experimental bin covers a range of t values. The differential cross section that is to be fitted to the data must therefore be averaged over the size of the bin. This averaging is done by integrating the differential cross section over the bin, and then dividing it by the area of the bin. In this section, we will first briefly discuss the numerical integration schemes used, and then proceed to develop the expression for the *effective* elastic differential cross section which is fitted to the data.

F.1 Numerical Integration Techniques

The integrals were evaluated numerically by gaussian quadrature techniques[42]. These techniques use orthogonal polynomials, where the n th term of such polynomials is designated the symbol $p_n(x)$. Orthogonality means that any two terms of the polynomial satisfy the condition

$$\int_a^b p_i(x)p_j(x)w(x)dx = h_i\delta_{ij}, \quad (133)$$

where δ_{ij} is the Kronecker delta function, and $h_i = \int_a^b [p_i(x)]^2 w(x) dx$, with $w(x)$ as a weight function.

The polynomial term $p_n(x)$ has n real zeros in the interval $[a, b]$ and $p_{n+1}(x)$ has $n + 1$ zeros, interlaced with those of the n th order. The polynomials are evaluated recursively, using a two term recursion relation

$$p_{n+1}(x) = (\gamma_n x - \alpha_n)p_n(x) - \beta_n p_{n-1}(x), \quad n = 0, 1, 2, 3, \dots, \quad p_0(x) = 1, \quad p_{-1}(x) = 0. \quad (134)$$

The weight function $w(x)$ along with the limits of integration $[a, b]$, determine the type of polynomial to be used. As will be shown in Section F.2, the integration in y' is over finite limits,

and therefore a Legendre polynomial was used. Integration over infinite boundaries, such as the one in x' , are done using Hermite polynomials.

Legendre polynomials $y = P_n(x)$ satisfy the differential equation

$$(1 - x^2) \frac{d^2 y}{dx^2} - 2x \frac{dy}{dx} + n(n+1)y = 0. \quad (135)$$

The derivative satisfies the relation

$$(1 - x^2) \frac{dP_n}{dx}(x) = -nP_n(x) + nP_{n-1}(x). \quad (136)$$

The recursion relation for Legendre polynomials is

$$\begin{aligned} P_0(x) &= 1, \\ P_{-1}(x) &= 0, \\ (n+1)P_{n+1}(x) &= (2n+1)xP_n(x) - nP_{n-1}(x), \end{aligned} \quad (137)$$

with the normalization

$$\int_{-1}^1 P_n(x)P_m(x)w(x)dx = \frac{2}{2n+1}\delta_{mn}, \quad (138)$$

where $w(x) = 1$. The integration in Eq. 138 is in the interval $[-1, 1]$. A simple linear transformation allowed these polynomials to be used with non-unity limits $[y'_{min}, y'_{max}]$.

Hermite polynomials $y = H_n(x)$ satisfy the differential equation

$$\frac{d^2 y}{dx^2} - 2x \frac{dy}{dx} + 2ny = 0. \quad (139)$$

The derivatives satisfy the relation

$$\frac{dH_n}{dx}(x) = 2nH_{n-1}(x). \quad (140)$$

The recursion relation is

$$H_0(x) = 1,$$

$$\begin{aligned}
H_{-1}(x) &= 0, \\
H_{n+1}(x) &= 2xH_n(x) - 2nH_{n-1}(x),
\end{aligned} \tag{141}$$

with the normalization

$$\int_{-\infty}^{\infty} H_n(x)H_m(x)w(x)dx = \sqrt{\pi}2^n n! \delta_{mn}, \tag{142}$$

where $w(x) = e^{-x^2}$.

F.2 The Effective Differential Elastic Cross Section

The differential elastic cross section $\frac{d\sigma_{el}}{dt}$ is given in Eq. 113. Due to the width of the elastic pattern, the correct form of this differential cross section is expressed by convoluting it with the two-dimensional gaussian representing the pattern dispersion. As a reminder, small scattering angle allows the approximation $t = -p^2\theta^2$, where the components of θ are defined in terms of the left and right side coordinates according to Eqs. 45 and 46. The new *pattern corrected* elastic differential cross section is

$$\left. \frac{d\sigma_{el}}{dt} \right|_{corr} = \int_{-\infty}^{\infty} \int_{y'_{min}}^{y'_{max}} \frac{d\sigma_{el}}{dt} \frac{e^{-\frac{1}{2}(\frac{x-x'}{\sigma_x})^2}}{\sqrt{2\pi}\sigma_x} \frac{e^{-\frac{1}{2}(\frac{y-y'}{\sigma_y})^2}}{\sqrt{2\pi}\sigma_y} dy' dx', \tag{143}$$

where the limits of integration in y' are the boundaries of the right side chamber. In x , both chambers are 28 mm wide in physical space. In scaled space, however, the right side detector is $\frac{L_x}{L_{x'}} = \frac{45.6 \text{ m}}{30.0 \text{ m}} = 1.52$ times wider than the left side chamber. This means that in the frame of the left side chamber, the right side detector is $28 \times 1.52 = 42.6$ mm wide, leaving a space of more than 7 mm on each vertical side of the right side detector that is not covered by the left side chamber. Since the x component σ_x of the pattern width was about 2 mm, this 7 mm clearance was large enough to prevent any significant pattern loss at the vertical edges of the left side detector, and therefore the limits of integration in x' were approximated as infinities.

At any given point (x, y) on the left side detector, the ratio of this pattern-convoluted function

to what the differential cross section would have been without the pattern effect was calculated as a weight factor $W(x, y)$ such that

$$W(x, y) = \frac{\left. \frac{d\sigma_{el}}{dt} \right|_{corr}}{\left. \frac{d\sigma_{el}}{dt} \right|}. \quad (144)$$

The significance of this weight factor will be clarified shortly.

Since the measured number of counts, ΔN , belongs to a cell of 28 mm width and 0.5 or 1 mm height, the elastic differential cross section given in Eq. 113 was averaged over this cell. But to account for pattern loss, the average was weighted by the weight function $W(x, y)$ given in Eq. 144. for stack i

$$\left\langle \frac{d\sigma_{el}}{dt} \right\rangle_i = \frac{1}{\Delta x \Delta y} \int_{-\frac{\Delta x}{2}}^{\frac{\Delta x}{2}} \int_{y_{min_i}}^{y_{min_i} + \Delta y} \frac{d\sigma_{el}}{dt} W(x, y) dy dx. \quad (145)$$

Here, the scattering angle is determined by the left side coordinates (x, y) of the scattered particle, i.e., $t = -p^2 \left[\left(\frac{x}{L_x} \right)^2 + \left(\frac{y}{L_y} \right)^2 \right]$. The integrals of Eq. 145 are both over finite limits and were therefore evaluated by Legendre polynomials. The weights $W(x, y)$ were evaluated at the *same* positions as the zeros of the Legendre polynomials over the specified x and y intervals.

Advantage was taken of a few fine points in order to drastically cut down on computing time:

- The $W(x, y)$ values were evaluated for points whose y coordinates were as far as $4\sigma_y$ from the bottom of the chamber. For points higher than that, the weight values were not expected to depend appreciably on y , and were therefore not calculated. Instead, the same horizontal series of values were used all the way to the top of the chamber.
- The corrections were performed to account for the pattern loss at the low $|t|$ edge *only*. The small statistics at the high $|t|$ edge, as well as the absence of any Coulomb information, made the use of pattern corrections for those regions unfeasible. Instead, the three highest edge stacks were simply not used, with no appreciable effect on the final result.
- Use was made of the symmetry between the regions $-\frac{\Delta x}{2} \leq x \leq 0$ and $0 \leq x \leq \frac{\Delta x}{2}$. The

integration in x was therefore performed over the latter interval only, and the result was doubled.

A stability study was conducted to determine the number of points for each integration. A minimum number of points were used to yield stability of each integral to 1 part in 1000. For the Hermite integration in x' , this minimum number was 4 for data at $\sqrt{s}=1.8$ TeV, and 9 for data at $\sqrt{s}=1.0$ TeV. For all data, 8 Legendre points were needed to perform the integration in y' , 16 for x , and 4 for y .

Appendix G

Error Analysis

The measured quantity in this experiment was the number of counts. Therefore, all errors were based on the premise that the uncertainty of the measured number of counts in a bin is the square root of that number. The differential counts $\frac{dN}{dt}$ which were fitted were *not* directly measured, however, since they were background-subtracted, and background was a calculated quantity *based* on measured quantities.

The differential number of counts dN in each stack was obtained according to $dN = dN_{s+n} - dN_n$, where dN_{s+n} is the measured signal+noise count, and dN_n is the calculated background. The statistical error of dN_{s+n} is simply $\sqrt{dN_{s+n}}$. The statistical error of dN_n is found from Eq. 37, and is the quadrature sum of the statistical errors of the background normalization constant C , and the normalized background content P of that stack obtained from the background sample. The statistical error of P is in turn found from Eq. 38. Rewriting this equation in simpler form, we have, for stack i

$$P_i = \frac{N_i}{N_{tot}}. \quad (146)$$

The statistical error of P_i can then be calculated according to

$$\begin{aligned} \delta P_i &= P_i \sqrt{\left(\frac{\delta N_i}{N_i}\right)^2 + \left(\frac{\delta N_{tot}}{N_{tot}}\right)^2} \\ &= P_i \sqrt{\frac{1}{N_i} + \frac{1}{N_{tot}}}. \end{aligned}$$

Since $N_{tot} \gg N_i$, the second term inside the square root is dropped, and δP_i is calculated according to

$$\delta P_i = \frac{P_i}{\sqrt{N_i}}. \quad (147)$$

The error of the background normalization constant C can be calculated in a similar fashion. Its uncertainty, however, is taken to be due *only* to that of the background subset (N_{ij}^{IJ} in Eq. 39) of

the elastic sample, since the uncertainty of P_i is already taken into account. Furthermore, since the same constant is used to calculate the background of all stacks of a given chamber, treatment of the constant error as a statistical uncertainty would result in correlation among datum points. To address this point, only the P_i contribution to the background error was treated as statistical. The contribution from the normalization constant C was treated as a systematic uncertainty.

In addition to background, the statistical errors of the final results were enlarged due to systematic contributions from a number of factors, such as effective lengths, pot positions, pattern widths, and readout calibrations.

PATTERN WIDTHS were used only in the final fit when the pattern corrections were calculated. So it was a simple matter of re-doing the fit with the new corrections which resulted from the incremented widths.

EFFECTIVE LENGTHS were used mainly in the final step to calculate the components of the scattering angle and the t values. So in the final fit, each of the two left side effective lengths was in turn incremented by one standard deviation (1%), and the result observed.

POT POSITIONS: There were two factors that contributed to the uncertainty of the pot positions: The uncertainty in the positions read out by the electronics, and the uncertainty of the beam position due to centering.

- *The beam position:* In the centering procedure, the distance between the top and the bottom pot is held fixed, and the beam position with respect to the two pots is calculated. A positive perturbation of this beam position by one standard deviation with respect to one pot will result in an *equal* negative perturbation with respect to the other. Since the contents of each cell of one pot is averaged with the corresponding cell of the other pot to form, effectively, a *composite* chamber, this perturbation in the beam position canceled out to first order. Therefore, any effect on the final error due to uncertainty in beam centering was neglected.

- The *pot positions* were known to an accuracy of 35 microns in all cases. Again, since the data from the top and the bottom pots were averaged to yield a composite pot, the error in the position of this composite pot was approximately $\frac{35}{\sqrt{2}} = 24.7$ microns. Therefore, a shift of 24.7 microns in the t scale accounted for the uncertainty in pot position.

CALIBRATIONS: The y coordinate of each event is calculated according to Eq. 20. The error in Y , δY , is determined by taking the variations of the two sides of Eq. 20:

$$(\delta Y)^2 = \left(\sigma_p \frac{dY}{dp} \right)^2 + \left(\sigma_c \frac{dY}{dc} \right)^2 + 2\sigma_{pc}^2 \frac{dY}{dp} \frac{dY}{dc}, \quad (148)$$

where $\frac{dY}{dp}$ and $\frac{dY}{dc}$ are the derivatives of Y with respect to p and c , and σ_{pc}^2 is the covariance between p and c . It is clearly seen that $\frac{dY}{dp} = c$, and $\frac{dY}{dc} = p - y_b = \frac{Y - Y_{counter}}{c}$, where $Y_{counter} = Y_{eb} + Y_{pot}$. Substituting these into the expression for $(\delta Y)^2$, we get

$$(\delta Y)^2 = (c\sigma_p)^2 + \left[\left(\frac{Y - Y_{counter}}{c} \right) \sigma_c \right]^2 + 2(Y - Y_{counter})\sigma_{pc}^2. \quad (149)$$

The second and third terms clearly depend on Y , the location of the event. These terms vanish when $Y = Y_{counter}$, i.e., when the event is located on the edge of the calibration counter. The event can be located as much as 2 mm below the edge and as high as about 20 mm above it (see Fig. 7), so $-2 \text{ mm} \leq Y - Y_{counter} \leq +20 \text{ mm}$. Given typical values of $c = 0.0643 \pm 0.0001 \text{ mm/bit}$, $\sigma_p = 0.06 \text{ bits}$, and $\sigma_{pc} = -1 \times 10^{-5}$, and if we label the first, second, and third terms of Eq. 149 as t_1 , t_2 , and t_3 respectively, then we see that

$$t_1 = (0.0643 \times 0.06)^2 = 1 \times 10^{-5},$$

$$1 \times 10^{-5} \leq t_2 \leq 1 \times 10^{-3}, \text{ and}$$

$$-4 \times 10^{-4} \leq t_3 \leq +4 \times 10^{-5}.$$

While fitting the data, the top and bottom boundaries of each stack were thus perturbed. Since the fitting function was the integrated average of the pattern-corrected differential elastic cross section over the cell boundaries, this procedure changed these boundaries of integration.

To investigate the feasibility of altering the pattern corrections, attention was given to the fact that these corrections are important near the bottom of the chamber. Let us take the very bottom where $Y - Y_{counter} = -2$ mm. Then according to Eq. 149, $(\delta Y)^2 = 1 \times 10^{-5} + 1 \times 10^{-5} + 4 \times 10^{-5} = 6 \times 10^{-5}$, so $\delta Y = \sqrt{6 \times 10^{-5}} = 0.008$ mm. This is only an 8 micron change at the very bottom, which is only about a quarter of the 35 micron error in pot position. It was thus judged that the correction factors did not get affected significantly enough to warrant their change. In the high $|t|$ regions, they are nearly unity anyway.

References

- [1] Block, M. M., and R. N. Cahn, *Phys. Lett.*, **149B**, (1984) , 245.
- [2] Belletini, G., G. Cocconi, A. N. Diddens, E. Lillethun, J. Pahl, J. P. Scanlon, J. Walters, A. M. Wetherell, and P. Zanella, *Phys. Lett.*, **14**, (1965), 164.
- [3] Foley, K. J., R. S. Jones, S. J. Lindenbaum, W. A. Love, S. Ozaki, E. D. Platner, C. A. Quarles, and E. H. Willen, *Phys. Rev. Lett.*, **19**, 857; Galbraith, W., E. W. Jenkins, T. F. Kycia, B. A. Leontic, R. H. Phillips, A. L. Read, and R. Rubinstein, *Phys. Rev.*, **B138**, (1965), 913.
- [4] Denisov, S. P., Y. P. Dmitrevski, S. V. Donskov, Y. P. Gorin, A. I. Petrukhin, Y. D. Prokoshkin, V. S. Seleznev, R. S. Shuvalov, D. A. Stoyanova, and L. M. Vasiljev, *Phys. Lett.*, **B36**, (1971), 528.
- [5] Beznogikh, G. G., et al., *Phys. Lett.*, **B39**, (1972), 411.
- [6] Amaldi, U., et al., *Phys. Lett.*, **B36**, (1971), 504.
- [7] Bartenev, V., et al., *Phys. Rev. Lett.*, **29**, (1972), 1755.
- [8] UA1 Collaboration, *Phys. Lett.*, **B128**, (1983), 336.
- [9] UA4 Collaboration, *Phys. Lett.*, **B115**, (1982), 333.
- [10] Amendolia, S. R., et al., *Phys. Lett.*, **B44**, (1973), 119.
- [11] Favart, D., et al., *Phys. Rev. Lett.*, **47**, (1981), 1191.
- [12] Carboni, G., et al., *Phys. Lett.*, **B108**, (1982), 145.
- [13] Froissart, M., *Phys. Rev.*, **123**, (1961), 1053.

- [14] Martin, A., and F. Cheung, "Analytic Properties and Bounds of the Scattering Amplitudes", Gordon and Breach, New York, (1970).
- [15] Breakstone et al., *Nucl. Phys.*, **B248**, (1984), 253.
- [16] Bozzo et al., *Phys. Lett.*, **147B**, (1984), 392.
- [17] Pomeranchuk, I. Y., *Zh. Eksp. Teor. Fiz.*, **34**, (1958), 725.
- [18] Eden, R. J., *Phys. Rev. Lett.*, **16**, (1966), 39; Kinoshita, T., "Perspectives in Modern Physics", edited by R. E. Marshak, (Wiley, New York), (1966), 211.
- [19] Cornille, H., and A. Martin, *Phys. Lett.*, **B40**, (1972), 671; *Ibid*, *Nucl. Phys.*, **B48**, (1972), 104; *Ibid*, *Nucl. Phys.*, **B49**, (1972), 413; *Ibid*, *Nucl. Phys.*, **B77**, (1974), 141.
- [20] Chou, T. T., and C. N. Yang, *Phys. Rev.*, **170**, (1968), 1591; *Ibid*, *Phys. Lett.*, **B128**, (1983), 457.
- [21] Durand, L., and R. Lipes, *Phys. Rev. Lett.*, **20**, (1968), 637.
- [22] UA4/2 Collab., private communication; results presented at the Blois Workshop on Elastic and Diffractive Scattering, Brown University, Providence, RI, June 8-12, 1993.
- [23] CDF Collab., private communication; results presented at the Blois Workshop on Elastic and Diffractive Scattering, Brown University, Providence, Rhode Island, June 8-12, 1993.
- [24] Amos et al., *Phys. Rev. Lett.*, **63**, (1989), 2784
- [25] Kang, K., and A. R. White, *Phys. Rev.*, **D42**, (1990), 835.
- [26] Amos et al., *Phys. Rev. Lett.*, **68**, (1992), 2433.
- [27] CDF Collaboration, presented at the International Conference on Elastic and Diffractive Scattering (4th Blois Workshop), Elba, Italy, May 22, 1991.

- [28] Bethe, H. A., *Ann. Phys.* (N. Y.), **3**, (1958), 190.
- [29] UA5 Collaboration, G. J. Alner et al., *Z. Phys.*, **C32**, (1986), 153.
- [30] West, G. B., and D. Yennie, *Phys. Rev.*, **172**, (1968), 1413.
- [31] Cahn, R. N., *Z. Phys.*, **C15**, (1982), 253.
- [32] Amos, et al., *Phys. Lett.*, **B301**, (1993), 313.
- [33] Guss, C. M., "Measurement of σ_{tot} and B from $\bar{p}p$ Elastic Scattering at the Fermilab Tevatron", Ph.D. Thesis, Northwestern University, Evanston, IL, 1989.
- [34] Edwards, H. T. , *Ann. Rev. Nucl. Part. Sci.*, **35**, (1985), 605.
- [35] Amos, N., et al., *Nucl. Instr. and Methods in Physics Research*, **A252**, (1986), 263.
- [36] Dimitroyannis, D., "Measurement of the Proton-Antiproton Total Cross Section at the Tevatron Collider", Ph.D. Thesis, University of Maryland, College Park, MD, 1990.
- [37] Lohman, K. D., "Motor Driver Characteristics", CERN/SppS/EBP/Note 78-17, Geneva, Switzerland, 1978.
- [38] Manarin, A., L. Pregernig, M. Rabany, R. Saban, and G. Vismara, *Nucl. Instr. and Methods*, **217**, (1983), 335.
- [39] Shukla, S., "Drift Chamber Telescopes", E710 Internal Note, February 1987.
- [40] Lawson, J. D. , *The Physics of Charged Particle Beams*, New York: Clarendon Press, 1977.
- [41] Amos, N., et al., *Phys. Lett.*, **B243**, (1990), 158.
- [42] Block, M. M., S. Shakir, J. Smith, *ProMath 2.0 and ProMath/VB 2.0, A Professional BASIC Mathematics Library*, Published by TeraTech, Tools for Programmers, 100 Park Ave., Suite 360, Rockville, MD 20850.

- [43] “ $p\bar{p}$ Elastic Scattering at $\sqrt{s} = 1020$ GeV”, FERMILAB-PUB-92-203, (1992), 12pp. ,*Nuovo Cimento*, **106A**, (1993), 123.
- [44] Block, M. and R. N. Cahn, *Reviews of Modern Physics*, **57**, No. 2, (1985), 563.
- [45] Block, M. M., F. Halzen, B. Margolis, A. R. White, private communication, presented at the XXIII International Symposium on Multiparticle Dynamics, Aspen, Colorado, September 12-17, 1993.
- [46] Rubinstein, R., “Total, Elastic and Diffractive Cross Sections at High Energies”, FERMILAB-Conf-90/160-E, August 1990.
- [47] Migdal, A. A., A. M. Polyakov and K. A. TerMartiroysan, *Zh. Eksp. Teor. Fiz.*, **67**, (1974), 84; Abarbanel, H. D., and J. B. Bronzan, *Phys. Rev.*, **D9**, (1974), 2397.
- [48] Block, M. M., K. Kang, and A. R. White, *International Journal of Modern Physics*, **A7**, No. 19, (1992), 4449
- [49] Block, M. et al., *Phys. Rev.*, **D41**, (1990), 978; M. M. Block, F. Halzen, and B. Margolis, *Phys. Lett.*, **B252**, (1990), 481; M. M. Block, F. Halzen, and B. Margolis, *Phys. Rev.*, **D45**, (1992), 839.
- [50] Frauenfelder, H., and E. M. Henley, “Subatomic Physics”, Prentice Hall, Inc., Englewood Cliffs, N.J., (1974), 312.
- [51] Block, M., and A. R. White, *Nucl. Phys. (Proc. Suppl.)*, **B25**, (1992), 59; *Phys. Lett.*, **B273**, (1992), 145.
- [52] Donnachie, A., and P. V. Landshoff, *Nucl. Phys.*, **B267**, (1986), 657; *Nucl. Phys.*, **B348**, (1991), 297; *Particle World*, **2**, (Gordon & Breach, 1991); P. Landshoff, *Nucl. Phys. (Proc. Suppl.)*, **B12**, (1990), 397.

- [53] Amos et al., *Phys. Lett.*, **B247**, (1990), 127.
- [54] Taff. L., D. Ritchie, and T. Lagerlund, "RTMULTI Data Acquisition System", Fermilab Software Support Group, PN-110.2, Batavia, June 1985.
- [55] Brenner, A. E. and R. G. Martin, "Bison Interrupt and Gate Control", Fermilab Software Support Group, HN-3.2, Batavia, November 1977.